

Master's Thesis Spring 2025

Cosmic-Ray Up-scattered Co-SIMPs

Exploring Inelastic Cosmic-Ray-Boosted Dark Matter

Edvard Borkenhagen Rørnes

Theoretical Physics
60 ECTS study points

Department of Physics
Faculty of Mathematics and Natural Sciences

Spring 2025



Edvard Borkenagen Rørnes

Cosmic-Ray Upscattered Co-SIMPs

Exploring Inelastic Cosmic-Ray-Boosted Dark
Matter

Supervisor:
Torsten Bringmann

Abstract

Co-scattering strongly interacting massive particles (Co-SIMPs), denoted χ , constitute a well-motivated dark matter (DM) candidate. Their relic abundance is set by a $\chi + \chi + \text{SM} \rightarrow \chi + \text{SM}$ reaction that maintains kinetic equilibrium with the Standard Model and evades conventional direct detection limits. We investigate whether nucleophilic Co-SIMPs ($\chi\chi p \rightarrow \chi p$) can be probed via cosmic-ray-boosted dark matter (CRDM), in which Galactic cosmic rays upscatter halo DM, producing a flux of relativistic χ capable of triggering underground detectors.

We impose perturbative unitarity and extend the CRDM module in `DarkSUSY` to treat inelastic $2 \rightarrow 3$ Co-SIMP scattering. The boosted flux is obtained by integrating the three-body phase space and, from the resulting recoil spectra in several detectors, we derive bounds on the DM–nucleon cross section.

The unitarity bound eliminates much of the nucleophilic case but does not constrain the purely leptophilic case ($\chi\chi\ell \rightarrow \chi\ell$). Because thermal freezeout demands large cross sections and each scattering event drains substantial energy, the CRDM flux capable of triggering observable $2 \rightarrow 3$ interactions is stopped in Earth’s atmosphere and crust. A loop-induced elastic channel avoids this trap and excludes nucleophilic Co-SIMPs with $0.1 < m_\chi/\text{GeV} < 1$, requiring $\langle\sigma_{32}v^2\rangle \gtrsim 10^{10} \text{ GeV}^{-5}$ for $20 < m_\chi/\text{MeV} < 100$. With our approach, the elastic channel cannot probe Co-SIMP masses below $\sim 20 \text{ MeV}$: producing a detectable recoil would require χ to exceed the $2 \rightarrow 3$ kinematic threshold, leading to substantial energy loss in the detector’s overburden. These CRDM limits rely on an effective-field-theory description and leading-order loop estimates; a UV completion is necessary for definitive exclusion.

Preface

This thesis represents the work I have done throughout the last year under the supervision of Professor Torsten Bringmann, with major contributions from Professor Takashi Toma.

I have opted not to include derivations which can be found in common graduate-level textbooks and instead cited such results. However, I aimed for the level of this thesis to be accessible enough that I myself would have been able to understand the material before I began researching this topic. As such, it should be accessible to a second year master's student who has prerequisites equivalent to the two quantum field theory courses at the University of Oslo. Additionally, Section 2.5 assumes some familiarity with cosmological concepts.

A warm thanks to Torsten Bringmann and Takashi Toma for their invaluable insight into this topic and for the wonderful collaboration. I especially appreciated our biweekly meetings and the discussions that came along with them.

Torsten, I apologize for all the times I excitedly emailed you a breakthrough—only to discover an hour later that it was just me being an idiot.

I want to thank Adam, Aksel, Anton, Isak and Morten, whom I've shared an office with over the last few years. Our discussions, while not always productive, have always been interesting. Especially you, Anton—I think I would have gone mad staying in the office late at night without someone else around. Of course, thanks to everyone at the theoretical physics department for the enjoyable lunch breaks and engaging conversations.

Special thanks to my parents for consistently showing up to Oslo and feeding me with both wine and food far beyond my student budget, or my ability to properly appreciate, and for always supporting me. Additionally, thanks to my sister, brother-in-law, nieces, and nephew for always letting Violet and me stay at your place, no matter the circumstances. Finally, thanks to my brother—somehow both a neighbor and a rare sight, except when summoned by our parents.

Last but not least, Violeta, who gave me the motivation to pursue my goals through thick and thin, and who had to endure me rambling about abstract topics for the past two years—often against her will.

We note that part of the language and formatting in this thesis were improved with the assistance of AI-based writing tools. All suggestions were reviewed with rigor to ensure accuracy and consistency.

Contents

1	Introduction	1
1.1	Overview	2
1.2	Notation and Conventions	3
2	Dark Matter	5
2.1	Evidence	5
2.2	Halos	5
2.3	Detection	7
2.4	Typical Candidates	9
2.5	Co-Scattering SIMPs	10
3	Cosmic Ray Upscattering	15
3.1	Interstellar Cosmic-Ray Flux Energy Spectrum	15
3.2	CRDM Flux	17
3.3	Composite Interactions	21
3.4	Attenuation	23
3.5	Recoil Rates & Constraints	26
4	Cosmic-Ray-Boosted Co-SIMPs	29
4.1	$2 \rightarrow 3$ Scattering	29
4.2	Co-SIMP CRDM Flux	35
4.3	Recoil Rates in a Detector	43
4.4	Constraints	46
4.5	Energy Loss of $2 \rightarrow 3$ Interactions	50
4.6	Two-Loop Elastic Co-SIMP Scattering	52
5	Discussion	59
6	Conclusion	63
A	$2 \rightarrow 3$ Scattering	65
A.1	Cross Section	65
A.2	CM Angles	67
A.3	Analytical Simplification of Differential Cross Section	68
B	Implementation in DarkSUSY	71

Chapter 1

Introduction

Dark matter (DM) remains one of the greatest mysteries in modern physics. It is a necessary constituent of the universe, required to explain a range of observations. The first signs of a discrepancy between theoretical predictions and measurements—which pointed toward the existence of dark matter—were seen in the orbital velocities of galaxies within clusters, as observed by Zwicky in 1933 [1]. Later observations of the Andromeda Galaxy revealed similar discrepancies in stellar velocities. At the time, there was no scientific consensus on what could cause these phenomena, and it was not until the 1970s that the dark matter hypothesis gained mainstream acceptance in the scientific community [2].

Today, the most compelling evidence for dark matter comes from large-scale cosmological observations, including the formation of large-scale structure and the cosmic microwave background (CMB) [3]. From a combination of theoretical arguments and experimental input, the general constraints on DM can be summarized as follows:

- Interacts primarily through gravity, with minimal (or no) coupling to Standard Model (SM) particles.
- Must be cold, i.e., non-relativistic.¹
- Satisfies the present-day relic density requirement $\Omega_{\text{DM},0}h^2 = 0.11933 \pm 0.00091$ [3].
- Remains stable over cosmological timescales.
- Must be consistent with various theoretical and experimental bounds, including those from big bang nucleosynthesis, self-interactions, astrophysical observations, and direct detection experiments.

Satisfying all of the above, while also providing candidates with testable predictions, is a difficult task. Nevertheless, over the years many viable dark matter candidates have been proposed, including heavy neutrinos, weakly interacting massive particles (WIMPs), and strongly interacting massive particles (SIMPs). Many early candidates—such as heavy neutrinos and WIMPs—have now been largely excluded due to increasingly stringent experimental constraints.

In this thesis, the primary goal is to use a relatively new framework, initially proposed by [4], known as cosmic-ray-boosted dark matter (CRDM), to probe a recently suggested freezeout mechanism introduced in [5], known as co-scattering strongly interacting massive

¹In the cosmological sense. An individual DM particle may be relativistic, but the ensemble of DM particles responsible for structure formation must be non-relativistic with respect to the comoving frame.

particles (Co-SIMPs). The Co-SIMP mechanism builds on the existing SIMP model, but achieves both thermal freezeout and kinetic equilibrium with the SM through the same number-changing interaction—eliminating the need for an additional mediator to maintain thermal contact. This is achieved through a number-changing interaction of the form $\chi\chi\psi \rightarrow \chi\psi$, where χ (ψ) denotes a DM (SM) particle, which sets the present-day dark matter relic density. Unlike SIMPs, whose dark sector typically interacts with the SM exclusively via a weakly coupled portal, the dark sector of Co-SIMPs is not minimally connected to the SM. If such interactions are sufficiently strong, present-day direct detection experiments may be capable of probing this scenario.

Within the frameworks considered so far, the Co-SIMP parameter space remains largely open [5]. This work aims to test whether Co-SIMPs are excluded by current bounds using the CRDM framework. CRDM relies on high-energy SM–DM interactions between cosmic rays and dark matter in the galactic halo. These interactions induce a small but irreducible flux of relativistic DM incident on Earth. This boosted flux may subsequently interact with terrestrial detectors, potentially producing observable signals of SM–DM scattering. It is precisely this scenario that we aim to investigate.

Assuming perturbative estimates remain valid, CRDM constraints exclude nucleophilic Co-SIMPs—meaning direct couplings to nucleons—in the mass range $m_\chi \sim [0.1, 1]$ GeV, while masses $m_\chi \sim [20, 100]$ MeV remain viable provided $\langle\sigma_{32}v^2\rangle \gtrsim 10^{10}$ GeV $^{-5}$, allowing them to evade current direct detection bounds. Due to attenuation² of the high-energy CRDM flux, our approach cannot probe $m_\chi \lesssim 20$ MeV, leaving this region unconstrained. Projected sensitivities from the upcoming Darwin experiment indicate that, if no signal is seen, the region $m_\chi \sim [1, 2]$ GeV may be excluded. Finally, to account for the entire DM abundance, CRDM bounds restrict nucleophilic Co-SIMPs to $m_\chi \sim [1, 20]$ MeV. We emphasize that these results rely on perturbative estimates in a strongly interacting theory and should not be viewed as conclusive; a UV completion is necessary for definitive exclusion. In addition, we impose a perturbative unitarity bound, which excludes large portions of the nucleophilic scenario but does not constrain the leptophilic case ($\chi\ell \rightarrow \chi\chi\ell$).

1.1 Overview

This section provides a brief overview of the structure and goals of the thesis. Chapter 2 outlines the general details surrounding dark matter, including observational evidence, detection strategies, and typical DM candidates, before taking a deeper dive into the Co-SIMP scenario and its corresponding unitarity bound. In Chapter 3 we introduce cosmic ray upscattering, and explain how SM–DM interactions give rise to an irreducible component of CRDM incident on Earth. Here it is shown how this flux can potentially produce observable nuclear recoils in direct detection experiments, which in turn constrain the strength of such interactions. Chapter 4 begins by going through the basics of relativistic kinematics of a general $2 \rightarrow 3$ process, and applies this to Co-SIMPs within the framework of CRDM. We present results from our numerical implementation in `DarkSUSY` [6], arriving at the Co-SIMP CRDM flux, recoil rates, and resulting constraints. Upon realizing that the large cross section required for detecting pure Co-SIMP CRDM—meaning that the $2 \rightarrow 3$ interaction occurs both in the galactic halo and the detector—leads to complete attenuation through the Earth’s crust and atmosphere, we further consider a two-loop induced elastic scattering process. This allows us to utilize the full treatment of attenuation in `DarkSUSY`, based on the work done in [7]. After completing

²Meaning energy loss and suppression while traversing Earth’s atmosphere and crust.

the analysis, we provide an overview and discussion of the results in Chapter 5 and scrutinize the theoretical assumptions. Finally, in Chapter 6 we conclude and consider which future developments should be pursued. Appendix A provides the more involved derivations surrounding the $2 \rightarrow 3$ cross section and kinematics. In addition, we provide a brief overview of the differences in our implementation compared to `DarkSUSY 6.4.1` in Appendix B. For further details, we refer the reader to [6].

1.2 Notation and Conventions

Here we outline the notation and conventions followed throughout the thesis. Unless explicitly stated otherwise, the following will apply:

- Natural units, i.e. $c = \hbar = k_B \equiv 1$, will be used. All quantities may then be referred to by their mass (or energy) dimension, e.g. [time] = -1 , implying it has units mass^{-1} . We will generally restore SI units when presenting results.
- **Bold**, non-italic characters for 3-vectors, e.g. \mathbf{a} . Their components are given by Latin superscripts a^i with $i \in \{1, 2, 3\}$.
- Non-bold, *italic* characters for 4-vectors, e.g. a . A contravariant (covariant) vector a has components given by Greek indices $a^\mu \equiv (a^0, \mathbf{a})$ ($a_\mu \equiv (a^0, -\mathbf{a})$) with $\mu \in \{0, 1, 2, 3\}$.
- A 4-vector and Lorentz scalar will be referred to as a vector and scalar, respectively.
- Repeated indices are summed over.
- The convention used for the inner product³ of two vectors is given by $g(a, b) \equiv ab \equiv g_{\mu\nu}a^\mu b^\nu = a^0b^0 - \mathbf{a} \cdot \mathbf{b}$ where $g_{\mu\nu} = \text{diag}(+1, -1, -1, -1)$ is the mostly minus Minkowski metric.
- For a $2 \rightarrow 2$ ($2 \rightarrow 3$) processes the momentum labeling is $p_1 p_2 \rightarrow p_3 p_4$ ($p_1 p_2 \rightarrow p_3 p_4 p_5$).
- Whenever a non-scalar quantity is denoted with a prime, e.g. E' , it refers to its value in the center of mass (CM) frame. While not necessary, this will also be applied to inner products of vectors when it enhances the clarity of a computation.
- The notation for the generalized Mandelstam variables used is $s_{ij} \equiv (p_i + p_j)^2$ and $t_{ij} \equiv (p_i - p_j)^2$ with $s \equiv s_{12} = E_{\text{CM}}^2$.
- Non-primed quantities will either refer to an arbitrary frame or the cosmic/lab frame. This should be clear from the context.
- Superscript $+$ ($-$) refers to upper (lower) integration limits. We will always choose our integration limits in such a way that $a^+ \geq a^-$ where a is any integration variable.
- In Chapter 3, the Greek letter χ is reserved for generic DM, while in the rest of the thesis it denotes the Co-SIMP DM candidate. Standard Model particles are labeled ψ , and SM nuclei are denoted by N . When referring specifically to direct detection constraints on unboosted halo DM, we use the label ‘DM’ to distinguish it from CRDM-induced signals.

³Of course, the physicists inner product.

- The standard n -dimensional Fourier transform convention for physics is used throughout:

$$f(p) = \int d^n x f(x) e^{+ipx} \quad \text{and} \quad f(x) = \int \frac{d^n p}{(2\pi)^n} f(p) e^{-ipx}.$$

Chapter 2

Dark Matter

This chapter provides a brief overview of the evidence for the existence of DM, the methodologies employed in its detection, and typical DM candidates. For a recent and more in-depth pedagogical review of these topics, see [8]. Additionally, we discuss dark matter halos and their uncertainties, as they are a necessary component of the framework this thesis builds on. We conclude this chapter by introducing Co-SIMPs, a recently proposed freezeout mechanism [5], which this thesis investigates through cosmic-ray upscattering [4].

2.1 Evidence

Galaxy rotation curves reveal that the visible mass alone cannot account for the observed orbital velocities of stars in galaxies and galaxy clusters, implying the presence of an additional unseen mass component [9]. Gravitational lensing measurements confirm this across galaxy clusters and large-scale structures [10], independently supporting the existence of a gravitational source beyond luminous matter. On cosmological scales, anisotropies in the cosmic microwave background and the large-scale distribution of galaxies provide the strongest constraints on the dark matter abundance and clustering behavior [3]. All of these observations are consistent with a cold, non-baryonic matter component that interacts predominantly through gravity.

Together, these observations converge on the same conclusion: DM must constitute $(84.14 \pm 0.13)\%$ of the matter energy content in the universe [3], yet its fundamental nature remains unknown. While DM has not been detected—with the exception of gravitational interactions—these observations strongly motivate its existence. The leading hypothesis is that DM is composed of one or more new particle species, and is widely favored over alternative explanations such as modifications to gravity. However, the particle properties of DM remain unknown, motivating ongoing experimental and theoretical efforts.

2.2 Halos

Dark matter halos are gravitationally bound structures surrounding galaxies and galaxy clusters, inferred from a range of astrophysical and cosmological observations. If DM is particle-like, such halos arise naturally from the nonlinear growth of primordial density perturbations—whose gravitational enhancement is essential for the formation of galaxies and clusters [8].

The exact form of these halos is not well known and remains an active research subject. Numerous attempts have been made to accurately simulate the DM density

profile surrounding galaxies and explore their implications for broader areas of physics, such as the Λ CDM cosmological model [11–14]. To date, there is no scientific consensus on a universally correct DM density profile. However, several parametrizations are widely used:

1. Pseudo-isothermal halo profile:

$$\rho_{\text{DM}}(r) = \frac{\rho_0}{1 + (r/r_c)^2}, \quad (2.1)$$

where ρ_0 is the DM density at the galactic core and r_c is the radius of said core.

2. The Navarro-Frenk-White (NFW) profile:

$$\rho_{\text{DM}}(r) = \frac{\rho_c \delta_c}{(r/r_s)(1 + r/r_s)^2}, \quad (2.2)$$

where $\rho_c = 3H^2/(8\pi G)$ is the critical density, r_s is the scale radius and δ_c is the dimensionless characteristic overdensity.

3. Einasto profile:

$$\rho_{\text{DM}}(r) = \rho_e \exp \left(-d_n \left[\sqrt[n]{r/r_e} - 1 \right] \right), \quad (2.3)$$

where d_n is a function of n defined by the requirement the total DM mass within a radius r_e is exactly half of the total DM mass of the galaxy, and $n > 1/2$ is an empirically determined shape parameter.

While all three profiles are commonly used, none provides a universally accurate description of the DM distribution across different astrophysical systems. The pseudo-isothermal profile features a central core and is often used to fit the rotation curves of dwarf and low-surface-brightness galaxies [15]. On the other hand, the NFW and Einasto profiles typically arise from cold DM N-body simulations assuming collisionless dynamics [16, 17]. However, simulation outcomes depend sensitively on the physical inputs—such as whether baryons are included—and on the type of system being modeled (e.g., clusters, dwarfs, or disk galaxies) [18]. Since this thesis focuses on the Milky Way, it is important to note that there is no observational evidence for a core in the inner halo, nor any theoretical expectation of one at radii $r \gtrsim 0.1$ kpc [19]. Since the NFW and Einasto profiles yield similar results for the Milky Way over the radial range of interest, we adopt the NFW profile for its simplicity and conventional status in the literature.

These profiles all rely on input from the locally measured DM density, $\rho_{\text{DM}}^{\text{loc}}$. For a comprehensive review of local DM density determinations, see [20]. Modern estimates typically fall within the range $\rho_{\text{DM}}^{\text{loc}} \in [0.2, 0.4] \text{ GeV/cm}^3$. The specific benchmark value chosen, along with the distance to the Galactic center, is used to fix the normalization of the density profiles. In this thesis, we follow the default in `DarkSUSY`, which sets $\rho_{\text{DM}}^{\text{loc}} = 0.3 \text{ GeV/cm}^3$ as the local DM energy density [4, 6].

2.3 Detection

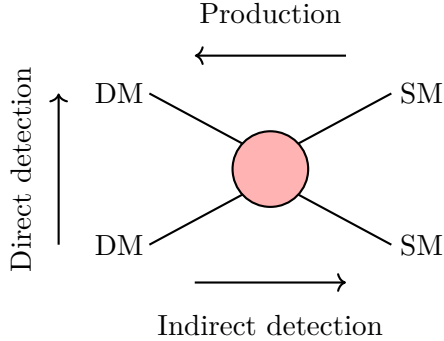


Fig. 2.1: Schematic of the main non-gravitational approaches of DM detection.

Non-gravitational DM detection is typically categorized into three main mechanisms: production, indirect detection, and direct detection. In Fig. 2.1, we show a rough schematic of this idea. We provide a brief introduction to production and indirect detection of DM, and discuss direct detection in more depth, as it is the relevant detection mechanism for this thesis.

Production

The production of dark sector particles is a major goal of collider experiments such as ATLAS and CMS at the Large Hadron Collider (LHC). These searches are motivated in large part by the possibility that DM resides within such a sector and can be produced at high energies. Since DM must interact only weakly with SM particles, it cannot be directly observed in particle detectors. Instead, its presence is inferred from missing transverse energy (\cancel{E}_T), which arises when undetected particles carry away momentum in the transverse plane of the collision. Identifying such missing energy forms the basis of DM production searches.

Despite extensive efforts, no conclusive evidence for DM has been observed in collider experiments. However, the absence of a signal sets strong constraints on DM models, particularly in terms of mediator masses, coupling strengths, and interaction cross sections. Current LHC data have ruled out a wide range of parameter space. For example, for mediators coupled to heavy quarks, the mediator mass is constrained up to the TeV scale [21].

It is important to note that these searches are sensitive to any weakly interacting particle associated with a dark sector, not just DM. Even if such a particle is detected, there is no guarantee that it constitutes the cosmologically observed DM. Nevertheless, DM remains one of the primary motivations for these searches, and collider results are frequently interpreted in the context of DM models.

Future collider experiments, such as the High-Luminosity LHC [22] and proposed next-generation facilities, aim to extend the sensitivity of dark sector searches. These experiments will allow for the exploration of weaker DM–SM interactions and higher mass scales, improving the ability to test a wide range of theoretical models.

Indirect Detection

Indirect detection of DM aims to probe its particle properties by observing the effects of self-annihilation or decay into SM particles. This approach is based on the premise that DM particles, if capable of self-annihilation or decay, could produce SM particles such as gamma rays, neutrinos, or cosmic rays. By modeling the spectrum of, e.g., cosmic rays stemming from known SM sources, one can predict the expected signal. If the properties of these secondaries deviate from SM expectations, they can be observed using space- and ground-based detectors, thereby providing constraints on the particle nature of DM [23]. The main targets for indirect detection include regions of high DM density, such as the galactic center, dwarf spheroidal galaxies, and galaxy clusters.

Significant efforts have been made to constrain DM properties through indirect detection experiments. For instance, the Fermi Gamma-ray Space Telescope has placed stringent limits on the annihilation cross section of WIMPs in the GeV to TeV mass range [24]. Neutrino observatories such as IceCube and Super-Kamiokande have searched for high-energy neutrino signals arising from DM annihilation in the Sun, where DM particles may accumulate and annihilate [25, 26].

Direct Detection

Direct detection (DD) experiments aim to directly measure the scattering of DM particles with ordinary matter. If such interactions occur, they would produce low-energy nuclear recoils when DM particles scatter off target nuclei in terrestrial detectors. The expected event rate and recoil energy spectrum of conventional non-relativistic DM (i.e., halo DM) depend on the local DM density, the Galactic velocity distribution—typically modeled using the Standard Halo Model (SHM) [27, 28]—and the specific properties of the DM particle, such as its mass and interaction cross section.

One of the most sensitive direct detection experiments to date is the XENON1T detector, which utilizes liquid xenon as the target material [29]. Xenon-based detectors offer several advantages, including a high atomic mass for enhanced scattering probability, excellent scintillation and ionization properties, and low intrinsic backgrounds (e.g., from radioactive impurities) [30, 31]. While the successor experiment, XENONnT, has recently improved sensitivity to spin-independent DM–nucleon scattering [32], we use XENON1T data as the basis for our constraints due to the availability of detailed recoil response information and analysis thresholds relevant for CRDM studies. The sensitivity of these experiments is largely determined by their ability to suppress background events, achieved through material screening, shielding, and advanced analysis techniques. Despite these efforts, distinguishing between potential DM-induced signals and background events from natural radioactivity or cosmic rays remains a major challenge. As a result, DD experiments are typically placed deep underground, where the Earth’s crust serves as a natural shield against background radiation. DM particles, due to their extremely low interaction rates with the SM, can still pass through and potentially scatter in the detector.

Conventional searches have placed increasingly stringent limits on the spin-(in)dependent DM–nucleon scattering cross section, $\sigma_{\chi p}^{\text{SD}} \lesssim 10^{-41} \text{ cm}^2$ ($\sigma_{\chi p}^{\text{SI}} \lesssim 10^{-46} \text{ cm}^2$) for DM masses around 10 GeV [32, 33]. However, such searches are inherently limited by the velocity distribution of DM in the galactic halo. Since DM within the halo is required to be non-relativistic to remain gravitationally bound to the Milky Way, we require $v_{\text{DM}} < v_{\text{esc}} \simeq 530 \text{ km/s}$ [34]. For DM masses below the GeV scale, its kinetic energy is too low to exceed the recoil energy thresholds of current detectors. For instance, applying

this bound to elastic SM–DM scattering in XENON1T, which has a recoil threshold of 4.9 keV, shows that only DM with $m_{\text{DM}} \gtrsim 10 \text{ GeV}$ can be detected.¹

Recently, a new mechanism known as cosmic-ray-boosted DM (CRDM) has been proposed [4], and has become an active area of research [7, 35–39]. This mechanism bypasses the requirement of $v_{\text{DM}} < v_{\text{esc}}$ limitation by acknowledging the additional DM flux from CR–DM interactions within the galactic halo, allowing sub-GeV DM to be probed by these underground detectors. CRDM is the main topic of this thesis, and we will analyze the general mechanism in detail in Chapter 3.

2.4 Typical Candidates

Many particle-like DM candidates have been proposed over the last 50 years. In this section, we briefly introduce a few of the most well-studied examples.

The most explored thermal DM candidate is the weakly interacting massive particle (WIMP), which arises naturally in many beyond-the-Standard-Model theories, such as supersymmetry [40, 41]. WIMPs are characterized by weak-scale interaction strengths and predicted masses around the electroweak scale, typically around 1 TeV. Their relic abundance is generally set via a freezeout mechanism involving $2 \rightarrow 2$ annihilation. The thermally averaged annihilation cross section required to achieve the observed DM relic density coincides with that of weak-scale interactions, a coincidence in scales often referred to as the “WIMP miracle” [42]. However, despite decades of experimental effort—including direct detection (XENON1T [29], LZ [43]), indirect detection (Fermi-LAT [44, 45], AMS-02 [46]), and collider searches (LHC [47])—no conclusive evidence for WIMPs has been found. As a result, simple WIMP models are increasingly constrained, with upper bounds on scattering cross sections from DD reaching $\sim 10^{-46} \text{ cm}^2$ for weak-scale masses.

Given these constraints, alternative thermal DM candidates have gained more attention. One such candidate is the strongly interacting massive particle (SIMP), which features strong self-interactions while remaining only weakly coupled to the SM [48]. SIMPs achieve the correct relic abundance through number-changing self-annihilation processes, typically of the form $\chi\chi\chi \rightarrow \chi\chi$. Unlike WIMPs, whose interactions primarily involve SM particles, SIMPs interact dominantly within the dark sector. Their relatively strong self-scattering makes them testable through effects on structure formation, but they are subject to constraints from the CMB, big bang nucleosynthesis, and astrophysical observations such as the Bullet Cluster [49]. Because their SM coupling is generally small, they remain difficult, but not impossible, to probe in direct detection experiments [48].

Another notable class of candidates includes sterile neutrinos: right-handed neutrinos that are not charged under the SM’s left-handed $SU(2)_L$ gauge group. They are typically non-thermal DM candidates, produced via neutrino oscillations or freeze-in mechanisms in the early Universe. Sterile neutrinos are also motivated by the see-saw mechanism, which offers an explanation for the small neutrino masses observed in the SM [50, 51]. Their presence can be tested through X-ray observations, as they may decay into active neutrinos and photons, producing potentially observable spectral lines [52].

Finally, axions are ultra-light bosons originally proposed to solve the strong CP problem in QCD [53]. If they exist, axions could be produced non-thermally via the misalignment mechanism and account for the observed DM abundance [54, 55]. Their

¹The 4.9 keV recoil threshold corresponds to a conservative S1 cut of 3 photoelectrons in XENON1T. Analyses using lower thresholds—such as S2-only events—can probe recoil energies below $\sim 2 \text{ keV}$, enabling sensitivity to DM masses as low as $m_{\text{DM}} \sim 2\text{--}6 \text{ GeV}$, depending on detector specifics.

coupling to electromagnetic fields enables detection via experiments such as ADMX, which searches for axion-photon conversion in strong magnetic fields [56–58].

2.5 Co-Scattering SIMPs

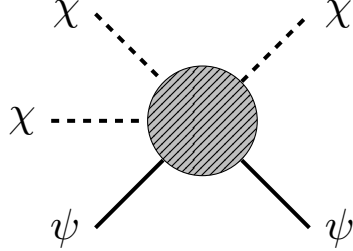


Fig. 2.2: Co-SIMP freezeout process. The gray ‘blob’ implies an effective interaction rather than a fundamental one; a UV completion is required for renormalization.

Recently, [5] proposed an alternative to SIMPs, known as co-scattering strongly interacting massive particles (Co-SIMPs). In contrast to standard SIMPs, which reduce their comoving number density through a $3 \rightarrow 2$ self-annihilation process within the dark sector, Co-SIMPs involve an SM particle in the number-changing interaction. In the case where $m_\chi \lesssim 2m_\psi$, the dominant process is a co-annihilating interaction of the form $\chi\chi\psi \rightarrow \chi\psi$, where χ denotes the DM particle and ψ is an SM particle, as shown in Fig. 2.2. This interaction modifies the freezeout dynamics and offers an alternative mechanism to set the relic abundance, while maintaining thermal contact with the SM to avoid overheating the DM—‘killing two birds with one stone’ [59]. This extends the SIMP paradigm in a minimal way, relaxing the need for large self-interactions while preserving testable couplings to the SM.

Throughout this thesis, we take the Co-SIMP candidate, χ , to be a complex scalar. This is necessary, since ensuring stability requires that Co-SIMPs are charged under a \mathbb{Z}_3 symmetry, which enforces that all interactions preserve charge modulo 3. This restricts allowed dark-sector processes to those in which the net number of χ particles changes by a multiple of three. As a result, processes such as $\chi\psi \rightarrow \bar{\chi}\bar{\chi}\psi$ and $\bar{\chi}\psi \rightarrow \chi\chi\psi$ are allowed, while others like $\chi\chi\psi \rightarrow \chi\psi$ are forbidden at tree level. Elastic processes such as $\chi\chi \rightarrow \chi\chi$ are forbidden, but $\chi\psi \rightarrow \chi\psi$ can be generated radiatively through intermediate states consistent with \mathbb{Z}_3 charge conservation. We use the shorthand $\chi\chi\psi \rightarrow \chi\psi$ to collectively denote both tree-level co-scattering channels permitted by the \mathbb{Z}_3 symmetry, including the crossed process $\chi\psi \rightarrow \chi\chi\psi$.

Given $m_\chi \lesssim 2m_\psi$, then during the thermal epoch the Boltzmann equation describing the evolution of the dark matter number density, n_χ , in the non-relativistic limit takes the form [5]:

$$\frac{dn_\chi}{dt} + 3Hn_\chi = -\langle\sigma_{32}v^2\rangle(n_\chi^2 - n_{\chi,\text{eq}}^2)n_{\psi,\text{eq}}. \quad (2.4)$$

Here $\langle\sigma_{32}v^2\rangle$ is an effective thermally averaged cross section for the co-annihilation process and $n_{\chi,\text{eq}}$ and $n_{\psi,\text{eq}}$ are the number densities at equilibrium. If we allow $m_\chi \gtrsim 2m_\psi$, the process $\chi\chi \rightarrow \chi\psi\psi$ becomes dominant, leading to a WIMP-like freezeout. While the case $m_\chi \gtrsim 2m_\psi$ is allowed, it leads to a WIMP-like freezeout; this thermal history is not the focus of this thesis.

The presence of ψ changes the scaling behavior of the effective interaction rate. While standard SIMP freezeout relies on the interaction rate scaling as $\langle \sigma v^2 \rangle \sim \alpha^3/m_\chi^5$ —where α is a generic coupling and m_χ the dark matter mass—the co-annihilation process involves a mixed rate that scales more softly with m_χ , also depending on the mass and abundance of ψ . This opens up a wider viable mass range for χ , extending up to the GeV regime when considering nucleophilic processes of the form $\chi\chi p \rightarrow \chi p$. For the leptophilic case $\chi\chi\ell \rightarrow \chi\ell$ this range is much lower, requiring $m_\chi \lesssim 1$ MeV. In this thesis we assume spin-independent direct couplings to protons and neutrons of the form $\mathcal{L} \supset \Lambda^{-2}\chi^3(\bar{p}p + \bar{n}n)$ where Λ is some energy scale where our effective theory breaks down.

Moreover, because the dominant interaction is not purely among χ particles, the model evades many of the small-scale structure constraints that plague conventional SIMPs [5, 60]. For example, the strong self-scattering among dark matter particles, often required for standard SIMPs to achieve sufficient freezeout, tends to be in tension with observations of galaxy halos [61]. In the Co-SIMP case, much of the annihilation burden is offloaded onto the interactions involving ψ , and the self-scattering cross section, σ_{self} , remains within acceptable limits. This enables Co-SIMPs to retain the benefits of strongly interacting models, such as addressing small scale structure problems, without running into bounds from cluster collisions or halo shapes.

Existing Constraints

We briefly review the existing constraints that apply to Co-SIMPs and, in addition, include the requirement that the S -matrix be unitary. Conventionally, since Co-SIMPs are thermal relics, these constraints are typically formulated in terms of the thermally averaged cross section which governs the freezeout dynamics. The thermally averaged cross section for any $\alpha \rightarrow \beta$ process, $\langle \sigma_{\alpha\beta} v^{\alpha-1} \rangle$, is defined in such a way that the annihilation rate per unit volume per unit time—up to combinatorial factors—is [62]

$$\langle \sigma_{\alpha\beta} v^{\beta-1} \rangle \prod_{i=1}^{\alpha} \frac{\rho_i}{m_i}, \quad (2.5)$$

where ρ_i and m_i are the initial-state energy densities and masses, respectively. While more transparent, this definition is not particularly convenient. Thus, one often works with an equivalent definition [63]:

$$\langle \sigma_{\alpha\beta} v^{\alpha-1} \rangle = \frac{1}{S_\alpha S_\beta} \left[\prod_{i=1}^{\alpha} \frac{1}{n_i^{\text{eq}}} \int \frac{d^3 p_i}{(2\pi)^3 2E_i} g_i f_i \right] \left[\int d\Pi_\beta \overline{|\mathcal{M}_{\alpha \rightarrow \beta}|^2} \right]. \quad (2.6)$$

Here S_α (S_β) is the symmetry factor in the initial (final) state (e.g., $S_\alpha = N!$ for N identical particles in the initial state), n_i^{eq} is the number density of species i at equilibrium,² and g_i and f_i are the number of internal degrees of freedom and distribution function, respectively, for particle species i . Furthermore, $d\Pi_\beta$ is the β -particle Lorentz invariant phase space (LIPS) for the out-state particles which, given incoming momenta p_α and outgoing momenta p_β , is [64]³

$$d\Pi_\beta = (2\pi)^4 \delta^4 \left(\sum_\alpha p_\alpha - \sum_\beta p_\beta \right) \prod_\beta \left[\frac{d^3 p_\beta}{(2\pi)^3 2E_\beta} \right]. \quad (2.7)$$

²The particular type of equilibrium is model dependent. It can e.g. mean thermal, kinetic or chemical equilibrium based on which processes dominate.

³Note that we include a factor of $(2\pi)^4$ in $d\Pi_n$ unlike how it is done in [64]. Additionally we emphasize here that α and β are *not* Lorentz indices but simple labels for in and out particles respectively.

Finally, $|\mathcal{M}_{\alpha \rightarrow \beta}|^2$ is the matrix element squared, summed over both initial- and final-state spins. In this generalized case, it is often best to consider $\sigma_{\alpha\beta}v^{\alpha-1}$ as a single ‘symbol’ as opposed to independently meaningful quantities.⁴

Imposing the relic density requirement $\Omega h^2 < 0.12$ leads to the following lower bound on the thermally averaged cross section at freezeout [5]⁵

$$\langle\sigma_{32}v^2\rangle_{\text{f.o.}} > \left(\frac{\text{GeV}}{m_\chi}\right)^3 \text{GeV}^{-5} \times \begin{cases} 10^3 \left(\frac{10^{-9}}{\eta}\right), & m_\chi \ll m_{\text{SM}}, \\ 5 \times 10^{-3}, & m_\chi \sim m_{\text{SM}}, \end{cases} \quad (2.8)$$

where η is the baryon-to-photon ratio. Co-SIMPs that fail to satisfy this bound would not annihilate efficiently, resulting in a relic density $\Omega h^2 > 0.12$ and thus overclosing the Universe.

Observations of merging galaxy clusters (e.g. the Bullet Cluster) show that dark-matter halos remain aligned with the collision-less galaxies, implying they must scatter only rarely. This “collision-less” requirement translates to a self-interaction bound of $\sigma_{\text{self}}/m_\chi \lesssim 1 \text{ cm}^2 \text{ g}^{-1} \approx 10^{-24} \text{ cm}^2 \text{ GeV}^{-1}$ [65]. The self-scattering cross section σ_{self} induced via the 2-loop process $\chi\chi \rightarrow \chi\chi$ is approximately [5]

$$\sigma_{\text{self}}^{\text{Co-SIMP}} \approx 10^{-7} \left(\frac{\text{GeV}}{m_\chi}\right)^2 \left[\frac{\langle\sigma_{32}v^2\rangle_p}{\text{GeV}^{-5}}\right] \text{cm}^2, \quad (2.9)$$

where the subscript p implies that this involves proton propagators. This leads to an upper bound on the thermally averaged cross section in the nucleophilic case:

$$\langle\sigma_{32}v^2\rangle_p \lesssim 10^{23} \left(\frac{m_\chi}{\text{GeV}}\right)^3 \text{GeV}^{-5}. \quad (2.10)$$

We note that this bound is weakened by the \mathbb{Z}_3 symmetry, which forbids $\chi\chi \rightarrow \chi\chi$ at tree level, as it would violate \mathbb{Z}_3 charge conservation. This requires the process to proceed only through higher-loop interactions. The same suppression renders the corresponding constraint in the leptophilic case negligible—further weakened by a factor of $\sim 10^{10}$ —since the strength of the induced self-interaction scales with the mass of the SM particle [5].

In addition to the constraints discussed above, Co-SIMPs must respect unitarity bounds, which can be derived using the optical theorem.⁶ For any $\alpha \rightarrow 2$ freezeout process, the unitarity bound on the thermally averaged cross section takes the following form in the non-relativistic limit [62]:

$$\langle\sigma_{\alpha 2}v^{\alpha-1}\rangle \leq 2^{(3\alpha-1)/2} S_\alpha \frac{\prod_\beta g_\beta}{\prod_\alpha g_\alpha} \left[\frac{\sum_\alpha m_\alpha}{\prod_\alpha m_\alpha}\right]^{3/2} \left(\frac{\pi}{T}\right)^{(3\alpha-5)/2}, \quad (2.11)$$

where T is the freezeout temperature. If we take ψ to be a fermion, and since χ is a complex scalar, then all species have $g_i = 2$. Further, taking freezeout to occur at $x \equiv m_\chi/T \sim 10$, the $3 \rightarrow 2$ Co-SIMP scenario ($\alpha = 3$, $S_\alpha = 2$) gives the perturbative unitary bound in the non-relativistic limit:

$$\langle\sigma_{32}v^2\rangle \leq 1.6 \times 10^4 \left[\frac{\text{GeV}}{m_\chi}\right]^5 \left[\frac{2m_\chi}{m_\psi} + 1\right]^{3/2} \text{GeV}^{-5}. \quad (2.12)$$

For a review of alternative bounds that do not constrain Co-SIMPs, the supplemental material of [5] offers a helpful overview and discussion.

⁴Technically it is only σ which requires interpretation. The v^{n-1} symbol is meant to signify the flux (or velocity) of $n - 1$ particles arriving at the rest frame of one of the initial particles.

⁵We omit the subscript on Ω_{DM} as it is the only relevant density parameter for this thesis.

⁶This was not considered in [5].

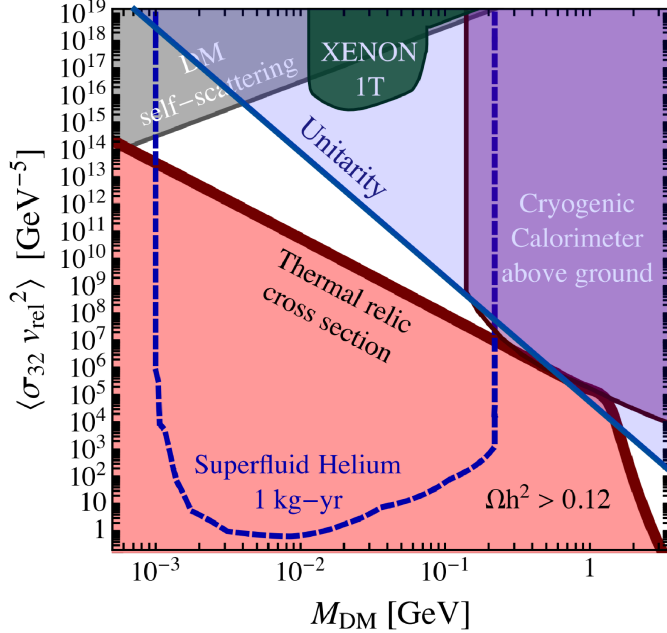


Fig. 2.3: Bounds from [5] in the nucleophilic case $\chi\chi p \rightarrow \chi p$. The gray region stems from self-scattering constraints in (2.10) [49], and the red region corresponds to a numerical calculation of (2.8) with the thick dark-red line indicating 100% Co-SIMP DM. The green and purple regions show constraints from XENON1T [29] and a cryogenic calorimeter [66], respectively. A projected constraint from superfluid helium (dashed dark blue) assumes a 1 kg-yr exposure with 1 MeV threshold. Additionally, the blue region indicates the unitarity bound from (2.12), overlaid as a power-law approximation. Note that this is not exact.

These constraints on the nucleophilic case are shown in Fig. 2.3—taken from the original Co-SIMP publication [5]—where we have overlaid the unitarity bound from (2.12). We note that the unitarity bound does not affect the existing limits on the leptophilic case in [5]. The goal is to investigate whether the CRDM mechanism—to be introduced in detail in Chapter 3—can exclude the currently viable region $m_\chi \in [10^{-3}, 0.2] \text{ GeV}$ in this plot, without relying on future experiments. We note that the Ωh^2 constraint shown here lies above the analytic bound in (2.8). This discrepancy arises because (2.8) assumes universal couplings of χ to all kinematically allowed SM particles, whereas the numerical calculation in Fig. 2.3 includes only proton interactions, which in turn requires a larger cross section for sufficient annihilation. For $m_\chi \gtrsim 2m_p$ this constraint becomes much weaker due to enabling $\chi\chi \rightarrow \chi\bar{p}p$ in this region, allowing the Co-SIMPs to reduce their comoving number density more efficiently to align with the required $\Omega h^2 \leq 0.12$. As shown, the unitarity constraint is strong enough to nullify the detector-based bounds from XENON1T, and only a minor portion of the cryogenic calorimeter remains restrictive. As such, we will omit these from the exclusion plots presented in Chapter 4. However, for the case of the Ωh^2 bound, we do not have access to the relevant data, nor the simulation which generates them. As such, when we present our exclusion limits, we approximate these results using simple power-law fits based on Fig. 2.3.

The introduction of leptophilic Co-SIMPs coincided with the reported excess of low-energy recoil events by the XENON1T experiment [67], and was therefore noted as a potential explanation in the original proposal. This gave Co-SIMPs an increased amount of attention at the time. While the excess was initially consistent with the spectrum expected from DM-electron scattering, subsequent experiments—such as its successor

XENONnT—have not observed similar features [68]. It is now widely believed that the XENON1T excess was most likely caused by an unaccounted-for background, e.g., trace tritium contamination, rather than a genuine signal of new physics.

Nonetheless, the Co-SIMP mechanism offers a well-motivated alternative to the SIMP framework. By including co-annihilation into the thermal history, it relaxes the minimal SIMP model’s stringent self-interaction requirement while preserving a viable relic abundance and allowing for sizable interactions with the Standard Model. This makes Co-SIMPs more adaptable to observational constraints and potentially detectable through both direct and indirect signatures, including those induced by cosmic-ray interactions—the primary focus of the following chapters.

Chapter 3

Cosmic Ray Upscattering

Cosmic rays (CRs) are energetic particles originating from high-energy astrophysical phenomena, including supernova remnants, active galactic nuclei, and pulsars. As they travel through space, CRs interact with various media such as interstellar gas, cosmic microwave background photons, and potentially even dark matter. If DM interacts with CRs, these interactions can transfer significant energy to otherwise non-relativistic DM particles, generating a population of *cosmic-ray-boosted dark matter* (CRDM), originally introduced in [4]. This mechanism enables new probes of light DM through nuclear recoils, independent of the velocity ceiling imposed by the halo distribution.

Since its inception, CRDM has been extensively studied, including improvements by incorporating effects like deep inelastic scattering at higher energies [7], and performing detailed analyses addressing the largest uncertainties associated with CRDM [36]. To date, this mechanism has been used to complement existing constraints for explicit models such as puffy DM [69].

The purpose of this chapter is to outline the fundamental mechanism behind CR upscattering, where CR interactions give rise to a secondary component of energetic DM particles, and to then apply this to Co-SIMPs in Chapter 4. Unlike the non-relativistic DM component that constitutes the Galactic halo, low mass CRDM can acquire sufficient kinetic energy to produce observable signals in direct detection experiments. This allows for novel experimental probes of DM–SM interactions, particularly for sub-GeV mass DM candidates.

This chapter begins by introducing the general properties of cosmic rays, focusing on their flux spectrum, in particular how to distinguish the local CR spectrum from the interstellar cosmic-ray flux. This is followed by a derivation of the CRDM flux spectrum resulting from CR–DM interactions. The effects of form factors and coherent enhancement in composite interactions are briefly addressed, since the most relevant species for CRDM are composite systems. We then examine the major blind spot of DD experiments caused by attenuation due to interactions with the Earth’s atmosphere and crust. Finally, we outline how the incident CRDM flux can be translated to recoil rates in the detector and connected to conventional DD constraints.

3.1 Interstellar Cosmic-Ray Flux Energy Spectrum

To better understand the phenomena we will encounter, it is vital to take a detailed look at the source of CRDM: the interstellar cosmic-ray (ICR) flux energy spectrum. CRs are produced by various phenomena, from some of the most energetic processes in the universe, such as gamma-ray bursts [70], down to relatively mundane phenomena like

3.1 Interstellar Cosmic-Ray Flux Energy Spectrum

solar activity. Due to the vast range in intensity of these production mechanisms, CRs span an enormous energy range, from a few MeV up to 10^{17} eV and beyond [71].

A substantial fraction of CRs observed near Earth originates from the Sun [72]. These MeV-scale solar CRs, produced during events such as solar flares and coronal mass ejections, dominate the spectrum below a few GeV. However, they are largely confined by the heliosphere and therefore do not contribute significantly to the interstellar cosmic-ray (ICR) flux. For CRDM studies, the relevant flux is the ICR, which originates outside the solar system and arises from galactic sources such as pulsars, supernovae, and other high-energy environments.

The ICR flux can be further categorized into two subsets: galactic CRs and cosmological/extragalactic CRs, distinguished by whether they are confined by the galactic magnetic field. The ultra-relativistic component typically originates from extragalactic sources and can traverse intergalactic distances [73], while galactic CRs are accelerated by astrophysical sources and remain trapped within the Milky Way. For the energy scales relevant to this work—since we neglect high-energy effects such as deep inelastic scattering within the halo—the galactic component is the dominant contributor.

To distinguish the ICR flux from the observed CR flux, one must account for the solar modulation effect. The solar wind and heliospheric magnetic field affect the spectrum of incoming cosmic-rays, with the effect becoming stronger at lower energies. This effect can be modeled using the force-field approximation, where the observed flux Φ_ψ^{obs} at Earth is related to the interstellar flux Φ_ψ^{ICR} by [74]

$$\Phi_\psi^{\text{obs}}(\bar{T}_\psi) = \frac{\bar{T}_\psi(\bar{T}_\psi + 2m_\psi)}{(\bar{T}_\psi + \phi)(\bar{T}_\psi + \phi + 2m_\psi)} \times \Phi_\psi^{\text{ICR}}(\bar{T}_\psi + \phi). \quad (3.1)$$

Here, \bar{T}_ψ is the kinetic energy per nucleon, and ϕ is the solar modulation potential, typically at the GeV scale and varying with the solar cycle [72]. This correction is particularly important for low-energy CRs, whose energies $\lesssim 1$ GeV are heavily suppressed by solar modulation. Above these energies, the modulation effect diminishes, and the flux approaches the interstellar level.

Additionally, experiments such as the Voyager probes—currently operating at the outer reaches of the solar system—provide invaluable data to differentiate between solar and interstellar cosmic-ray contributions. Since the detectors on the Voyager probes measure the CR flux beyond the heliospheres influence, they offer an unmodulated view of the ICR spectrum. Voyager’s observations confirm the transition from solar-modulated CRs to the unmodulated ICR flux, particularly in the energy region where the solar wind’s influence becomes insignificant [72]. This data, together with measurements from ground-based and near-Earth detectors, allows precise modeling of how the solar modulation effect varies over time. By comparing local experimental observations with Voyager data, it is possible to reconstruct the ICR spectrum from the locally measured CR spectrum. This distinction is crucial for CRDM studies since the relevant flux spectrum for dark matter upscattering originates from the ICR, rather than solar-modulated CRs within the solar system.

Fig. 3.1, taken from [72], illustrates the measured cosmic-ray energy spectrum¹ for the proton, highlighting the distinction between solar and interstellar contributions. Here we see that the solar modulation in (3.1) can be used to accurately describe the local CR spectrum. While at further distances from the sun, i.e. setting $\phi = 0$, one recovers

¹Note that E in Fig. 3.1 denotes the kinetic energy of the CR species, not its total energy; this is a common convention in cosmic-ray literature.

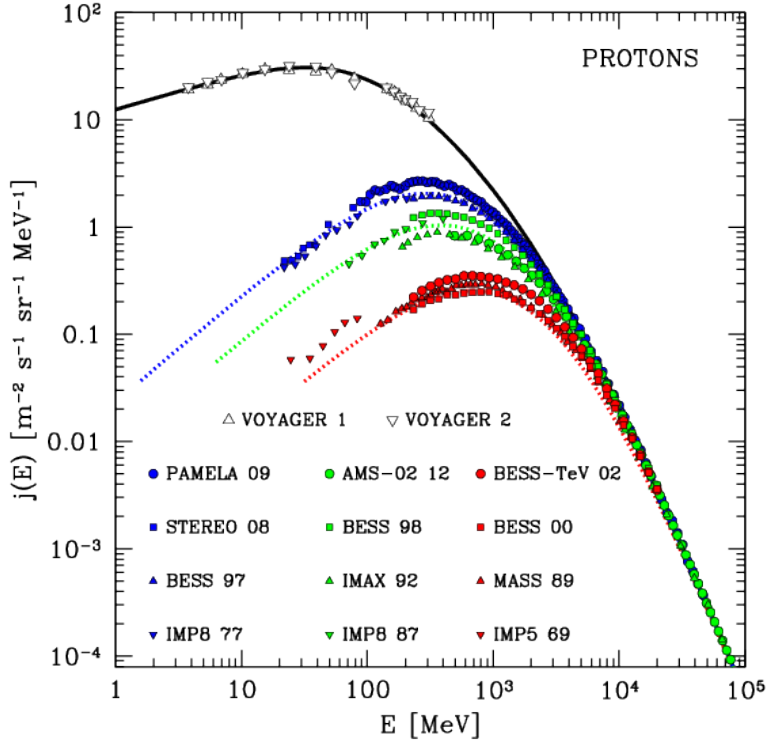


Fig. 3.1: Proton CR flux energy spectrum per steradian, $j(E) \equiv d\Phi_p/(dT_p d\Omega)$, measured both non-locally (white triangles with data from [75] and [76]) via the Voyager probes along with local measurements from PAMELA 09 [77]; STEREO 08 and IMP8 87 [78]; BESS 97, 98, -TeV 02, 00 [79]; IMP8 77 [80]; AMS-02 12 [81]; IMAX 92 [82]; MASS 89 [83]; and IMP5 69 [84]. The black solid line is an analytical representation of the unmodulated CR spectrum, while the colored dotted lines are computed with the modulation potential $\phi \in \{0.6, 0.8, 1.4\}$ GeV. The colors red, green and blue correspond to epochs of maximum, intermediate, and minimal solar activity, respectively. This figure is taken from [72], which adapts a plot originally published in [85].

the unmodulated CR flux, corresponding to the ICR flux. As seen in the figure, the solar modulation primarily affects lower energy CRs and is accurately described by (3.1). At higher energies, the modulated flux and ICR flux coincide, following a power-law spectrum $d\Phi_\psi/dT_\psi \propto T_\psi^{-\gamma}$ with a spectral index $\gamma \approx 2.7$ in the energy range below the knee at $T_\psi \gtrsim 10^5$ MeV.

With the above techniques, the ICR flux is well established. We adopt the parametrization in DarkSUSY from [86], shown in Fig. 3.2. In this work, we consider only the four most relevant species for CR upscattering, $\psi \in \{p, {}^4\text{He}, {}^{12}\text{C}, {}^{16}\text{O}\}$ [7], since the CR flux spectra for higher- Z species suffer from large uncertainties. For low DM masses in elastic scattering, the inclusion of heavier CR species can enhance the CRDM flux by up to $\sim 50\%$, as shown in [36]. As we will see later, including heavier species is negligible for nucleophilic Co-SIMPs, resulting in $\mathcal{O}(10^{-4})$ corrections. This feature generalizes to all particle-producing CRDM models, as it is an inherently kinematic consequence.

3.2 CRDM Flux

We now consider how this ICR flux induces a corresponding CRDM flux. In the following, we label the initially at-rest DM particle as χ and the incoming cosmic ray as ψ . We

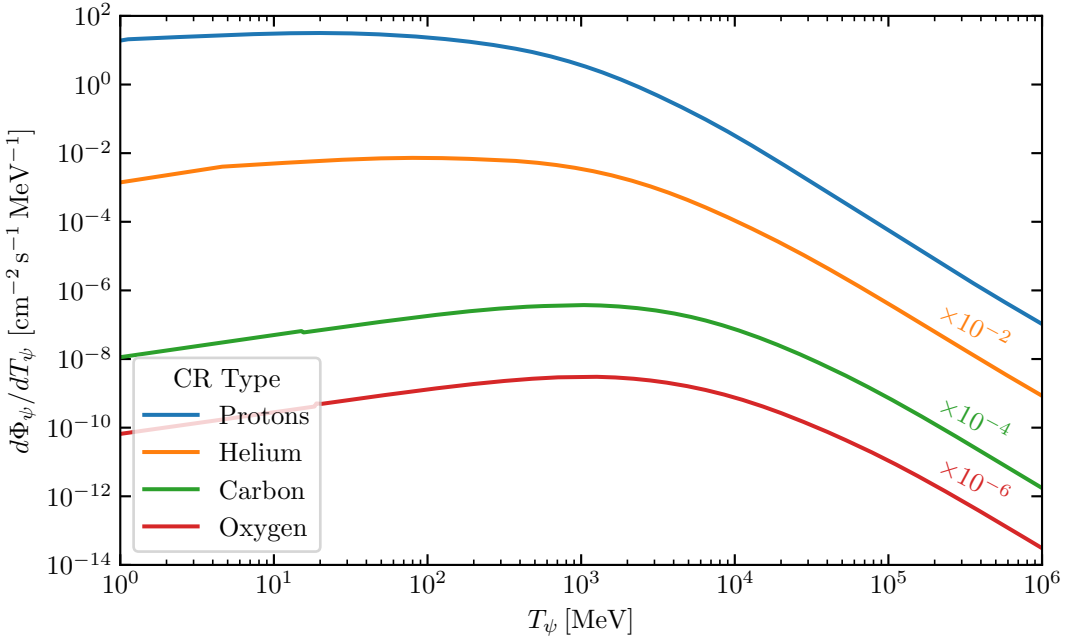


Fig. 3.2: Tabulated ICR flux which has been implemented in `DarkSUSY` based on the work in [86]. This includes the CR species $\psi \in \{p, {}^4\text{He}, {}^{12}\text{C}, {}^{16}\text{O}\}$. For visual clarity, we also multiply each flux (with the exception of the proton) by the factor above each line to avoid overlap.

assume a population of N_χ target particles χ , and that the interaction produces some final state X , in which we restrict ourselves to the case where χ appears in the final state—otherwise, there would be no resulting flux of particle χ .

The total rate of scattering in the rest frame of the target particles is²

$$\tilde{\Gamma}_{\chi\psi \rightarrow X} = N_\chi \sigma_{\chi\psi \rightarrow X} \Phi_\psi, \quad (3.2)$$

where $\sigma_{\chi\psi \rightarrow X}$ is the integrated cross section, and Φ_ψ is the flux of particle ψ . However, this expression averages over all kinematic configurations, and is therefore insufficient when energy-dependent features of the interaction are relevant. In particular, we are interested in the energy spectrum of the upscattered particle χ , which requires working with its corresponding differential form.

Given an energy density ρ_χ , the number of χ targets within an infinitesimal volume dV is $dV \rho_\chi / m_\chi$. The relevant differential cross section is $d\sigma_{\chi\psi \rightarrow X} / dT_\chi$ —where T_χ is the kinetic energy of particle χ *after* the interaction has occurred—and the differential flux of incoming particles with kinetic energy T_ψ is $d\Phi_\psi / dT_\psi$. Thus, the differential rate of scattering is given by

$$\frac{d^3 \tilde{\Gamma}_{\chi\psi \rightarrow X}}{dT_\chi dT_\psi dV} = \frac{\rho_\chi}{m_\chi} \frac{d\sigma_{\chi\psi \rightarrow X}}{dT_\chi} \frac{d\Phi_\psi}{dT_\psi}. \quad (3.3)$$

To determine the flux of particle χ with kinetic energy T_χ after scattering, we integrate (3.3) over the ensemble volume and the incoming CR energy T_ψ . Additionally, if the distribution of χ is isotropic in the observer's frame, and the particles are on average a distance r away, the observed differential flux would be equal to the differential flux

²The tilde distinguishes the total interaction rate from the per-target rate, defined by $\Gamma \equiv \tilde{\Gamma}/N_T$.

exiting a sphere of radius r , which is given by $4\pi r^2 d\Phi_\chi/dT_\chi$. For any given T_χ , only incoming particles with kinetic energy $T_\psi \geq T_\psi^-$ could have contributed to the process, where $T_\psi^-(T_\chi)$ is determined by kinematic constraints which depend on the final state X : this imposes a lower integration bound. As an example, in the case of elastic scattering, $X = \chi\psi$, this threshold is [4]

$$T_{\psi,\text{ES}}^- = \frac{T_\chi}{2} - m_\psi + \sqrt{\left(\frac{T_\chi}{2} - m_\psi\right)^2 + \frac{T_\chi}{2m_\chi}(m_\psi + m_\chi)^2}. \quad (3.4)$$

Including all possible CR particles that interact with χ , the flux observed at an average distance r from the source is³

$$\frac{d\Phi_\chi}{dT_\chi} = \int_V \frac{dV}{4\pi r^2} \sum_\psi \int_{T_\psi^-}^\infty dT_\psi \frac{d^3\tilde{\Gamma}_{\chi\psi \rightarrow X}}{dT_\chi dT_\psi dV} = \int_V \frac{dV}{4\pi r^2} \frac{\rho_\chi}{m_\chi} \sum_\psi \int_{T_\psi^-}^\infty dT_\psi \frac{d\sigma_{\chi\psi \rightarrow X}}{dT_\chi} \frac{d\Phi_\psi}{dT_\psi}. \quad (3.5)$$

Given that X contains n copies of χ , we must multiply (3.5) by n . If we neglect any secondary collision between the upscattered particle and the medium it travels through, these DM particles would travel in a straight line toward Earth. Thus, we can simplify the volume integral to a one-dimensional line-of-sight (l.o.s) integral:

$$\frac{d\Phi_\chi}{dT_\chi} = \int_{\text{l.o.s}} d\ell \frac{\rho_\chi}{m_\chi} \sum_\psi \int_{T_\psi^-}^\infty dT_\psi \frac{d\sigma_{\chi\psi \rightarrow X}}{dT_\chi} \frac{d\Phi_\psi}{dT_\psi}. \quad (3.6)$$

In the context of CRDM, $\Phi_\psi = \Phi_\psi(\mathbf{r})$ and $\rho_\chi(\mathbf{r})$ in (3.6) are the position-dependent CR flux and DM energy density surrounding a region around our solar system—the volume from which the initially at-rest DM particles originate—and \mathbf{r} is the distance to the Galactic Center. These two quantities are generally poorly constrained and represent the main astrophysical uncertainties in the CRDM framework. We therefore aim to relate them to local observations within the solar system.

Following the procedure in [36], we rewrite (3.6) as

$$\frac{d\Phi_\chi}{dT_\chi} = \frac{\rho_\chi^{\text{loc}}}{m_\chi} \sum_\psi \int_{T_\psi^-}^\infty dT_\psi \frac{d\sigma_{\chi\psi \rightarrow X}}{dT_\chi} \frac{d\Phi_\psi^{\text{loc}}}{dT_\psi} K_\psi(T_\psi). \quad (3.7)$$

Here, the superscript “loc” refers to the local interstellar value of the quantity, and the kernel $K_\psi(T_\psi)$ encodes deviations in the ICR flux and the DM densities along the line of sight:

$$K_\psi(T_\psi) \equiv \left[\rho_\chi^{\text{loc}} \frac{d\Phi_\psi^{\text{loc}}}{dT_\psi} \right]^{-1} \int \frac{d\Omega}{4\pi} \int_{\text{l.o.s}} d\ell \rho_\chi \frac{d\Phi_\psi}{dT_\psi}. \quad (3.8)$$

This captures all the astrophysical information beyond the local system. Furthermore, we note that the flux in (3.7) is now the angular-averaged CRDM flux due to the solid angle integration in K_ψ . Defining

$$D_{\text{eff}}(T_\chi) \equiv \frac{\sum_\psi \int_{T_\psi^-}^\infty dT_\psi K_\psi(T_\psi) \frac{d\sigma_{\chi\psi \rightarrow X}}{dT_\chi} \frac{d\Phi_\psi^{\text{loc}}}{dT_\psi}}{\sum_\psi \int_{T_\psi^-}^\infty dT_\psi \frac{d\sigma_{\chi\psi \rightarrow X}}{dT_\chi} \frac{d\Phi_\psi^{\text{loc}}}{dT_\psi}}, \quad (3.9)$$

³Provided that the observer is at rest with respect to the initial χ .

the flux can be written on the compact form

$$\frac{d\Phi_\chi}{dT_\chi} = D_{\text{eff}}(T_\chi) \frac{\rho_\chi^{\text{loc}}}{m_\chi} \sum_\psi \int_{T_\psi^-}^\infty dT_\psi \frac{d\Phi_\psi^{\text{loc}}}{dT_\psi} \frac{d\sigma_{\chi\psi \rightarrow X}}{dT_\chi}. \quad (3.10)$$

At this point, all non-local information is encapsulated in the prefactor $D_{\text{eff}}(T_\chi)$. This parametrization is particularly effective since it captures the dominant uncertainties in the CRDM flux, whereas the local interstellar CR flux and DM energy density are relatively well constrained. Thus, the single function D_{eff} effectively encodes the entire astrophysical uncertainty of the mechanism. From its definition, we see that D_{eff} is a weighted average of K_ψ , where the weights are given by the product of $d\Phi_\psi^{\text{loc}}/dT_\psi$ and $d\sigma_{\chi\psi \rightarrow X}/dT_\chi$.

To better understand the behavior of D_{eff} , we consider simplified cases. For instance, if the CR flux is assumed to be spatially uniform within the magnetic halo we take our CRDM to originate from, then D_{eff} reduces to a T_χ independent factor, depending only on the DM density profile and the integration region:

$$D_{\text{eff}} = \int \frac{d\Omega}{4\pi} \int_{\text{l.o.s}} d\ell \frac{\rho_\chi}{\rho_\chi^{\text{loc}}}. \quad (3.11)$$

This corresponds to the effective distance or diffusion volume commonly adopted in the CRDM literature. If we further assume $\rho_\chi = \rho_\chi^{\text{loc}}$, then D_{eff} simply reduces to the average distance at which the CR–DM interactions occur. It may then be interpreted as the characteristic size of the region over which the source density of χ is approximately equal to the local density ρ_χ^{loc} , assuming the CR flux is homogeneous within this region [87]. Since the Milky Way is a disk-like shape, the main uncertainty of this parameter comes from the vertical extend of the cylindric confinement zone of Galactic CRs [7]. In the literature, typical benchmark values are $D_{\text{eff}} \in [1, 10]$ kpc, with the lower end corresponding to an ultra-conservative choice.

Relaxing this simplification, we instead consider a CR flux whose spatial dependence can be factored out:

$$\frac{d\Phi_\psi(\mathbf{r})}{dT_\psi} = g_\psi(\mathbf{r}) \frac{d\Phi_\psi^{\text{loc}}}{dT_\psi}. \quad (3.12)$$

Under this assumption, K_ψ reduces to

$$K_\psi(T_\psi) = \int \frac{d\Omega}{4\pi} \int_{\text{l.o.s}} d\ell \frac{\rho_\chi}{\rho_\chi^{\text{loc}}} g_\psi(\mathbf{r}). \quad (3.13)$$

This factorization is motivated by observations of the angular spectrum of CRs, which suggest an excess originating from the direction of the Galactic Center, where the matter density is higher [88]. An in-depth analysis of the diffusion parameter under this assumption was carried out in [36]. They found that the energy dependence of the K_ψ factors is largely independent of the CR species: starting at ~ 4.5 kpc for 1 MeV/nucleon, peaking at 10 kpc near 1 GeV/nucleon, and asymptotically approaching $D_{\text{eff}} \sim 8.7$ kpc for $T_\chi \gtrsim 10$ GeV/nucleon. Unlike K_ψ , which is purely astrophysical, D_{eff} also depends on the CR–DM differential cross section. For elastic scattering, it reaches a nearly constant value $D_{\text{eff}} \simeq 9$ kpc for $T_\chi \gtrsim 1$ GeV [36].

Due to the sheer computational cost required to calculate (3.9)—even with the simplifying assumption in (3.12)—we will follow the common choice in the literature: keeping D_{eff} as a constant, using the result from [36] as a guideline. Typically $D_{\text{eff}} = 10$ kpc is a common and realistic benchmark. We will conservatively set $D_{\text{eff}} = 5$ kpc, due to uncertainties in how inelastic processes affect this effective parameter.

3.3 Composite Interactions

Since the most dominant CR species are all composite systems, their interactions cannot accurately be modeled using point-like approximations. Thus, we will briefly introduce the relevant features of composite interactions, focusing on form factors and coherent enhancement, both of which are essential for a realistic treatment of CRDM.

Form Factors

In quantum field theory, vertex corrections imply that the full matrix element \mathcal{M} can be written as the product of a point-like matrix element \mathcal{M}_0 and a form factor G [89, 90]. The form factor, due to Lorentz invariance and the Ward identity, can only depend on the space-like momentum transfer q^2 , and must satisfy the limits $G(q^2 = 0) = 1$ and $G(q^2 \rightarrow -\infty) = 0$ [89]. For particles that interact via multiple gauge groups, or have internal structure, the form factors are not perturbatively calculable [90]. Since this applies to all relevant CR species, experimental input is required. However, we will briefly consider an alternative approach.

In the non-relativistic limit $|\mathbf{q}|/q^0 \ll 1$, the form factor may be defined as the normalized Fourier transform of the spatial distribution $\rho(\mathbf{x})$ of the composite system:⁴

$$G(|\mathbf{q}|) \equiv \frac{\int d^3x e^{i\mathbf{q}\cdot\mathbf{x}}\rho(\mathbf{x})}{\int d^3x \rho(\mathbf{x})}. \quad (3.14)$$

Assuming spherical symmetry, as is often the case, the form factor simplifies to

$$G(|\mathbf{q}|) = \frac{1}{|\mathbf{q}|} \frac{\int_0^\infty dr r \sin(|\mathbf{q}|r)\rho(r)}{\int_0^\infty dr r^2 \rho(r)}. \quad (3.15)$$

To proceed analytically, a choice for ρ must be made. An exponentially decaying distribution, $\rho(\mathbf{x}) = Ae^{-\Lambda|\mathbf{x}|}$, provides both simplicity and physical relevance. Inserting this into (3.14), the integral simplifies to:

$$G(|\mathbf{q}|) = (1 + |\mathbf{q}|^2/\Lambda^2)^{-2}. \quad (3.16)$$

This is known as the non-relativistic electromagnetic dipole form factor. Motivated by the fact that the full form factor must depend only on q^2 , adopting the ansatz that Lorentz invariance can be approximately restored by promoting $|\mathbf{q}| \rightarrow Q \equiv \sqrt{-q^2}$, giving the well-known result

$$G(Q^2) = (1 + Q^2/\Lambda^2)^{-2}. \quad (3.17)$$

This final argument lacks rigor, and one could easily find counterexamples, such as adding another function $f(q^2)$ to the above which satisfies $f(Q^2 = 0) = f(Q^2 \rightarrow \infty) = 0$, and is finite otherwise.⁵ This function would be invisible in the low energy limit, and would satisfy the requirement from QFT that $G(Q^2 \rightarrow \infty) = 0$.

The reason for this is simple: we performed this ‘derivation’ in reverse. Experimentally, these form factors are not derived from the spatial or charge distribution, but instead at the level of the differential cross section $d\sigma/dQ^2$. By obtaining the analytic tree-level result for this quantity in the point-like limit, and then taking the ratio of the measured

⁴Experimentally, such a spatial distribution is not directly accessible. Therefore, one often takes $\rho(\mathbf{x})$ to represent the more tractable charge distribution.

⁵For example, $f(Q^2) = -a/(Q^2/\Lambda^2 + \Lambda^2/Q^2)$ with $a > 0$.

differential cross section and the tree-level result, one arrives at the form factor. In doing so, the spatial distribution becomes a post hoc explanation—an ansatz chosen to reproduce experimental behavior, not a fundamental input. For the proton, this ratio approximately yields the result in (3.17) with $\Lambda_p = 0.843 \text{ GeV}$, which provides an excellent fit to current data up to $Q \sim 1 \text{ GeV}$, and agreeing within 10% for $Q^2 \leq 10 \text{ GeV}^2$ [91, 92]. This correspondence with the experimental results is what justifies our modeling of the proton's spatial distribution with an exponentially damped profile. Given its empirical success, this work adopts (3.17) for the proton.

For more complex composite systems, such as ${}^4\text{He}$, ${}^{12}\text{C}$, and ${}^{16}\text{O}$ nuclei, the analysis becomes more intricate and is not captured by the exponentially damped distribution. In these cases, the structure of the nucleus is not well described by the dipole form factor, and more complicated form factors are needed. As such, for the heavier CR species we will make use of the tabulated form factors in **DarkSUSY** [6], which are based on data from [93].

Coherent Enhancement

In scenarios where a point-like particle interacts with a composite system, it effectively couples to each of its point-like constituents. This feature is known as coherent enhancement. As we will show, coherence can significantly amplify the total scattering amplitude, particularly for elastic scattering. What follows is an illustrative argument for the origin of coherent enhancement; it should not be regarded as a complete or rigorous proof.

To model this effect, we begin by considering a composite target consisting of A individual constituents, each with a point-like interaction matrix element \mathcal{M}_{i0} . If the interaction is coherent—meaning that the momentum transfer q is sufficiently small such that the de Broglie wavelength of the incoming particle exceeds the size of the composite system, R —then the amplitudes from all constituents add constructively. The total matrix element then takes the form

$$\mathcal{M} = \sum_{i=1}^A \mathcal{M}_{i0} e^{i\mathbf{q} \cdot \mathbf{x}_i}, \quad (3.18)$$

where \mathbf{x}_i denotes the position of the i -th constituent with respect to some arbitrary reference position. If we further take the spatial distribution of each constituent of the nucleus to be localized, i.e.,

$$\rho_s(\mathbf{x}) = \sum_{i=1}^A \delta(\mathbf{x} - \mathbf{x}_i), \quad (3.19)$$

and insert this into (3.14), one arrives at

$$G(|\mathbf{q}|) = \frac{1}{A} \sum_{i=1}^A e^{i\mathbf{q} \cdot \mathbf{x}_i}. \quad (3.20)$$

If the interaction is approximately uniform across the nucleus and the interaction strength is the same for all nucleons, i.e., $\mathcal{M}_0 \equiv \mathcal{M}_{i0} = \mathcal{M}_{j0}$ for all i and j , then (3.18) becomes

$$\mathcal{M} = \mathcal{M}_0 \sum_{i=1}^A e^{i\mathbf{q} \cdot \mathbf{x}_i}. \quad (3.21)$$

Inserting the sum from (3.20) then gives an approximation for the coherently enhanced matrix element:

$$\mathcal{M} = A \mathcal{M}_0 G(|\mathbf{q}|), \quad |\mathbf{q}|R \ll 1. \quad (3.22)$$

Thus, for sufficiently small $|\mathbf{q}|R$, where $G(|\mathbf{q}|) \approx 1$, the enhancement at the cross section level scales as A^2 , significantly boosting the interaction probability compared to a naive sum over A independent scatterings. This enhancement is particularly relevant for halo DM detection and neutrino–nucleus scattering, where the momentum transfers are typically very low and the coherence condition is well satisfied. In such regimes, where detectors are sensitive to low recoil energies, one typically retains the coherent enhancement factor throughout, while using the full kinematics as if the interaction were point-like with the entire nucleus: this also applies at the level of the matrix element.

For larger $|\mathbf{q}|R \sim 1$, the interaction transitions to the incoherent regime, where individual scatterings contribute independently, as discussed in [94], suggesting a scaling $\sigma \propto A$. When $|\mathbf{q}|R > 1$, the scattering begins to occur at the level of a single constituent, effectively interacting with just one particle. For example, in a nucleus, at sufficiently high momentum transfers the de Broglie wavelength of the incoming particle becomes small enough that it only interacts with a single nucleon—typically once the binding energy of the nucleus becomes negligible. In this case, we model the interaction using the kinematics and form factors of a proton rather than those of the full nucleus. At $|\mathbf{q}|R \gg 1$, the probe begins to resolve the internal structure of the proton itself, transitioning to scattering off individual quarks, where the point-like limit becomes valid.

In summary, scattering on composite systems require careful consideration before applying standard formulas. One must consider the energy scales probed by a given detector and adjust the relevant kinematics and dynamics accordingly. For this thesis, in xenon based detectors we will apply the $|\mathbf{q}|R \ll 1$, and for higher energy detectors such as MiniBooNE and Borexino we consider the $|\mathbf{q}|R > 1$ case, meaning scattering off individual nucleons. For the interaction in the halo we apply coherent enhancement to all applicable CR species, and use their respective form factor. As mentioned earlier, the $\mathcal{O}(1\%)$ correction from including heavier CRs than the proton makes any uncertainty from incoherent interactions in the DM halo negligible. Further, we discuss the details of including form factor in the detector in Section 4.4. These choices follow the logic adopted in DarkSUSY [6] based on the work in [4, 7].

3.4 Attenuation

For very large cross sections, terrestrial DD contains a blind spot to DM. This stems from scattering on nuclei within the overburden—the Earth’s atmosphere and crust above a given detector—which attenuates the CRDM flux; that is, it reduces both the flux’s energy and overall intensity before reaching the detector. For detectors positioned far underground, e.g., the XENON1T detector at a depth $z \sim 1.4$ km, this is particularly relevant. To model this effect, we can relate the initial kinetic energy T_χ at the top of the atmosphere to the energy T_χ^z at depth z via the energy loss equation [4, 7]:⁶

$$\frac{dT_\chi^z}{dz} = - \sum_N n_N \int d\Pi_f \frac{d\sigma_{\chi N \rightarrow X}}{d\Pi_f} \omega_\chi. \quad (3.23)$$

⁶The notation is slightly generalized compared to the corresponding result in [7].

Here, N are the nuclear species in the overburden that CRDM must traverse through, n_N is the number density of N , z is the depth, ω_χ is the energy lost by a DM particle in a single collision, and $d\Pi_f$ is the Lorentz invariant phase space in (2.7). Eq. (3.23) applies to any process where $\chi \in X$, including inelastic or non-elastic $2 \rightarrow 3$ scattering, naturally, provided χ survives the interaction and continues to propagate.

To motivate (3.23), we define $\omega_\chi \equiv \Delta T_\chi = T_\chi^{\text{in}} - T_\chi^{\text{out}}$ as the energy lost by a CRDM particle in a single interaction. This quantity depends on the final state kinematics and is not fixed, varying across the physically accessible phase space. A DM particle traversing an infinitesimal path length dz has a probability $n_N \sigma_{\chi N \rightarrow X} dz$ to scatter on a nuclear species N with number density n_N and cross section $\sigma_{\chi N \rightarrow X}$. Summing over all species gives the total scattering probability over this distance:

$$\sum_N n_N \sigma_{\chi N \rightarrow X} dz. \quad (3.24)$$

The corresponding energy loss is the product of this probability with the average energy loss per interaction:

$$dT_\chi^z = - \sum_N n_N \sigma_{\chi N \rightarrow X} \langle \omega_\chi \rangle dz, \quad (3.25)$$

where the average is taken over the allowed final states weighted by the differential cross section:

$$\langle \omega_\chi \rangle \equiv \frac{\int d\Pi_f \frac{d\sigma_{\chi N \rightarrow X}}{d\Pi_f} \omega_\chi}{\int d\Pi_f \frac{d\sigma_{\chi N \rightarrow X}}{d\Pi_f}} = [\sigma_{\chi N \rightarrow X}]^{-1} \int d\Pi_f \frac{d\sigma_{\chi N \rightarrow X}}{d\Pi_f} \omega_\chi. \quad (3.26)$$

Inserting (3.26) into (3.25) yields the expression in (3.23). This derivation neglects any angular deflection of the DM's path, assuming it continues approximately along its original trajectory. The assumption becomes less accurate when $m_N \gtrsim m_\chi$, where sizable deflections can accumulate. A more rigorous treatment would account for such effects, e.g., through Monte Carlo simulations, so (3.23) should be regarded as an approximation.

In CRDM's inception, attenuation was modeled by assuming the cross section in (3.23) was constant, corresponding to its non-relativistic limit [4]. Later refinements included relativistic effects, form factors, and high energy effects such as deep inelastic scattering [7]. When these effects are taken into account, the overall attenuation becomes much weaker than predicted by the non-relativistic cross section, thereby allowing for significantly stronger CRDM bounds.

Attenuation for inelastic processes is more complicated, particularly in scenarios where the low-energy flux can increase due to scattering—as in the $2 \rightarrow 3$ Co-SIMP process considered in our CRDM flux. Nevertheless, we will show that this complication can be neglected, since attenuation for the relevant cross sections is too strong to allow Co-SIMPs to pass through the overburden and reach the detector, as will be discussed in Section 4.5. Furthermore, at sufficiently high energies, the CRDM flux may enter regimes where scattering with the overburden is no longer purely elastic, and effects such as hadronic resonances and deep inelastic scattering become important.

While we do not directly implement attenuation for the $2 \rightarrow 3$ process, we later include a two-loop induced elastic scattering channel that determines the observable signal and must be attenuated accordingly. As such, we will outline the general strategy for attenuation in form factor-dependent elastic scattering, $X = \chi N$, where we neglect exotic effects such as deep inelastic scattering. Such effects will be modeled with an

explicit flux cutoff $T_\chi^+ = 0.1 \text{ GeV}$, which has been shown to be a good approximation [7]. The results in this thesis are however obtained by making use of the full treatment implemented in `DarkSUSY`, based on the work of [7]. For a detailed description of the inelastic effects, along with the parameters used, we refer the reader to [7].

In the elastic case, (3.23) simplifies to

$$\frac{dT_\chi^z}{dz} = - \sum_N n_N \int_0^{\omega_\chi^+} d\omega_\chi \frac{d\sigma_{\chi N \rightarrow \chi N}}{d\omega_\chi} \omega_\chi, \quad (3.27)$$

where $\omega_\chi = T_N$ since the scattering is elastic, and the upper integration limit is given by

$$\omega_\chi^+ = T_N^{\max} = \frac{2m_N T_\chi^z (2m_\chi + T_\chi^z)}{(m_N + m_\chi)^2 + 2m_\chi T_\chi^z}, \quad (3.28)$$

obtained by inverting (3.4) with the relevant replacements. In practice, solving (3.27) exactly for each DM particle would be computationally expensive, especially for a general momentum-transfer-dependent differential cross section. Instead, we adopt an efficient numerical strategy implemented in `DarkSUSY` [6]. One begins by specifying the non-relativistic normalization of the cross section, σ_{NR} , along with a relativistic correction factor $\sigma/\sigma_{\text{NR}}$. For example, for a simple 4-point scalar interaction with coupling λ , these are

$$\sigma_{\text{NR}} = \frac{\lambda^2}{16\pi(m_\chi + m_N)^2} + \mathcal{O}(\lambda^3), \quad \frac{\sigma}{\sigma_{\text{NR}}} = \frac{(m_\chi + m_N)^2}{s}, \quad (3.29)$$

where s is the center-of-mass (CM) energy squared. Then, for each value of σ_{NR} , the equation is solved numerically across a range of incoming T_χ to determine the corresponding T_χ^z at depth z . The resulting mapping between T_χ and T_χ^z is stored in a lookup table. To simplify the integration, the energy loss equation is recast in terms of a rescaled ‘mass depth’ variable x , defined by

$$dx \equiv \rho(z) dz, \quad (3.30)$$

where $\rho(z)$ is the mass density of the overburden. We assume $\rho(z)$ to be constant, corresponding to a uniform medium. Since the Earth’s crust density varies little between the surface and detector depth, this is a reasonable approximation. With this, the (3.27) becomes

$$\frac{d \ln T_\chi}{dx} = - \frac{1}{T_\chi} \sum_N \frac{\rho_N}{m_N} \int_{\omega_\chi^-}^{\omega_\chi^+} d\omega_\chi \frac{d\sigma_{\chi N \rightarrow \chi N}}{d\omega_\chi} \omega_\chi, \quad (3.31)$$

where ρ_N is the mass density of nuclear species N . The lookup table is generated by numerically integrating (3.31) over a grid of T_χ . This provides an efficient interpolation between T_χ at the top of the atmosphere and T_χ^z at the detector depth.

We emphasize that this approach fully accounts for the energy dependence of the differential cross section, rather than assuming a constant cross section as in some simplified models. This gives a more accurate treatment of attenuation, particularly when the scattering is dominated by low-momentum transfers or suppressed by form factors. However, without the explicit cutoff on the CRDM flux, this prescription becomes overly lenient for the high-energy component of the CRDM flux, where relativistic corrections and form factor suppression significantly reduce the interaction rate in the overburden. At these scales, additional processes emerge that are not captured by elastic modeling—this

is precisely what the cutoff is intended to regulate. While more sophisticated than the constant cross section approximations, this section was intended to provide a schematic overview of attenuation. In this thesis, we make use of the full treatment, including quasi-inelastic scattering, hadronic resonances, and deep inelastic scattering, using the same parametrization implemented in `DarkSUSY`, based on [7].

3.5 Recoil Rates & Constraints

Given the flux of CRDM derived above, we now consider its scattering with a target nucleus N in a detector. Assuming the same interaction occurs—producing a final state X that includes N —and that the detector is at rest with respect to the galactic halo (from which the initial χ was at rest), the observable interaction rate is simply a relabeling of (3.3), integrated over the detector volume and over the observable nuclear recoil energies $T_N \in [T_N^-, T_N^+]$:

$$\begin{aligned}\tilde{\Gamma}_{\chi N \rightarrow X} &= \int_V dV \frac{\rho_N}{m_N} \int_{T_N^-}^{T_N^+} dT_N \int_{T_\chi^-}^\infty dT_\chi \frac{d\sigma_{\chi N \rightarrow X}}{dT_N} \frac{d\Phi_\chi}{dT_\chi} \\ &= N_T \int_{T_N^-}^{T_N^+} dT_N \int_{T_\chi^-}^\infty dT_\chi \frac{d\sigma_{\chi N \rightarrow X}}{dT_N} \frac{d\Phi_\chi}{dT_\chi}.\end{aligned}\quad (3.32)$$

We will follow the convention in [4], and instead report the interaction rate *per target nucleus*:

$$\Gamma_{\chi N \rightarrow X} \equiv \frac{\tilde{\Gamma}_{\chi N \rightarrow X}}{N_T} = \int_{T_N^-}^{T_N^+} dT_N \int_{T_\chi^-}^\infty dT_\chi \frac{d\sigma_{\chi N \rightarrow X}}{dT_N} \frac{d\Phi_\chi}{dT_\chi}.\quad (3.33)$$

When accounting for attenuation, the T_χ appearing in the differential cross section must be evaluated at T_χ^z , the kinetic energy of χ at detector depth z . This does not apply to the remaining T_χ in the expression, which refers to the pre-attenuation energy at the top of the atmosphere. However, since χ loses energy while traversing the overburden, the minimum energy required to induce a recoil T_N must be correspondingly larger. We therefore take $T_\chi^- = T_\chi(T_\chi^{z,-})$, where $T_\chi^{z,-}$ is the minimum post-attenuation energy needed to produce a nuclear recoil of energy T_N . In the elastic case, $T_\chi^{z,-}$ is obtained by solving (3.4) for T_χ^z and then numerically inverting the solution to (3.27) to recover the corresponding T_χ at the top of the atmosphere.

We now wish to connect the CRDM-induced interaction rates to conventional direct detection (DD) constraints. These are typically reported as limits on the spin-independent (SI) DM-nucleon cross section, $\sigma_{\text{DM}}^{\text{SI}}$, for WIMP-like dark matter masses $m_{\text{DM}} \sim 1 \text{ TeV}$. Since we can compute the expected recoil rate in the detector from CRDM, we follow the approach of [4] and reinterpret these conventional constraints by matching the expected number of events. To avoid potential confusion, we will label quantities relevant for conventional halo dark matter with the sub-/superscript DM, and the analogous CRDM quantities with χ .

Conventional DD relies on low-energy halo DM, for which the velocity is bounded by $v_{\text{DM}} < v_{\text{esc}} \simeq 530 \text{ km/s}$ [34]. This allows the DM velocity distribution $f(v)$ to be treated as non-relativistic, leading to a differential flux [4]

$$\frac{d\Phi_{\text{DM}}}{dT_{\text{DM}}} = \frac{\rho_{\text{DM}}^{\text{loc}}}{m_{\text{DM}}^2} f_{\text{NR}}(v),\quad (3.34)$$

where $\rho_{\text{DM}}^{\text{loc}} = 0.3 \text{ GeV/cm}^3$ is the local DM energy density. Assuming isotropic scattering, which yields a flat nuclear recoil distribution $d\sigma_{\text{DM},N}/dT_N = \sigma_{\text{DM},N}/T_N^{\max}$, the rate per target nucleus becomes [4]

$$\begin{aligned}\Gamma_N^{\text{DM}} &= \int_{T_N^-}^{T_N^+} dT_N \int_{T_{\text{DM}}^-}^{\infty} dT_{\text{DM}} \frac{d\Phi_{\text{DM}}}{dT_{\text{DM}}} \frac{\sigma_{\text{DM},N}}{T_N^{\max}(T_{\text{DM}})} \Theta[T_N^{\max}(T_{\text{DM}}) - T_N] \\ &\simeq \kappa (\bar{v} \rho_{\text{DM}})^{\text{loc}} \frac{\sigma_{\text{DM},N}}{m_{\text{DM}}} = \kappa (\bar{v} \rho_{\text{DM}})^{\text{loc}} \frac{\sigma_{\text{DM}}^{\text{SI}}}{m_{\text{DM}}} A_N^2 \left(\frac{m_N(m_{\text{DM}} + m_p)}{m_p(m_{\text{DM}} + m_N)} \right)^2.\end{aligned}\quad (3.35)$$

Here, \bar{v} is the mean DM velocity, and κ is an $\mathcal{O}(1)$ constant that depends on both the DM velocity distribution and the detector energy window. For a Maxwellian distribution,

$$\kappa = \exp \left[-\frac{2T_N^-}{\pi m_N \bar{v}^2} \right] - \exp \left[-\frac{2T_N^+}{\pi m_N \bar{v}^2} \right].\quad (3.36)$$

In the $m_N/m_{\text{DM}} \ll 1$ limit, then for the Standard Halo Model and XENON1T detector, which has $T_{\text{Xe1T}} \in [4.9, 40.9] \text{ keV}$ [29], this yields $\kappa \simeq 0.23$ [4]. In the final line of (3.35), the nuclear cross section is rewritten in terms of the SI DM–nucleon cross section. The A_N^2 factor reflects coherent enhancement from scattering off a nucleus with mass number A_N , and the kinematic prefactor accounts for the change in reduced mass relative to a proton target, i.e., $\mu_{\text{DM},N}^2/\mu_{\text{DM},p}^2$. In doing so, we approximated the neutron and proton masses as equal, $m_n \approx m_p$. Having fixed $\sigma_{\text{DM}}^{\text{SI}}$ using experimental upper bounds, and knowing all other parameters in (3.35), we determine the effective interaction rate Γ_N^{DM} that a CRDM signal cannot exceed—otherwise it would have been detected. This serves as the exclusion threshold in our reinterpretation:

$$\Gamma_{\chi N \rightarrow X} = \Gamma_N^{\text{DM}}.\quad (3.37)$$

Detector	m_T [GeV]	T_N^- [GeV]	T_N^+ [GeV]	z [m]	Γ_N^{DM} [1/s]
XENON1T	122.05	4.9×10^{-6}	4.08×10^{-5}	1400	$*3.74 \times 10^{-37}$
Darwin	122.05	$\dagger 1.0 \times 10^{-6}$	4.08×10^{-5}	1400	$*1.38 \times 10^{-39}$
Borexino	0.938	$\S 1.25 \times 10^{-2}$	$\S 0.25$	1400	1.89×10^{-39}
MiniBooNE	0.938	3.5×10^{-2}	1.4	3, $\ddagger 6$	1.54×10^{-32}

Table 3.1: Detector properties and derived 90% CL upper limits on interaction rates per target nucleus. T_N^- is the minimal threshold to produce a signal, while T_N^+ is the upper end of the default analysis window.

Table 3.1 summarizes the Γ_N^{DM} used in this work for various detectors. For XENON1T and Darwin, these rates are computed using (3.35) assuming the SHM. For MiniBooNE and Borexino, the event-counting method constitutes a reinterpretation of the following:

$$\Gamma_N^{\text{DM}} = \frac{n_{\text{events}}^{90\%}}{\epsilon n_T \Delta T}.\quad (3.38)$$

^{*} Assumes $m_\chi = 1 \text{ GeV}$ and the Standard Halo Model with the NFW profile in (2.2).

[†] Optimistic threshold; a conservative one is $4.9 \times 10^{-6} \text{ GeV}$.

[‡] Effective depth including atmospheric shielding.

[§] Quenched energy in scintillators. True recoil energy is obtained using `DarkSUSY`.

Here, $n_{\text{events}}^{90\%}$ is the 90% CL upper limit on observed events, ϵ is the detector efficiency, and ΔT is the exposure time. For more details, see the appendix in [4]. Note that Darwin is a future experiment, and we include its projected sensitivities. The experiments can be broadly categorized by ‘shallow vs. deep location’, ‘low vs. high energy’, ‘heavy vs. light targets’ and ‘strong vs. weak constraints’. The effects of each of these categories can be used to explain various results which we see in Chapter 4, along with evaluating the validity of our constraints.

As implied in Chapter 2, due to the large momentum transfer imposed by the CR, CRDM bypasses the limitations of detection mechanisms—even if their masses are low. This allows for the DD experiments to probe much smaller DM masses, even down to the eV scale. It can be shown that for a CR flux energy spectrum which scales as $T^{-\gamma}$ with $\gamma = 3$, the DM mass dependence of CRDM flux is completely canceled out in typical elastic scattering processes [35]. In our case, the CR spectrum scales approximately as $\gamma = 2.7$, implying a very weak DM mass dependence. As a result, constraints can be reliably extrapolated to much smaller DM masses. This is perhaps the greatest strength of the CRDM framework. In the next chapter, we will explore whether a similar cancellation occurs in $2 \rightarrow 3$ inelastic scattering, and find that the situation is more nuanced.

Chapter 4

Cosmic-Ray-Boosted Co-SIMPs

This chapter develops the core idea of this thesis: extending the cosmic ray upscattering framework to co-scattering strongly interacting massive particles (Co-SIMPs). We explore the present-day counterpart of the early-universe freezeout reaction $\chi\chi\psi \rightarrow \chi\psi$ by considering the crossed process $\chi\psi \rightarrow \chi\chi\psi$. This $2 \rightarrow 3$ scattering channel becomes kinematically accessible at the relativistic energies provided by cosmic rays.

Since the original Co-SIMP formulation focuses on non-relativistic thermal freezeout, the $2 \rightarrow 3$ process has only been explored in the context of DM with a Maxwell–Boltzmann distribution, which allows for rewriting $2 \rightarrow 3$ as its crossed counterpart by using detailed balance. Here we investigate how this reaction, driven by cosmic rays interacting with halo DM, generates a relativistic secondary Co-SIMP flux—an analog to the CRDM flux discussed in Chapter 3.

The general features and kinematics of $2 \rightarrow 3$ scattering are first reviewed, followed by a computation of the resulting Co-SIMP CRDM flux and corresponding recoil spectra in direct detection experiments. Initially, attenuation effects in the atmosphere and soil are neglected to isolate the behavior of the unshielded CRDM flux. However, the terrestrial overburden is then shown to severely suppress the relevant Co-SIMP cross sections. This motivates an inspection of the average energy loss for $2 \rightarrow 3$ scatterings, serving as an effective first look into attenuation effects for inelastic interactions.

Upon acquiring grim results, this leads to a second analysis: the consideration of an alternative, loop-induced $\chi\psi \rightarrow \chi\psi$ elastic interaction. This allows us to incorporate full attenuation effects using `DarkSUSY`'s infrastructure, and derive realistic constraints on Co-SIMP parameter space. To the best of our knowledge, this forms the first dedicated CRDM study of Co-SIMPs, and derive new limits on this class of dark matter models.

4.1 $2 \rightarrow 3$ Scattering

Since this chapter involves a $2 \rightarrow 3$ process, we begin by reviewing general features of such scattering, with the CRDM application in mind, and discuss the structure of the total and differential cross sections relevant to this process. Most results are simply stated here; lengthy derivations are given in Appendix A.

Kinematics

To count the number of independent kinematic degrees of freedom (DoF) in an N -particle process, note that each particle contributes 4 components to its 4-momentum, yielding

$4N$ in total. Poincaré invariance eliminates 10 of these,¹ and N on-shell conditions relate one component of each momentum to the other three. Thus, any N -body process has $3N - 10$ independent kinematic invariants.

For $2 \rightarrow 2$ processes, this implies 2 independent DoF. The standard approach introduces the Mandelstam variables $s \equiv (p_1 + p_2)^2$, $u \equiv (p_1 - p_3)^2$, and $t \equiv (p_1 - p_4)^2$, constrained by $s + t + u = \sum_{i=1}^4 m_i^2$. In the $2 \rightarrow 3$ case, there are 5 independent kinematic variables. Rather than using the traditional s , t , and u , we define generalized Mandelstam variables (henceforth simply referred to as Mandelstam variables):

$$s_{ij} \equiv (p_i + p_j)^2, \quad t_{ij} \equiv (p_i - p_j)^2. \quad (4.1)$$

Throughout this section, $2 \rightarrow 3$ processes follow the momentum labeling $p_1 p_2 \rightarrow p_3 p_4 p_5$. For brevity, we adopt the convention $s \equiv s_{12} = E_{\text{CM}}^2$. While s_{ij} is often written as m_{ij}^2 in the literature, this notation is avoided here to reserve the superscript for integration limits.

Using momentum conservation one can show that these satisfy

$$s_{34} + s_{45} + s_{53} = s + m_3^2 + m_4^2 + m_5^2, \quad (4.2)$$

$$t_{13} + t_{14} + t_{15} = m_1^2 - s + \sum_{i=1}^5 m_i^2, \quad (4.3)$$

implying that they are also not all independent. All remaining Mandelstam variables can be written as linear combinations of the 7 appearing above. With the index rules $i, j, k \in \{3, 4, 5\}$ and $i \neq j \neq k$ these relations can be summarized as:

$$\begin{aligned} t_{2i} &= m_1^2 + m_2^2 + m_i^2 - s + s_{jk} - t_{1i}, & t_{ij} &= m_i^2 + m_j^2 - m_k^2 - s + s_{ik} + s_{jk}, \\ t_{12} &= 2(m_1^2 + m_2^2) - s, & s_{1i} &= 2(m_1^2 + m_i^2) - t_{1i}, & s_{2i} &= 2(m_2^2 + m_i^2) - t_{2i}, \end{aligned} \quad (4.4)$$

which exhausts the spectrum.² So, the 7 variables in the two equations (4.2, 4.3), we may pick 5 variables to satisfy the 5 DoF of the system.

Given that particle i is not massless, then in its rest frame (RF), both t_{ij} and s_{ij} are related to the kinetic energy, T_j , of particle j :

$$t_{ij} = (m_i - m_j)^2 - 2m_i T_j, \quad (4.5)$$

$$s_{ij} = (m_i + m_j)^2 + 2m_i T_j. \quad (4.6)$$

For the $2 \rightarrow 3$ process to be kinematically allowed, the minimum kinetic energy of the incoming particle 2 in the RF of particle 1 is

$$T_2^{\min} = \frac{(m_3 + m_4 + m_5)^2 - (m_1 + m_2)^2}{2m_1}. \quad (4.7)$$

The corresponding T_1^{\min} in the RF of particle 2 is a simple $1 \leftrightarrow 2$ relabeling of the above. In the CM frame³ we can also relate the CM energy of particle i to s_{jk} by using momentum conservation:

$$E'_i = \frac{s + m_i^2 - s_{jk}}{2\sqrt{s}}, \quad i, j, k \in \{3, 4, 5\}, \quad i \neq j \neq k. \quad (4.8)$$

¹Three from rotations, three from boosts, and four from translations.

²Additionally we have the trivial relations: $s_{ii} = 4m_i^2$, $t_{ii} = 0 \forall i$.

³We remind the reader that primed quantities refer to the CM frame.

Using $|\mathbf{p}'_i| = \sqrt{E_i'^2 + m_i^2}$ yields that the magnitude of the CM momentum of an outgoing particle is

$$|\mathbf{p}'_i| = \frac{\sqrt{\lambda(s, s_{jk}, m_i^2)}}{2\sqrt{s}}, \quad i, j, k \in \{3, 4, 5\}, \quad i \neq j \neq k, \quad (4.9)$$

where we defined the Källén function:

$$\lambda(a, b, c) \equiv a^2 + b^2 + c^2 - 2ab - 2bc - 2ca. \quad (4.10)$$

For the incoming particles in the CM frame, the energy and momenta are the same as for any $2 \rightarrow n$ process:

$$E'_1 = \frac{s + m_1^2 - m_2^2}{2\sqrt{s}}, \quad E'_2 = \frac{s + m_2^2 - m_1^2}{2\sqrt{s}}, \quad |\mathbf{p}'_1| = |\mathbf{p}'_2| = \frac{\sqrt{\lambda(s, m_1^2, m_2^2)}}{2\sqrt{s}}. \quad (4.11)$$

The $2 \rightarrow 3$ Cross Section

The differential cross section for any $2 \rightarrow n$ process in 4 space-time dimensions is given by [64]⁴

$$d\sigma_{2 \rightarrow n} = \frac{|\mathcal{M}_{2 \rightarrow n}|^2}{4F} d\Pi_n, \quad (4.12)$$

where F is the 2-particle flux factor, $d\Pi_n$ is the n -body Lorentz Invariant Phase Space (LIPS) in (2.7), and $|\mathcal{M}_{2 \rightarrow n}|^2$ is the spin-averaged $2 \rightarrow n$ matrix element squared. For particles with incoming momenta p_1 and p_2 , and outgoing particles with momenta $p_{i \geq 3}$, these quantities can be written as [64]

$$F \equiv \sqrt{(p_1 p_2)^2 - m_1^2 m_2^2} = \frac{1}{2} \sqrt{\lambda(s, m_1^2, m_2^2)}, \quad (4.13)$$

$$d\Pi_n = (2\pi)^4 \delta^4 \left(p_1 + p_2 - \sum_{j=3}^{n+2} p_j \right) \prod_{i=3}^{n+2} \left[\frac{d^3 p_i}{(2\pi)^3 2E_i} \right]. \quad (4.14)$$

The LIPS for any number of particles can be viewed as the possible ways in which their momentum and energy can be distributed, but subject to conservation laws stemming from Poincaré invariance. Since $[\sigma_{2 \rightarrow n}] = -2$ always holds, we note that (4.12–4.14) gives $[\mathcal{M}_{2 \rightarrow n}] = 2 - n$. Thus, for the $2 \rightarrow 3$ process which we will consider, $|\mathcal{M}_{2 \rightarrow 3}|^2$ has mass dimension -2 . Provided there are identical particles in the final state, the LIPS overcounts the number of physically distinguishable configurations. To correct for this, one must divide by the number of identical permutations of the final state. For example, a final state with five particles with one group of three identical particles and one group of two, (4.14) must be multiplied by $1/(2! 3!)$.

Since we will be treating the $2 \rightarrow 3$ interaction as fundamental, the problem becomes more complicated than processes where the phase space can be treated as sequential decays. In the latter case one may split up the phase space into products of ‘smaller’ phase spaces [64, 95], but if treated as a fundamental interaction the situation is more nuanced. Luckily, [96] provides a general recipe for this in any $2 \rightarrow n$ processes.⁵ Following said

⁴Note that we include a factor of $(2\pi)^4$ in $d\Pi_n$, unlike the convention used in [64].

⁵Additionally, [95] performs the same analysis of $2 \rightarrow 3$ processes in more detail with notation which is closer to ours. This reference was found at a later time, but was useful for verifying our results.

procedure, we find that the cross section for any $2 \rightarrow 3$ process in terms of s_{ij} and t_{ij} can be written as⁶

$$\sigma = \frac{1}{4F} \frac{4}{(4\pi)^4} \frac{s}{\lambda(s, m_1^2, m_2^2)} \int \frac{ds_{45} dt_{13} ds_{35} dt_{14}}{|\sin \theta'_{13} \sin \theta'_{34} \sin \varphi'_4|} \frac{|\mathcal{M}|^2}{\sqrt{\lambda(s, s_{45}, m_3^2) \lambda(s, s_{35}, m_4^2)}}, \quad (4.15)$$

up to symmetry factors. Here the angles are CM angles defined by⁷

$$\cos \theta'_{ij} \equiv \frac{\mathbf{p}'_i \cdot \mathbf{p}'_j}{|\mathbf{p}'_i||\mathbf{p}'_j|}, \quad \cos \varphi'_4 \equiv \frac{\cos \theta'_{14} - \cos \theta'_{13} \cos \theta'_{34}}{\sin \theta'_{13} \sin \theta'_{34}}, \quad (4.16)$$

and the limits of integration in (4.15), with our parametrization, are

$$s_{45}^- = (m_4 + m_5)^2, \quad s_{45}^+ = (\sqrt{s} - m_3)^2, \quad (4.17)$$

$$t_{13}^\pm = m_1^2 + m_3^2 - \frac{(s + m_1^2 - m_2^2)(s - s_{45} + m_3^2)}{2s} \pm \frac{\sqrt{\lambda(s, m_1^2, m_2^2) \lambda(s, s_{45}, m_3^2)}}{2s}, \quad (4.18)$$

$$s_{35}^\pm = s + m_4^2 - \frac{(s + s_{45} - m_3^2)(s_{45} + m_4^2 - m_5^2)}{2s_{45}} \pm \frac{\sqrt{\lambda(s, s_{45}, m_3^2) \lambda(s_{45}, m_4^2, m_5^2)}}{2s_{45}}, \quad (4.19)$$

$$\begin{aligned} t_{14}^\pm &= m_1^2 + m_4^2 - \frac{(s + m_1^2 - m_2^2)(s - s_{35} + m_4^2)}{2s} \\ &\quad + \frac{\sqrt{\lambda(s, m_1^2, m_2^2) \lambda(s, s_{35}, m_4^2)}}{2s} [\cos \theta'_{13} \cos \theta'_{34} \pm |\sin \theta'_{13} \sin \theta'_{34}|]. \end{aligned} \quad (4.20)$$

The $+ (-)$ superscript corresponds to the upper (lower) integration limit. By inspection of the variable dependencies in these limits, the current parametrization suggests that we must integrate t_{14} first and s_{45} last, with the s_{35} and t_{13} integrals being interchangeable.⁸

For CRDM, we require the differential cross section with respect to the boosted energy, evaluated in the rest frame of the initial DM particle. As such, it is convenient to choose a parametrization that is simple in the RF of one of the initial-state particles. Eq. (4.5) shows that t_{13} can be related to T_3 in the RF of particle 1. Thus, the easiest way to achieve the above is to switch the s_{45} and t_{13} integrals. This induces the following modifications of the integration limits:

$$t_{13}^\pm = m_1^2 + m_3^2 - \frac{(s + m_1^2 - m_2^2)(s - s_{45}^- + m_3^2)}{2s} \pm \frac{\sqrt{\lambda(s, m_1^2, m_2^2) \lambda(s, s_{45}^-, m_3^2)}}{2s}, \quad (4.21)$$

$$s_{45}^+ = \frac{s + t_{13} - m_1^2 + m_2^2 + m_3^2}{2} + \frac{(s - m_2^2)(t_{13} - m_3^2)}{2m_1^2} + \frac{\sqrt{\lambda(s, m_1^2, m_2^2) \lambda(t_{13}, m_1^2, m_3^2)}}{2m_1^2}, \quad (4.22)$$

with the remaining limits unchanged.

Fig. 4.1 shows a numerical evaluation of (4.15) versus the incoming kinetic energy $T_2 = T_\psi$, with form factors neglected and $|\mathcal{M}_{2 \rightarrow 3}|^2 = 1/s$. For comparison, we also show elastic $\chi p \rightarrow \chi p$ scattering with a constant matrix element normalized to $|\mathcal{M}_{2 \rightarrow 2}|^2 = 3.2 \times 10^{-3}$, chosen to match in the ultra-relativistic limit. At high energies, the cross section approaches the behavior of typical $2 \rightarrow 2$ elastic scattering. However,

⁶See Appendix A.1 for the derivation.

⁷For the angles in terms of invariants, see Appendix A.2.

⁸To see this variable dependence explicitly, we refer to the angles in Appendix A.2.

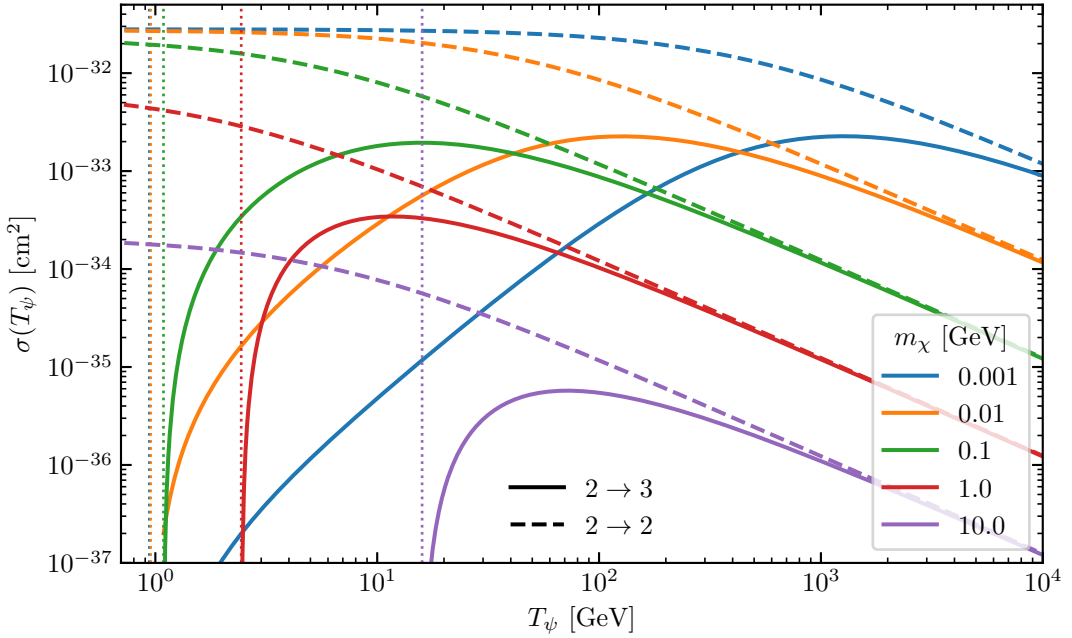


Fig. 4.1: Total cross section $\sigma(T_\psi)$ for a $2 \rightarrow 3$ process (solid) where $m_1 = m_3 = m_4 = m_\chi$, $m_2 = m_5 = m_p$, $|\mathcal{M}_{2 \rightarrow 3}|^2 = 1/s$, and $G(Q^2) = 1$. Additionally, we include an example of a $2 \rightarrow 2$ elastic scattering $\chi p \rightarrow \chi p$ (dashed) where we take $|\mathcal{M}_{2 \rightarrow 2}|^2 = 3.2 \times 10^{-3}$, chosen such that the cross sections align in the ultra-relativistic limit. The dotted vertical lines signify the minimum incoming kinetic energy for the $2 \rightarrow 3$ process to be kinematically allowed from (4.7).

given the small normalization of the $2 \rightarrow 2$ matrix element, the $2 \rightarrow 3$ cross section remains strongly phase-space suppressed. At low energies, the elastic and inelastic cases differ significantly. A clear feature is that the $2 \rightarrow 3$ cross section vanishes at finite $T_\psi > 0$ —as denoted by the vertical lines stemming from (4.7). This is expected, as the production of an additional particle implies a minimum incoming energy. The interplay between the mass scales of m_χ and m_p affects the shape in a distinct way. Surprisingly, when $m_\chi \ll m_p$, the suppression is enhanced at lower energies compared to the scales $m_\chi \sim m_p$. The cross section has a distinct peak at finite T_ψ , well above threshold. The position of this peak depends non-trivially on m_χ : it shifts to lower energies as $m_\chi \rightarrow m_p$ from below, and moves back to higher energies when $m_\chi > m_p$.

In the high energy limit, assuming a matrix element of the form $|\mathcal{M}_{2 \rightarrow 3}|^2 = 1/s$, the $2 \rightarrow 3$ cross section scales as $1/T_\psi \sim 1/s$. In contrast, $2 \rightarrow 2$ elastic scattering with a constant matrix element yields the same scaling. If instead $|\mathcal{M}_{2 \rightarrow 3}|^2 = \text{const.}$, the cross section approaches a constant as $s \rightarrow \infty$, leading to unitarity violation of the S -matrix. This difference originates from the LIPS for a 3-particle final state contributing 2 additional mass dimensions. Since the integrated n -body LIPS has mass dimension $[\Pi_n] = 2n - 4$, then in the massless limit $m_i \rightarrow 0$ where s is the only available scale, dimensional analysis requires $\Pi_n \sim \sqrt{s^{2n-4}} = s^{n-2}$. For $n = 3$, this gives $\Pi_3 \propto s$. We therefore restrict ourselves to matrix elements of the form $|\mathcal{M}|^2 = C/s$, where C is a dimensionless constant, to ensure unitarity is preserved in the high energy limit.

This choice can be further justified by defining the effective matrix element as the

phase-space averaged matrix element:⁹

$$\overline{|\mathcal{M}|^2} \equiv \frac{\int d\Pi_3 |\mathcal{M}_{\text{UV}}|^2}{\int d\Pi_3}, \quad (4.23)$$

where $|\mathcal{M}_{\text{UV}}|^2$ is the matrix element squared arising from the ‘true’ UV completion of the Co-SIMP scenario. Since s is the only quantity which has not been integrated over, and terms like C/m_i^2 are prohibited because they diverge as $m_i \rightarrow 0$, violating unitarity, the matrix element must take the form¹⁰

$$\overline{|\mathcal{M}|^2} = \frac{C}{s + \sum_i a_i m_i^2} \left[1 + b \ln \left(\frac{s}{s_0} \right) \right], \quad (4.24)$$

where a_i and b are dimensionless constants and s_0 is some energy scale. For simplicity, we will set $a_i = b = 0$ and ignore such logarithms, yielding the basic form $|\mathcal{M}|^2 = C/s$, with C defined by (4.23) in the massless limit. From now on, we will treat barred matrix elements as phase-space averaged quantities. This implies that this parametrization will not fully match a UV-complete theory.

Additionally, note that s is evaluated in the matrix element at the mass of the proton, even when χ interacts with a nucleus. This choice better resembles the scenario of a proper UV completion. Using the mass of heavier nuclei would instead allow the constant C to take on much larger values. As will be shown later in this chapter, this amounts to a conservative choice in the context of Co-SIMPs.

Differential Cross Section

For computational purposes, it is convenient to reduce (4.15) to a single-differential form for $d\sigma_{\chi\psi \rightarrow \chi\chi\psi}/dT_\chi$ and $d\sigma_{\chi N \rightarrow \chi\chi N}/dT_N$, which are used to compute the Co-SIMP CRDM flux spectrum and the corresponding recoil rate in the detector. Assuming the matrix element takes the form $\overline{|\mathcal{M}|^2} = C/s$ and neglecting form factors, (4.15) simplifies significantly. The details are spelled out in Appendix A.3. We isolate the particle labeled 3, for reasons which will become apparent in the following sections. The resulting differential cross section in the CM frame is

$$\frac{d\sigma}{dE'_3} = \frac{1}{4F} \frac{1}{(4\pi)^3} \frac{\overline{|\mathcal{M}|^2}}{s_{45}\sqrt{s}} \sqrt{\lambda(s, s_{45}, m_3^2)\lambda(s_{45}, m_4^2, m_5^2)}, \quad (4.25)$$

and in the rest frame of particle 1 it is

$$\frac{d\sigma}{dE_3} = \frac{1}{4F} \frac{m_1}{(4\pi)^3} \frac{1}{\sqrt{\lambda(s, m_1^2, m_2^2)}} \int_{s_{45}^-}^{s_{45}^+} \frac{ds_{45}}{s_{45}} \sqrt{\lambda(s_{45}, m_4^2, m_5^2)} \overline{|\mathcal{M}|^2}. \quad (4.26)$$

In the latter expression, the upper and lower integration limits are given by (4.22) and (4.17), respectively. These expressions remain valid when $|\mathcal{M}|^2$ depends on s_{45} , and in the latter case also on t_{13} . The same of course applies to the inclusion of form factors at this level.

An example of (4.25) and (4.26) is shown in Fig. 4.2, represented by the solid and dashed lines, respectively. As a consistency check, both differential cross sections were numerically integrated and found to yield the same result. Since we assume a matrix element independent of the scattering angles, the resulting distributions differ significantly

⁹This is essentially a generalization of an angular averaged matrix element in $2 \rightarrow 2$ elastic scattering.

¹⁰In principle, the matrix element could of course also contain other non-analytic factors.

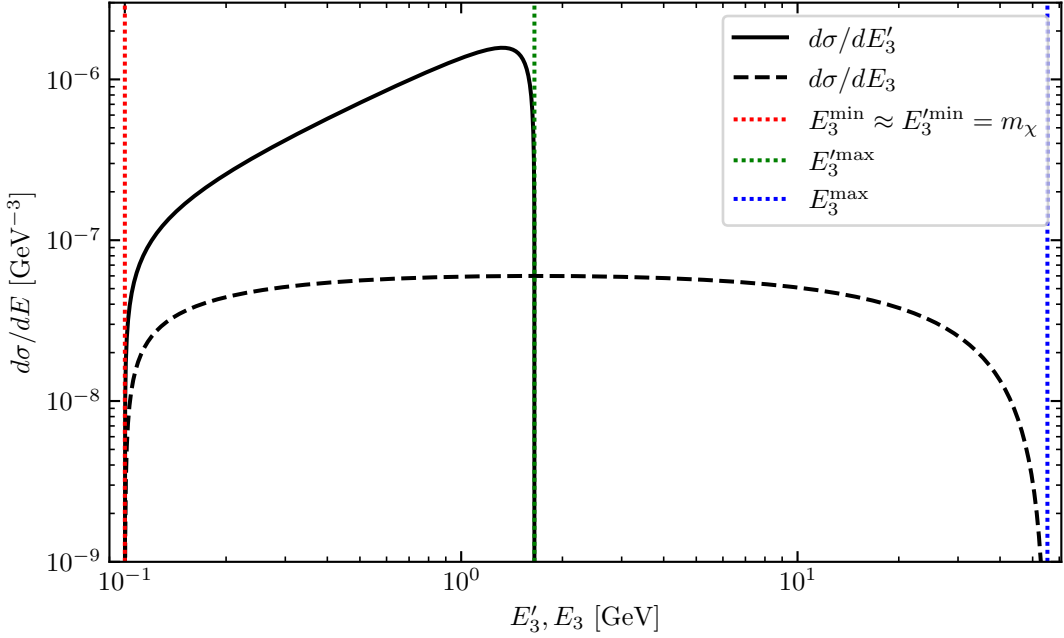


Fig. 4.2: The differential cross section in the CM frame, $d\sigma/dE'_3$, (solid) and lab frame, $d\sigma/dE_3$, (dashed) with $m_1 = m_3 = m_4 = m_\chi = 0.1 \text{ GeV}$, $m_2 = m_5 = m_p$, $s = 10(m_3 + m_4 + m_5)^2$, and $|\mathcal{M}|^2 = 1/s$. The vertical dotted lines indicate the analytically determined limits on E_3 and E'_3 from (4.21) and (4.17), respectively.

from those in the elastic $2 \rightarrow 2$ case. There, a similar setup leads to a delta-function-like energy distribution in the CM frame—required by 4-momentum conservation—and a flat distribution in the lab frame. In contrast, the $2 \rightarrow 3$ kinematics produce continuous and nontrivial energy spectra in both frames. The lab frame is perhaps the most similar, showing a much broader energy range. The primary difference from $2 \rightarrow 2$ is the sharp falloff near both ends of the energy spectrum. Of course, the maximal energy in $2 \rightarrow 3$ is lower due to the kinematic cost of producing an additional particle. Compared to the lab frame, the CM frame is skewed heavily towards the higher end of its energy spectrum. This distortion arises from the Lorentz boost against the direction of the incoming $\psi(p_2)$, taking us from the lab to the CM frame. Thus, the CM frame heavily favors higher energies given our mass configuration. Interestingly, in $2 \rightarrow 3$, both frames allow one of the outgoing particles to be produced at rest, as seen from both energy minima being m_χ , though this region is heavily suppressed. In $2 \rightarrow 2$ elastic scattering, while this naturally occurs in the lab frame, such configurations are kinematically forbidden in the CM frame.

4.2 Co-SIMP CRDM Flux

To compute the flux of cosmic-ray upscattered Co-SIMPs at Earth, we apply the general flux expression from the Chapter 3 to the Co-SIMP scenario shown in Fig. 4.3. We take the initial-state DM particle $\chi(p_1)$ to be at rest within the galactic halo, defining this frame as the cosmic frame (CF), and take $\psi(p_2)$ to be the incoming CR scattering particle. Using (3.10), relabeling $X \rightarrow \chi\chi\psi$, and insert a factor of 2—since two CRDM

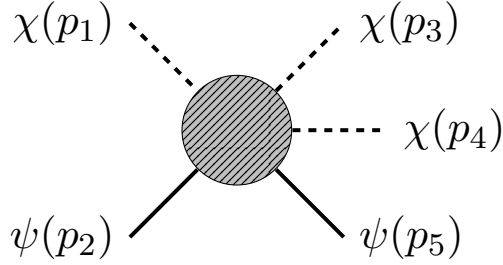


Fig. 4.3: Momentum labeling for the Co-SIMP interaction in the galactic halo. The incoming CR particle $\psi(p_2)$ interacts with an at rest DM particle $\chi(p_1)$ which then produces an out state $\chi(p_3)\chi(p_4)\psi(p_5)$.

particles are produced per interaction—gives

$$\frac{d\Phi_\chi}{dT_\chi} = 2 \times D_{\text{eff}} \frac{\rho_\chi^{\text{loc}}}{m_\chi} \sum_\psi \int_{T_\psi^-}^\infty dT_\psi \frac{d\Phi_\psi^{\text{loc}}}{dT_\psi} \frac{d\sigma_{\chi\psi \rightarrow \chi\chi\psi}}{dT_\chi}. \quad (4.27)$$

To evaluate this, we isolate the contribution from a single outgoing CRDM particle—specifically particle 3, as anticipated in the previous section. Relabeling (4.26) as implied by Fig. 4.3, the differential cross section in the CF becomes

$$\frac{d\sigma_{\chi\psi \rightarrow \chi\chi\psi}}{dT_\chi} = \frac{1}{2} \frac{1}{4F} \frac{m_\chi}{(4\pi)^3} \frac{1}{\sqrt{\lambda(s, m_\chi^2, m_\psi^2)}} \int_{s_{45}^-}^{s_{45}^+} \frac{ds_{45}}{s_{45}} \sqrt{\lambda(s_{45}, m_\chi^2, m_\psi^2)} |\mathcal{M}|^2, \quad (4.28)$$

where the leading factor of $1/2$ accounts for the two identical particles in the final state.¹¹ Although χ is a complex particle, the \mathbb{Z}_3 symmetry restricts the process to either $\chi\psi \rightarrow \bar{\chi}\bar{\chi}\psi$ or $\bar{\chi}\psi \rightarrow \chi\chi\psi$ (see the discussion in Section 2.5), meaning that the two final-state χ particles are identical.

We reiterate a potential limitation in the direct use of (3.10): the diffusion distance D_{eff} has only been rigorously studied in the context of elastic $2 \rightarrow 2$ CRDM scattering [36]. For $2 \rightarrow 3$ processes, one should in principle expect a more complicated dependence on the kinematics of both final-state particles. To remain conservative, we adopt $D_{\text{eff}} = 5 \text{ kpc}$, somewhat lower than typical values in the CRDM literature. A dedicated analysis of D_{eff} in this inelastic setting is left for future work. However, its effect on our results is minimal. The lower exclusion limit scales strictly as $1/\sqrt{D_{\text{eff}}}$, and thus any change in D_{eff} results in a simple vertical shift of the bound. In contrast, the upper exclusion limit—set by attenuation—depends only logarithmically on D_{eff} . As we will see, the part of the parameter space affected by changes to D_{eff} lies entirely within a region already excluded by independent constraints. An extreme and unrealistic choice like $D_{\text{eff}} = 50 \text{ pc}$ would therefore yield the same physical conclusions.

Minimal Cosmic-Ray Energy

The only missing part in (4.27) is an expression for $T_\psi^-(T_\chi)$. This quantity is the answer to the question: given that we measure T_χ , and it is known that the $2 \rightarrow 3$ interaction in

¹¹We will always keep such symmetry factors separate from the rest to make it easier for the reader (and the author!) to be reminded that it has been included, and to more easily adapt these expressions to related processes with different final-state symmetries. This thought process is also applied to the flux factor $4F$.

Fig. 4.3 occurred, what is the minimal energy that the incoming particle ψ could have had? Conceptually, the most direct way to solve this is by considering when T_χ achieves its maximum value. In principle, one could then solve (4.21) for s and use its one-to-one correspondence with T_ψ , as well as that of t_{13} and T_χ . However, this requires solving a quartic polynomial, which is analytically inconvenient.

To avoid this, we instead consider the maximum possible energy of particle 3 in the CM frame. Eq. (4.8) implies that $E_3'^{\max}$ corresponds to the minimum of s_{45} . According to (4.6), in the RF of particle 5, s_{45} is minimized when $T_4 = 0$, i.e. when p_4 and p_5 are at rest relative to one another. Since s_{45} is Lorentz invariant, this holds in all frames. Assuming this corresponds to the maximal energy E_3 in the CF, then in this scenario the following holds:

$$(m_4 + m_5)^2 = (E_4 + E_5)^2 - (|\mathbf{p}_4| + |\mathbf{p}_5|)^2 = (E_2 + m_1 - E_3)^2 - (|\mathbf{p}_2| - |\mathbf{p}_3|)^2. \quad (4.29)$$

Here, we have used the requirement that $\mathbf{p}_4 \parallel \mathbf{p}_5$ due to them sharing their RF, along with energy-momentum conservation. With the relevant replacements, solving (4.29) for T_2 yields two solutions of the form $T_2^{\min} \equiv T_\psi^- = a(1 \pm \sqrt{b/a^2}) = a \pm \text{sgn}(a)\sqrt{b}$. Clearly, when a is negative, the $+$ solution above would give a negative kinetic energy which is of course unphysical. Hence, we must associate a negative a with the negative sign. Requiring continuity, a simple check of the full solution shows that positive a must be associated with the positive sign. Thus, the physical branch may be combined into a single solution: $T_\psi^- = a + \sqrt{b}$. Written out fully, the result is:

$$T_\psi^- = \frac{2T_\chi - 2m_\psi + m_\chi}{4} + \sqrt{\frac{(2m_\chi + T_\chi)(m_\chi + 2T_\chi)((m_\chi + 2m_\psi)^2 + 2m_\chi T_\chi)}{16m_\chi T_\chi}}. \quad (4.30)$$

It has been verified numerically that the above is equivalent with inverting both solutions in (4.21) for the relevant mass configuration.

Fig. 4.4 shows the minimal kinetic energy an incoming proton must have had to provide the recoil energy of one of the DM particles for various m_χ . We compare it to the corresponding result for elastic scattering in (3.4). As one would expect, the energy required is always higher than in elastic scattering. However, we see a peculiar behavior as $T_\chi \rightarrow 0$, following a power law $T_\psi^- \sim T_\chi^{-1/2}$ and thus diverging in this limit. This would imply the counterintuitive result that achieving a very low energy T_χ requires a very large incoming T_ψ . At first sight, this appears incorrect, but the underlying reason is relatively simple. Since this has important implications for our results, we aim to justify it below.

The minimum T_ψ^- allowed for any given T_χ can be found analytically by solving the equation $dT_\psi^-/dT_\chi = 0$. This yields

$$T_\chi^{\text{sol}} = \frac{m_\chi(m_\chi + 2m_\psi)}{2(2m_\chi + m_\psi)}. \quad (4.31)$$

Inserting the above back into (4.30) gives that $T_\psi^-(T_\chi^{\text{sol}}) = 3m_\chi/2 + m_\psi$. Using (4.7), one sees that this corresponds to $s = (2m_\chi + m_\psi)^2$ at the pivot point. This s corresponds to the minimum CM energy in the final state system for these 3 particles, and thus corresponds to all the particles in the CM frame being at rest. Since the boost to the CF is along the direction of \mathbf{p}_2 , this means that any $T_\chi < T_\chi^{\text{sol}}$ requires $\cos\theta'_{23} < 0$, i.e. that particle 3 travels against the direction of the incoming CR particle in the CM frame. Thus, the boost taking us back to the CF frame will lower the energy of the χ in question.

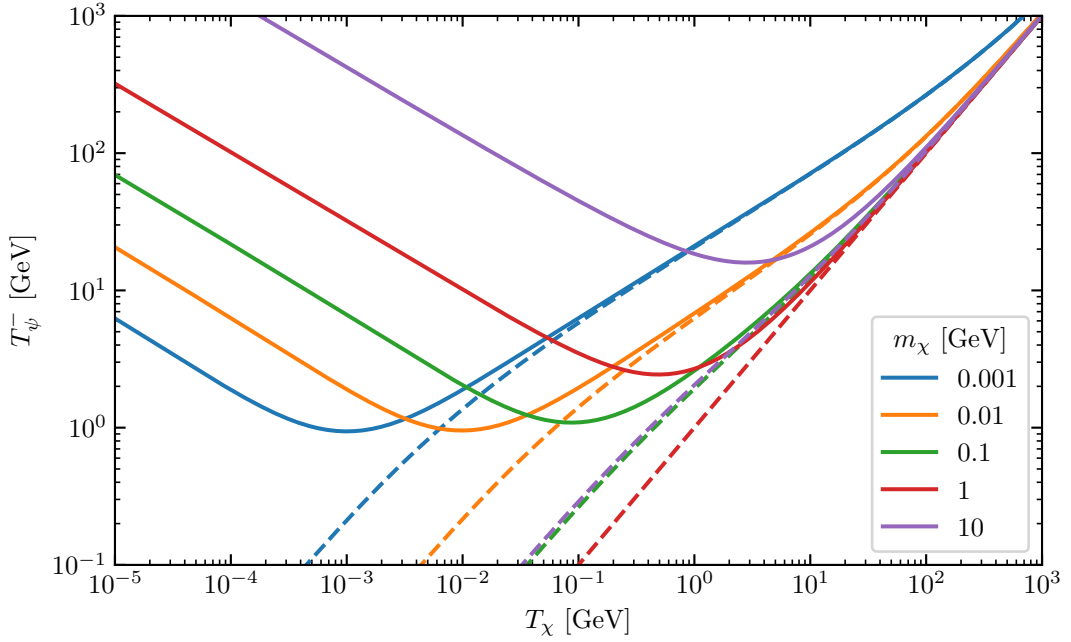


Fig. 4.4: T_ψ^- as a function of T_χ with $m_\psi = m_p$ for various DM masses. The solid lines correspond to $2 \rightarrow 3$ inelastic scattering for the process in Fig. 4.3 while the dashed lines correspond to elastic $\chi\psi \rightarrow \chi\psi$ scattering. The regions above each given line correspond to the kinematically allowed regions of incoming energy for any given DM energy. In the $T_\chi \rightarrow \infty$ limit all follow the power law $T_\psi^- \propto T_\chi$. Additionally, the $2 \rightarrow 3$ process follows the power law $T_\psi^- \propto T_\chi^{-1/2}$ in the $T_\chi \rightarrow 0$ limit and contains a minima at (4.31) corresponding to $T_\psi^- = 3m_\chi/2 + m_\psi$.

Now, if this was the sole reason for the non-monotonic behavior of T_ψ^- , one would also expect to see the same behavior in $2 \rightarrow 2$ elastic scattering. However, this would not be the minimum energy in $2 \rightarrow 2$, and we cannot know whether this is what occurred or if T_ψ simply had a low kinetic energy and thus transferred a low amount energy to the outgoing CRDM. This is the subtle difference: in $2 \rightarrow 3$ we cannot have an arbitrarily low T_ψ to provide a low energy transfer since it is required to have sufficient energy to produce another particle. The only possible way to produce a low energy χ in the CF is when $\cos\theta'_{23} < 0$. Thus, we will be ‘fighting’ against the boost that takes us from the CM frame to the CF, which is the reason for this non-monotonically increasing T_ψ^- . Knowing this, it is now no longer hard to justify the divergence in the $T_\chi \rightarrow 0$ limit. For this to happen, then in the CM frame we require that one of the outgoing χ must have the exact same momenta as the incoming $\chi(p_1)$. This is only approximately possible if the production of another χ is so negligible that the loss of kinetic energy in the system is minute. Since in the CF frame—in this limit—essentially all the energy is carried by $\psi(p_2)$, this clearly corresponds to an ultra-relativistic regime and hence, $T_\psi^- \rightarrow \infty$.

Since the high-energy CR flux spectrum is subject to the $d\Phi_\psi/dT_\psi \propto T_\psi^{-2.7}$ power law for large T_ψ , this feature leads to a highly suppressed low-energy DM flux compared to the analogous $2 \rightarrow 2$ case. Additionally, in the limit that $m_\chi \ll m_\psi$, (4.31) scales as m_χ . The pivot point is thus skewed to 0 as we take $m_\chi \rightarrow 0$, eventually coinciding with elastic scattering. The remaining behaviors in Fig. 4.4 mimic those of $2 \rightarrow 2$ so we will not probe them in any further detail.

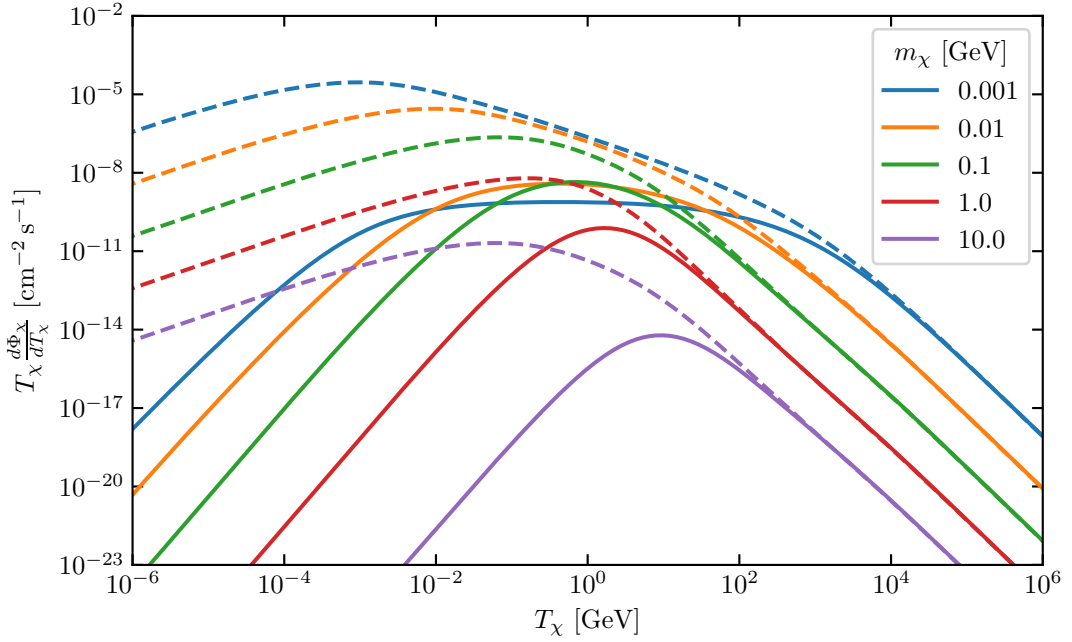


Fig. 4.5: CRDM flux $T_\chi \times d\Phi_\chi/dT_\chi$ of $\chi\psi \rightarrow \chi\chi\psi$ process compared to the previously considered $\chi\psi \rightarrow \chi\psi$ process from [4, 7]. Only the proton ICR flux is considered along with setting $Q^2 = 0$ in both cases. Here $|\mathcal{M}_{2 \rightarrow 2}|^2 = 1$ and the constant in $|\mathcal{M}_{2 \rightarrow 3}|^2 = C/s$ is chosen such that the ultra-relativistic limit coincides. Additionally, we have set $m_\chi = 0$ in the relativistic correction to the $2 \rightarrow 2$ cross section (cf. (B.3)) such that it more accurately resembles our $2 \rightarrow 3$ counterpart. This is because we cannot introduce a factor of m_χ^2 in the $2 \rightarrow 3$ cross section without also introducing a $1/s^2$ scaling.

Resulting Flux

With this, we have everything required to compute the interstellar Co-SIMP CRDM flux spectrum incident at Earth, as shown in Fig. 4.5. This figure includes only the proton ICR flux, and is compared it to the analogous $2 \rightarrow 2$ scattering scenario from [7]. As was seen in Fig. 4.1, the ultra-relativistic regime in the $2 \rightarrow 3$ cross section was unaffected. Thus, as expected, there is a negligible difference between the fluxes at high energies, since the kinematic cost of producing an additional DM particle becomes negligible. On the other hand, the low energy regime is significantly changed. This arises from the combined effects of the non-monotonic behavior of T_ψ^- , which forces low T_χ production to sample the high-energy tail of the ICR spectrum, and the altered spectrum of the differential cross section, resulting in a sharp suppression. A numerical inspection of the power laws of $d\sigma_{\chi\psi \rightarrow \chi\chi\psi}/dT_\chi$ in the low T_χ and high T_ψ regimes, along with $d\Phi_\psi/dT_\psi \sim T_\psi^{-2.7}$ for large T_ψ , gives the scaling

$$T_\chi \frac{d\Phi_\chi}{dT_\chi} \sim T_\chi \int_{T_\psi^-}^\infty dT_\psi \frac{d\sigma_{\chi\psi \rightarrow \chi\chi\psi}}{dT_\chi} \times \frac{d\Phi_\psi}{dT_\psi} \sim T_\chi \int_{T_\chi^{-1/2}}^\infty dT_\psi \frac{\sqrt{T_\chi}}{T_\psi^2} \times T_\psi^{-2.7} \sim T_\chi^{3.35}. \quad (4.32)$$

This is precisely the power law common to all $2 \rightarrow 3$ CRDM fluxes in Fig. 4.5 for $T_\chi \ll m_\chi, m_\psi$. Since the differential cross section in the CF frame becomes approximately flat in the high energy regime—seen by horizontally stretching the lab frame result in Fig. 4.2—the analogous behavior to $2 \rightarrow 2$ is expected given our choice of matrix elements. The transition between these two regimes is non-trivial, and we did not find a successful

analysis which explains this behavior. However, several features mimic a suppressed case of the $2 \rightarrow 2$ flux. Thus, its behavior is unsurprising given the low energy behavior.

Including Form Factors

For a realistic treatment, we now wish to incorporate form factors into the analysis. With the parametrization in Fig. 4.3 then, given that ψ is a composite particle, the relevant time-like momentum transfer is

$$\begin{aligned} Q^2 &= -t_{25} = s - m_1^2 - m_2^2 - m_5^2 - s_{34} + t_{15} \\ &= m_1^2 - m_5^2 - s + s_{35} + s_{45} - t_{13} - t_{14}, \end{aligned} \quad (4.33)$$

where we used various relations in (4.4). Due to Q^2 depending on every Mandelstam variable in (4.15), and since these are all independent, form factors must be included before any of the integrals have been performed. As such, the simplified differential cross section in (4.26) is not valid when including form factors.

The fact that Q^2 depends on all kinematic variables can be explained with simple physical intuition. In the CF we can never precisely know the momentum transfer which occurred between the CR and the DM particle since all that is (indirectly) measured is the CRDM flux of a single DM particle in the final state. The momentum transfer experienced by the CR could only be uniquely determined if the initial energy were known and either the energies and momenta of both outgoing CRDM particles or the four-momentum of the outgoing CR particle were measured. Since the only information in the interaction we make use of is the energy of one DM particle, we must average over all the possible Q^2 configurations for the process. This is precisely what (4.33) suggests.

Due to the non-trivial Q^2 dependence in (4.33) in the CF, even with an explicit form such as the dipole form factor, performing the integrals analytically is no longer feasible. Thus, when including form factors into the analysis, the differential cross section to be used in (4.27) is

$$\begin{aligned} \frac{d\sigma_{X\psi \rightarrow \chi\chi\psi}}{dT_\chi} &= \frac{1}{2} \frac{1}{4F} \frac{8m_\chi}{(4\pi)^4} \frac{s}{\lambda(s, m_\chi^2, m_\psi^2)} \int_{s_{45}^-}^{s_{45}^+} \frac{ds_{45}}{|\sin \theta'_{13}|} \left[\sqrt{\lambda(s, s_{45}, m_3^2)} \right]^{-1} \\ &\times \int_{s_{35}^-}^{s_{35}^+} \frac{ds_{35}}{|\sin \theta'_{34}|} \left[\sqrt{\lambda(s, s_{35}, m_4^2)} \right]^{-1} \int_{t_{14}^-}^{t_{14}^+} dt_{14} \frac{|\mathcal{M}_0|^2}{|\sin \varphi'_4|} A_\psi^2 G_\psi^2(Q^2), \end{aligned} \quad (4.34)$$

where G_ψ denotes the form factor for the CR particle and we included the A_ψ^2 coherent enhancement factor. Note that the above requires the explicit form of the CM angles given in Appendix A.2.

The first line of (4.33) suggests that this would be much simpler if we had used t_{25} as one of our integration variables in (4.15), and chosen a parametrization in which it appears last in the integration sequence in (4.34). However, with this choice it would be a much more difficult task to isolate one of the χ particles for the differential cross section. As such, it was not attempted to re-parameterize the cross section, but do not exclude the possibility that a particular combination of s_{ij} and t_{ij} variables could significantly improve the computational efficiency.

Fig. 4.6 shows the numerical result for the CRDM flux when including the dipole form factor for the proton in (3.10), along with a comparison to the previous $G(Q^2) = 1$ case. We also include the half-analytical result where form factors were neglected to verify the numerical result. Unlike in $2 \rightarrow 2$ scattering, the low-energy spectrum here is affected by form factors, in agreement with the physical interpretation mentioned earlier. This is

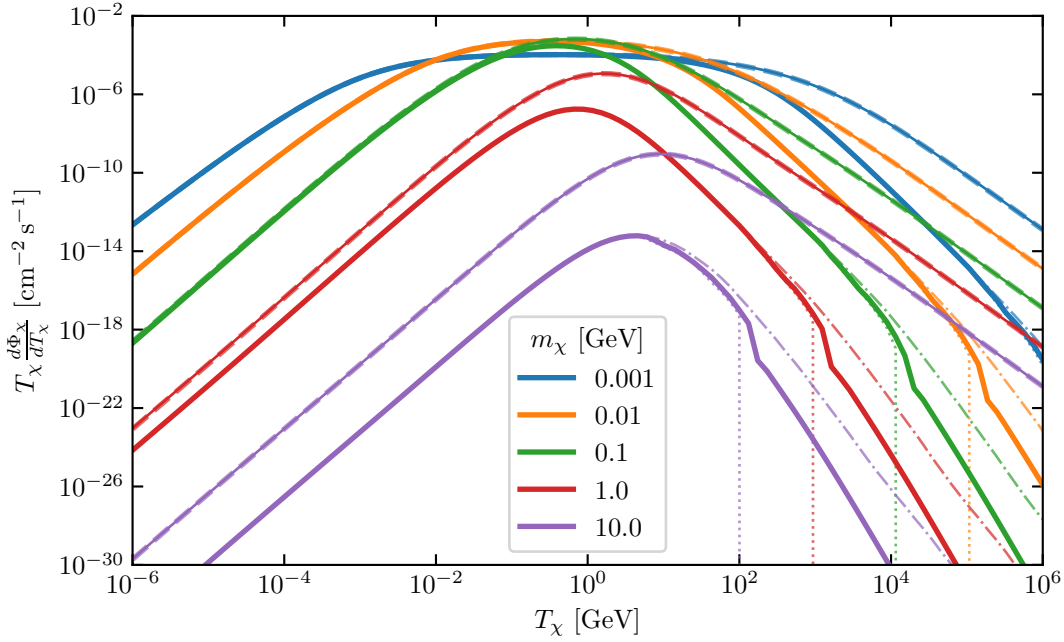


Fig. 4.6: CRDM flux $T_\chi d\Phi_\chi/dT_\chi$ with $|\mathcal{M}|^2 = C/s$ due to proton ICR flux of the $2 \rightarrow 3$ process with (thick solid) and without form factors (dashed) both done completely numerically. To confirm the numerical result, we also include the half analytical result from Fig. 4.5 (thin solid). The dash-dotted lines correspond to a higher accuracy integration routine, whilst the dotted lines exclude all contributions with momentum transfers $Q^2 > 10 \text{ GeV}^2$.

of course only kinematically likely if $m_\chi/m_p \gtrsim 0.1$, as the momentum transfers from a light to a heavy particle are generally small. This region of the flux is anyhow irrelevant for $2 \rightarrow 3$ Co-SIMP DD, since the process requires relativistic CRDM to reoccur in the detector.

At very large T_χ , the program suffers from numerical errors. To remedy this, the flux was also computed using higher-accuracy integration routines (shown as dash-dotted lines), which remove these artifacts. However, for the masses relevant to our analysis, this high-energy range is strongly suppressed by form factors and contributes negligibly to the recoil rate in the detector. Dotted lines show the CRDM flux when setting $G(Q^2) = 0$ for $Q^2 > 10 \text{ GeV}^2$, illustrating that the high- T_χ flux vanishes entirely once the unphysical region is excluded. This confirms that when such numerical artifacts appear, they coincide with momentum transfers that exceed the physical validity of the form factor model. We choose to retain these numerical features in our default results, not only for practical reasons, but also because they act as a diagnostic tool. Their appearance signals when contributions begin to arise from kinematic regions where our model assumptions break down, such as deep inelastic scattering or quark-level resolution of the CR species. In this sense, such artifacts serve as a useful check on whether the results are being extrapolated beyond their intended physical regime.

Impact of CR species

Finally, the impact of each individual CR species is shown in Fig. 4.7. Here, the black solid, dashed, dash-dotted and dotted lines correspond to scattering on p , ${}^4\text{He}$, ${}^{12}\text{C}$ and ${}^{16}\text{O}$, respectively. Clearly, the proton is by far the most dominant CR, with the heavier

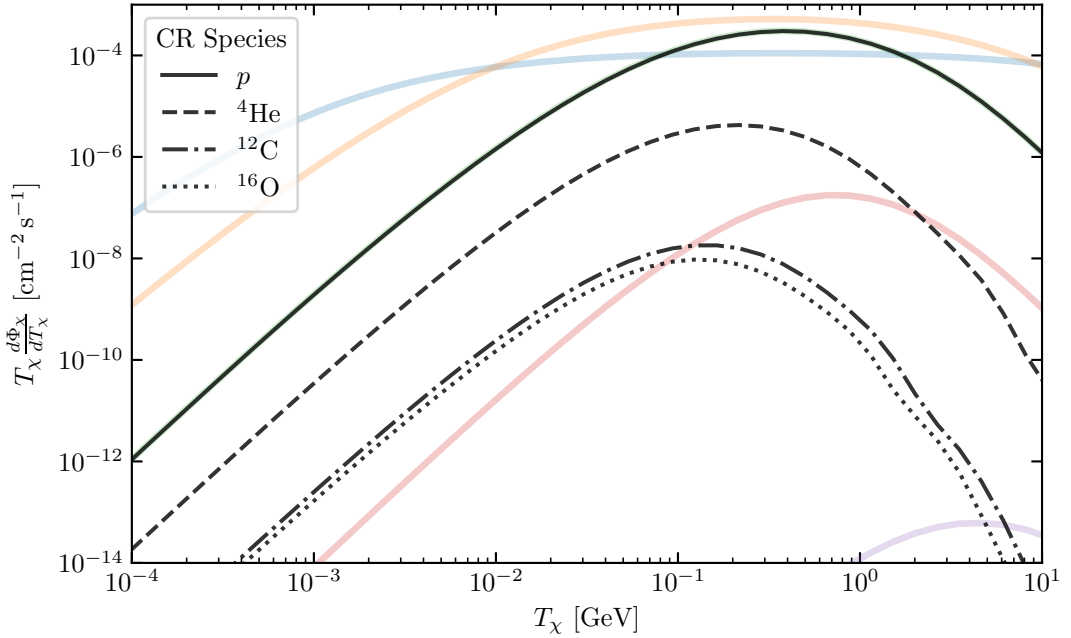


Fig. 4.7: The individual contributions to the CRDM flux $T_\chi d\Phi_\chi/dT_\chi$ with $|\mathcal{M}|^2 = C/s$ and $m_\chi = 0.1 \text{ GeV}$. The solid, dashed, dash-dotted and dotted lines correspond to scattering on p , ${}^4\text{He}$, ${}^{12}\text{C}$ and ${}^{16}\text{O}$, respectively. The features seen at high T_χ for the heavier CR species stem from numerical errors, not any underlying physics.

species giving $\mathcal{O}(1\%)$ corrections. While it is not included in the figure, this holds for all the m_χ we have considered. This is a consequence of the minimum energy requirement $T_\psi^{\min} = 3m_\chi/2 + m_\psi > m_\psi$, regardless of m_χ . Looking back to Fig. 3.1, we see that $T_\psi \gtrsim 5 \text{ GeV}$ already samples past the peak of the ICR flux spectrum for these heavier CR species. For the proton this is not quite the case due to its lower mass, and increased flux at $T_p \sim 1 \text{ GeV}$. Due to this, one can safely neglect all heavier CR species for nucleophilic Co-SIMPs.

Computing the Co-SIMP CRDM flux with form factors is time-consuming, especially since the result is used repeatedly in later calculations. To improve efficiency, the flux was precomputed on a grid using the faster, less accurate integration routine. The absence of numerical artifacts in the subsequent results confirms that this approximation has negligible impact. The grid spans 100 log-spaced values of $m_\chi \in [10^{-4}, 10] \text{ GeV}$ and 100 log-spaced values of $T_\chi \in [10^{-4}, 10^6] \text{ GeV}$. A 2D log-linear interpolation estimates intermediate values. To handle values outside the tabulated range in T_χ , asymptotic power laws are computed for $T_\chi < 10^{-4} \text{ GeV}$ and $T_\chi > 10^6 \text{ GeV}$, where the behavior is well understood. The same is not done in m_χ , as the flux does not exhibit a clear power-law scaling in that direction. In such cases, the program computes the flux on the fly.¹² Since the flux scales linearly with the matrix element normalization C , any rescaled result for C' follows by multiplying the stored $d\Phi_\chi/dT_\chi$ by C'/C .

¹²This has never been necessary, as the parameter space of nucleophilic Co-SIMPs considered here remains within this mass range.

4.3 Recoil Rates in a Detector

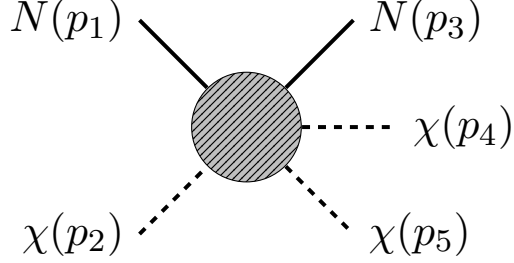


Fig. 4.8: Momentum labeling in the detector.

With the Co-SIMP CRDM flux computed, we will now turn to recoil rates in a detector. For the moment, we will neglect attenuation in the overburden and work with the unshielded flux. This will allow us to use conventional DD constraints from Section 3.5 to provide the lower limits on the Co-SIMP cross section.

Before proceeding, we clarify our terminology regarding exclusion limits. In the presence of competing constraints—such as attenuation and detector sensitivity—the terminology of “upper” and “lower” bounds can become confusing as they imply that all parameter values above and below such regions are excluded, respectively. However, in this thesis, our bounds tend to only apply to a finite region. Thus, throughout this work, we refer to *lower limits* and *upper limits* as shorthand for *lower* and *upper exclusion limits*, respectively. For example, a lower and upper limit on a cross section indicates that only the region between the limits is excluded. When there are no competing constraints, the lower and upper limits are the upper and lower bounds, respectively.

With this clarified, we now return to the calculation of recoil rates. Assuming a detector which measures the recoil of a nucleus, N , induced by the Co-SIMP process, we can calculate the nuclear recoil spectra stemming from an incoming CRDM causing an interaction as depicted in Fig. 4.8. Since the CRDM component which may contribute to the $2 \rightarrow 3$ process must be relativistic, we can neglect any boost between the CF and the lab frame. This is because the halo velocities are comparatively small, implying that such a boost induces a negligible change in the DM energy.¹³ Thus, the differential interaction rate *per target nucleon* follows directly from relabeling (3.33), giving

$$\frac{d\Gamma_{\chi N \rightarrow \chi \chi N}}{dT_N} = \int_{T_\chi^-}^\infty dT_\chi \frac{d\sigma_{\chi N \rightarrow \chi \chi N}}{dT_N} \frac{d\Phi_\chi}{dT_\chi}. \quad (4.35)$$

Once again we require a corresponding expression for $d\sigma_{\chi N \rightarrow \chi \chi N}/dT_N$ and T_χ^- . With most of the required setup already established, this step is straightforward. The relevant differential cross section is obtained by relabeling (4.26) according to Fig. 4.8, where the incoming CRDM particle is $\chi(p_2)$, and the detected nucleus is $N(p_3)$.¹⁴ This implies the mass assignments $m_1 = m_3 = m_N$ and $m_2 = m_4 = m_5 = m_\chi$, which leads to

$$\frac{d\sigma_{\chi N \rightarrow \chi \chi N}}{dT_N} = \frac{1}{2} \frac{1}{4F} \frac{m_N}{(4\pi)^3} \frac{1}{\sqrt{\lambda(s, m_N^2, m_\chi^2)}} \int_{s_{45}^-}^{s_{45}^+} \frac{ds_{45}}{s_{45}} \sqrt{\lambda(s_{45}, m_\chi^2, m_\chi^2)} |\mathcal{M}|^2, \quad (4.36)$$

¹³While this argument is particularly relevant for the $2 \rightarrow 3$ process, it also holds for elastic $2 \rightarrow 2$ processes provided that $m_\chi \lesssim 10$ GeV.

¹⁴This is the primary reason that we isolated particle number 3 in Section 4.1.

where, once again, the leading factor of $1/2$ is the symmetry factor, and it is understood that the relabeling of s_{45} 's definition (and its limits) has been done in accordance to Fig. 4.8. Given that $|\mathcal{M}|^2$ is independent of s_{45} , the above integral has a relatively simple analytical result since $m_4 = m_5 = m_\chi$, yielding

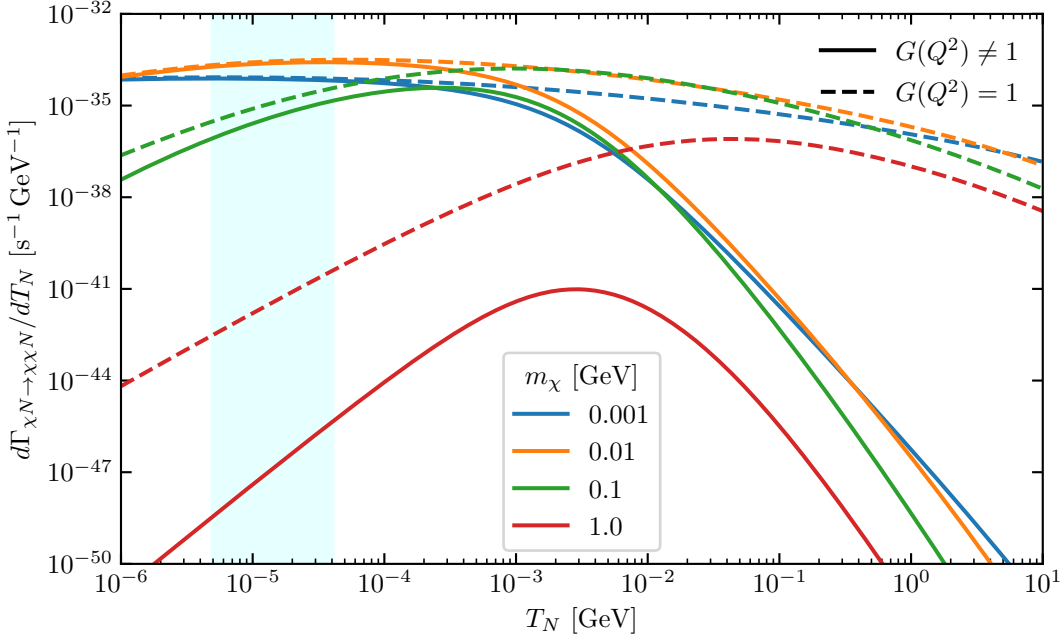
$$\frac{d\sigma_{\chi N \rightarrow \chi \chi N}}{dT_N} = \frac{1}{2} \frac{1}{4F} \frac{m_N}{(4\pi)^3} \frac{|\mathcal{M}|^2}{\sqrt{\lambda(s, m_N^2, m_\chi^2)}} \\ \times \left[\sqrt{s_{45}^+(s_{45}^+ - 4m_\chi^2)} - 4m_\chi^2 \operatorname{arctanh} \left(\sqrt{1 - \frac{4m_\chi^2}{s_{45}^+}} \right) \right]. \quad (4.37)$$

To arrive at T_χ^- , we follow the same procedure as preceding (4.30), giving

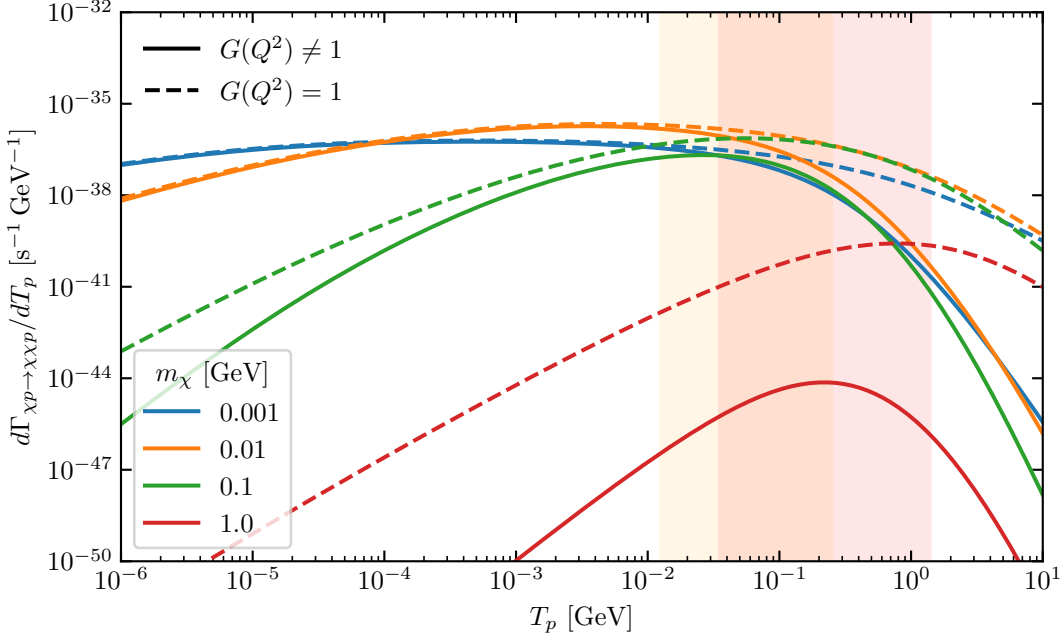
$$T_\chi^- = \frac{T_N}{2} - m_\chi + \frac{3m_\chi^2}{4m_N} + \frac{1}{4} \sqrt{\left(\frac{2m_N}{T_N} + 1 \right) \left(\frac{2T_N}{m_N} + \frac{9m_\chi^2}{m_N^2} \right) \left(2m_N T_N + m_\chi^2 \right)}. \quad (4.38)$$

As before, T_χ^- has a $T_N^{-1/2}$ divergence in the $T_N \rightarrow 0$ limit. Including form factors in this case is simple since $Q^2 = -t_{13} = 2m_N T_N$, which is exactly the same as $2 \rightarrow 2$ elastic scattering. Thus, unlike previously, this does not heavily affect our computation times.

As an example, Fig. 4.9 shows the differential recoil rate expected from Co-SIMP CRDM scattering off xenon nuclei (top) and free protons (bottom), respectively. The matrix element is taken as $|\mathcal{M}|^2 = C/s$ with $C = 10^{-24} \text{ GeV}^2 \text{ cm}^2$, which corresponds to a cross section $\sigma_{\chi p \rightarrow \chi \chi p} \sim 10^{-30} \text{ cm}^2$, of course, depending on the mass m_χ and energy scale as seen in Fig. 4.1. We also note that this figure excludes attenuation. The solid curves include the effect of form factors $G(Q^2)$ in both the CF and detector, while the dashed curves assume $G(Q^2) = 1$. Both plots sum over cosmic ray species $\psi \in \{\text{p}, \text{H}, \text{C}, \text{O}\}$ contributing to the Co-SIMP CRDM flux. Since the recoil rate for $m_\chi = 10 \text{ GeV}$ is highly suppressed, to avoid spanning ~ 50 orders of magnitude, we do not show this case. In the xenon case, displayed in Fig. 4.9a, coherent enhancement heavily boosts the recoil rate for light dark matter. However, this benefit rapidly diminishes with increasing m_χ as their recoil spectra shift to higher energies. For $m_\chi \gtrsim 1 \text{ GeV}$, the spectrum is weakened across the entire recoil window of XENON1T and Darwin, making them relatively insensitive to heavier Co-SIMPs. On the other hand, Fig. 4.9b illustrates the scenario for scattering off individual protons, which is relevant for detectors like MiniBooNE and Borexino. These detectors are sensitive to higher recoil energies, so they probe deeper into the tail of the CRDM recoil spectrum. Due to the high energies, these detectors are not able to benefit from coherent enhancement. Still, their broader and higher recoil windows allow them to sample the peak of the recoil spectrum more effectively than xenon-based detectors, resulting in higher overall rates, especially for $m_\chi \gtrsim 0.1 \text{ GeV}$. As mentioned, momentum transfers from low to high mass particles are generally less probable. This explains why the peaks tend to shift towards higher recoil energies as m_χ increases, as well as the negligible effects of form factors for small m_χ and low recoil energies. However, form factors become increasingly important at higher recoil energies, visibly suppressing the rates for MiniBooNE and Borexino in the upper end of their respective detection windows. Since nearly all contribution to the CRDM flux stems from protons, we can consider $m_\chi \sim 0.1 \text{ GeV}$ as the mass regime where form factors become prevalent.



(a) Differential recoil rate per xenon nucleus assuming coherent interactions between χ and the nucleons. The highlighted region indicates the analysis window for the XENON1T and Darwin detectors, as listed in Table 3.1.



(b) Differential recoil rate per target nucleon where we take the target to be a proton. The red (orange) highlighted region is the analysis window for the Borexino (MiniBooNE), detector as listed in Table 3.1. These detectors are sensitive to high-energy recoils, so the interactions probe individual protons within the nuclei.

Fig. 4.9: Differential nuclear recoil rates $d\Gamma_{\chi N \rightarrow \chi \chi N} / dT_N$ with $|\mathcal{M}|^2 = C/s$ where $C = 10^{-24} \text{ GeV}^2 \text{ cm}^2$ stemming from the unshielded Co-SIMP CRDM flux. This includes the CRDM flux from the CR species $\psi \in \{\text{p}, \text{H}, \text{C}, \text{O}\}$ both with (solid) and without (dashed) form factors. Attenuation is neglected.

4.4 Constraints

Since CRDM is constrained by the same experiments as any other DM mechanism, obtaining limits simply amounts to requiring $\Gamma_N^\chi = \Gamma_N^{\text{DM}}$. For the xenon based detectors, using (3.35), this implies the equality:

$$\int_{T_N^-}^{T_N^+} dT_N \frac{d\Gamma_{\chi\psi \rightarrow \chi\chi\psi}}{dT_N} = \kappa (\bar{v} \rho_{\text{DM}})^{\text{loc}} \frac{\sigma_{\text{DM}}^{\text{SI}}}{m_{\text{DM}}} A_N^2 \left(\frac{m_N(m_{\text{DM}} + m_p)}{m_p(m_{\text{DM}} + m_N)} \right)^2. \quad (4.39)$$

Note that m_{DM} is to be evaluated at the mass in which corresponds to the lower limit derived from conventional DD on $\sigma_{\text{DM}}^{\text{SI}}$, and *not* set equal to m_χ . Since the left-hand side of this equation contains the same coherence factor A_N^2 , they cancel out. Additionally, since both sides measure the same momentum transfers, the form factor contributions may be neglected in the detector. We note that this final statement is an approximation. If the recoil spectrum is significantly shifted towards the higher momentum transfers, then form factor suppression on one side of the equality in (4.39) would be more prevalent. As seen in Fig. 4.9a this could be relevant for $m_\chi \gtrsim 0.1 \text{ GeV}$ as the recoil spectrum inside the cyan region is skewed to higher energies. For MiniBooNE and Borexino this is simpler as we just have a single interaction rate to compare to, as listed in Table 3.1. Note that for these detectors we must include the form factors for a consistent comparison.

By numerically computing the Co-SIMP CRDM interaction rate, we find the normalization constant C in the matrix element $|\mathcal{M}|^2$ which aligns our interaction rates with the given limit. This then allows us to compute the full, properly normalized, cross section for the interaction $\chi p \rightarrow \chi\chi p$, which determines our bounds. We define this lower limit as:

$$\sigma_\chi^{\text{SI}} \equiv \int_{T_p^-}^{T_p^+} dT_p \frac{d\sigma_{\chi p \rightarrow \chi\chi p}}{dT_p} \Bigg|_{C \text{ s.t. } \Gamma_N^{\text{CRDM}} = \Gamma_N^{\text{DM}}}, \quad (4.40)$$

where T_p^\pm are integration limits stemming from a relabeling of (4.21).

There is an ambiguity in the choice of energy scale we evaluate σ when presenting these limits. In $2 \rightarrow 2$ scattering, the non-relativistic limit is the natural choice; such a limit does not exist in $2 \rightarrow 3$ processes. Additionally, since $\sigma(s = s^{\min}) = 0$, this will not do us any good either. Therefore, we choose to evaluate σ at the CM energy scales:¹⁵

$$E_1^{\text{ref}} \equiv 3m_\chi + m_p, \quad E_2^{\text{ref}} \equiv 2m_\chi + 2m_p. \quad (4.41)$$

To more easily see which region of the cross section this corresponds to in Fig. 4.1, we note that in the RF of the initial-particle χ , this corresponds to the proton kinetic energies

$$T_{p,1}^{\text{ref}} = 2m_p + 4m_\chi, \quad T_{p,2}^{\text{ref}} = \frac{3m_p^2}{2m_\chi} + \frac{3m_\chi}{2} + 3m_p. \quad (4.42)$$

We provide two alternatives as each of these have some drawback when it comes to interpreting the results. In particular, when $m_\chi \ll m_p$ then the cross section at E_1^{ref} becomes heavily suppressed since in this limit $\sigma(E_1^{\text{ref}}) \approx \sigma(\sqrt{s^{\min}}) \approx 0$, thus making our

¹⁵There is a third alternative which was considered but not adopted. Setting $|\mathcal{M}|^2 = \text{const}$ and $G(Q^2) = 1$, then $\sigma_{2 \rightarrow 3} \rightarrow \text{const.}$ as $s \rightarrow \infty$. As far as we are aware, this is the only constant quantity in $2 \rightarrow 3$ scattering and could have served as a reference. However, this constant tends to align with the peak of σ and thus over-represent the magnitude of the cross section compared to the cross section of a ‘typical’ interaction.

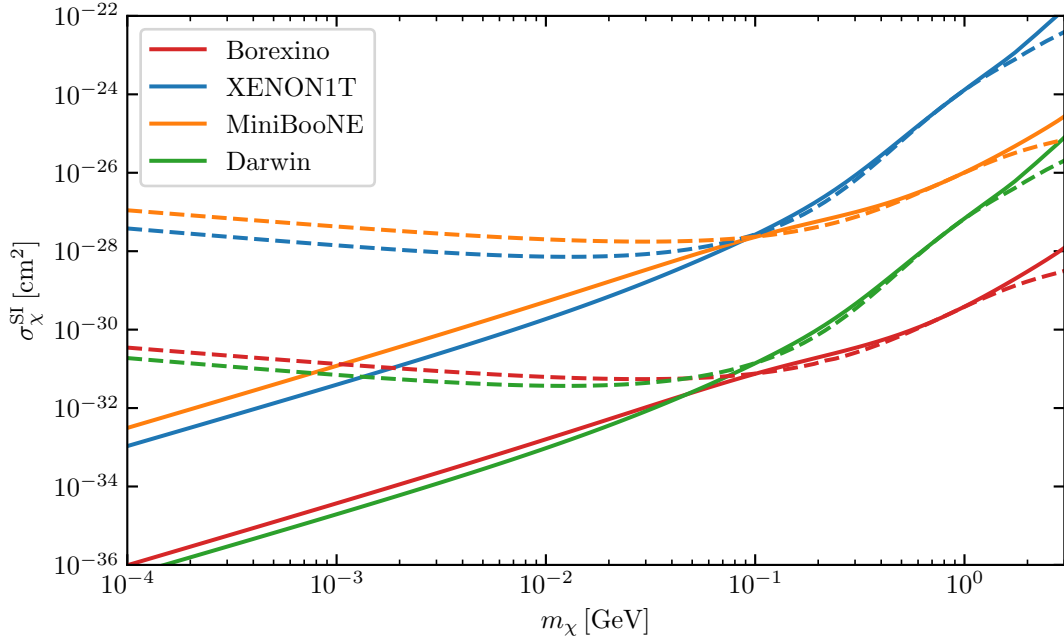


Fig. 4.10: The lower limits on the detectable proton cross section σ_χ^{SI} at the reference scales E_1^{ref} (solid) and E_2^{ref} (dashed) from (4.41) stemming from the Co-SIMP CRDM flux.

limits seem stronger than they actually are. Conversely, with E_2^{ref} then in the case that $m_\chi \gg m_p$, we encounter the same issue. As such, we believe the best approach is to provide both cases and interpret the results with their respective biases in mind.

We stress that this only provides a lower bound on the cross section, as attenuation is neglected. In reality, if the cross section becomes large, interactions with the overburden would start coming into effect. As mentioned in Section 3.4, this would cause the CRDM to undergo frequent interactions while passing through the Earth's surface and atmosphere, resulting in significant energy loss and, in severe cases, preventing it from ever reaching the detector.

Fig. 4.10 shows the results discussed above for the $2 \rightarrow 3$ scattering cross section off protons, derived for the detectors listed in Table 3.1. Attenuation from the overburden is neglected, and we instead determine the smallest normalization of the cross section that would allow detection of the unshielded Co-SIMP CRDM flux. We observe that, while detectors such as XENON1T impose much stronger constraints in conventional dark matter scenarios than, for example, MiniBooNE, their lower limits here are comparable. This again arises from the suppression at low recoil energies discussed in (4.38), which forces xenon based detectors—which are sensitive to low recoil energies—to sample the high-energy tail of the CRDM spectrum. In contrast, MiniBooNE probes much higher recoil energies, corresponding to interactions with individual protons. Borexino, being kinematically similar to MiniBooNE but with tighter experimental constraints, therefore outperforms both XENON1T and MiniBooNE in setting lower limits on the $2 \rightarrow 3$ Co-SIMP interaction. Even the future Darwin experiment, which features the strongest projected constraints among all considered detectors, achieves a sensitivity only comparable to Borexino in this context, and is dominated by Borexino at high m_χ .

As we mentioned at the end of Chapter 3, CRDM typically contains mass independent constraints on the cross section for $m_\chi \lesssim 0.1 \text{ GeV}$ due to the spectral index $\gamma \sim 3$.

However, here we see that $m_\chi \ll m_p$, the solid curves follow a power law $\sigma_\chi^{\text{SI}}(E_1^{\text{ref}}) \propto m_\chi^2$. At first, this was considered an exception to this standard rule. It was not until later that we realized that this was simply due to the energy scale in which we evaluated the cross section at, as confirmed by the inverse proportionality for the dashed lines. Thus, there seems to be some in-between energy scale between the chosen reference scales which reproduces this mass independence. A curious feature is that, for all curves, at $m_\chi \sim 0.1 \text{ GeV}$ the limits from both reference scales intersect, even if these scales do not coincide at this value. Since interactions with protons produce the vast majority of the Co-SIMP CRDM flux, this could be interpreted as the point where form factor effects become relevant, and begin to suppress the difference between the two estimates. On the other hand, the exact overlap at $m_\chi = m_p$ is expected since the reference energy scales coincide. In any case, the upcoming results are insensitive to the specific choice of reference energy scale.

Next, we can use the normalization constant C to relate these constraints to the results in [5], shown in Fig. 2.3. These constraints are shown via the thermally averaged cross section $\langle\sigma_{32}v^2\rangle$. Setting $\alpha = 3$ and $\beta = 2$ in its definition in (2.6). By considering the non-relativistic limit where we approximate $E_i \approx m_i$, then the product inside the brackets above simply reduces to $(8 \prod_{i=1}^3 m_i)^{-1}$ since

$$n_i \equiv \int \frac{d^3 p_i}{(2\pi)^3 2E_i} f_i. \quad (4.43)$$

Evaluating the 2-body phase space then yields the result

$$\langle\sigma_{32}v^2\rangle \stackrel{\text{NR}}{\approx} \frac{1}{2} \frac{1}{8m_\chi^2 m_\psi} \frac{\sqrt{\lambda(s, m_\chi^2, m_\psi^2)}}{8\pi s} \left| \mathcal{M}_{3 \rightarrow 2} \right|^2 \Bigg|_{s=(2m_\chi+m_p)^2}. \quad (4.44)$$

The above does not represent a true thermal average, but rather a threshold evaluation where all initial-state particles are assumed to be at rest. To estimate the possible error, suppose instead that the distribution functions are sharply peaked around relativistic energies, such as $E_i = 2m_i$. In that case, the resulting expression would differ by a factor of roughly 1/8. However, in the context of thermal freezeout, such high energies are strongly Boltzmann suppressed, making this a conservative upper bound on the error. A similar estimate can be made for the phase space factor by comparing its value at threshold, $s^{\min} = (2m_\chi + m_p)^2$, to that at a reference energy E_1^{ref} . Defining the kinematic factor as $f(\sqrt{s})$, then $f(\sqrt{s^{\min}})/f(E_1^{\text{ref}}) \sim [0.6, 0.85]$ across the full m_χ range. Thus, we consider this deviation as a potential factor of 1/2. Note that E_2^{ref} is not relevant in this context: for $m_\chi \ll m_p$, it yields highly relativistic χ , which are Boltzmann suppressed, while for $m_\chi \gg m_p$, it coincides with $\sqrt{s^{\min}}$. In the intermediate region, $m_\chi \sim m_p$, it matches E_1^{ref} , so no additional insight is gained. Thus, we estimate (4.44) to be maximally 16 times smaller than the true value of $\langle\sigma_{32}v^2\rangle$. We expect a more realistic error estimate to be $\lesssim 2$.

Finally, to link our results to the thermal Co-SIMP scenario we impose that $|\mathcal{M}_{3 \rightarrow 2}|^2 = |\mathcal{M}_{2 \rightarrow 3}|^2 = C/s$ and use (4.44). With this, the lower limits on $\langle\sigma_{32}v^2\rangle$ from Co-SIMP CRDM are obtained, and shown in Fig. 4.11. Here, the colored regions show the limits discussed in Section 2.5 where we note that the nucleophilic Ωh^2 limits have been estimated in accordance with Fig. 2.3. Additionally, the solid colored lines indicate the minimum thermally averaged cross section needed for CRDM to be detected by current or future detectors, assuming no attenuation on the lower bound. To estimate an upper bound, we impose an optimistic condition $\sigma_\chi^{\text{SI}} \lesssim 10^{-26} \text{ cm}^2$, evaluated at the

energy scales $\sqrt{s} = E_1^{\text{ref}}$ (solid black) and $\sqrt{s} = E_2^{\text{ref}}$ (dashed black), as discussed below (4.40).¹⁶ Any point above these curves corresponds to cross sections likely incompatible with overburden transparency, based on an optimistic estimate of the upper limits in [7].

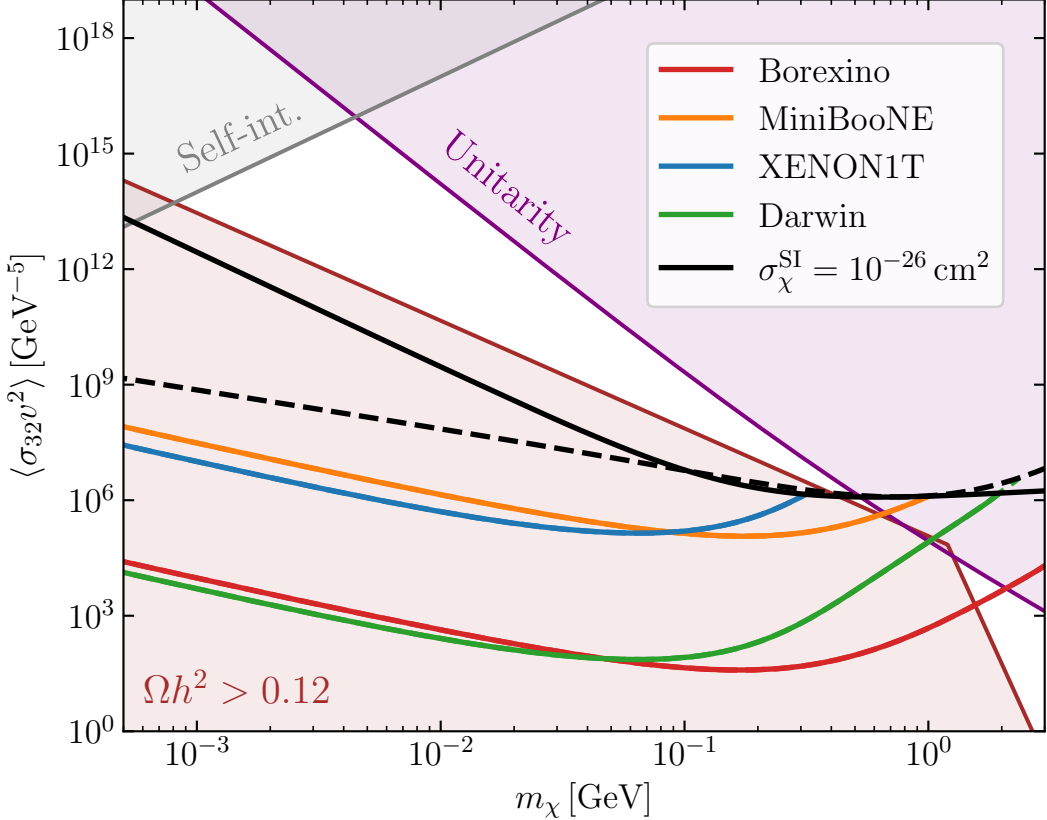


Fig. 4.11: Thermal Co-SIMP parameter space showing the $3 \rightarrow 2$ thermally averaged cross section $\langle\sigma_{32}v^2\rangle$ as a function of m_χ . The brown shaded region is excluded by relic overabundance ($\Omega h^2 > 0.12$), while theoretical bounds from unitarity and self-interactions are also indicated. We note that the relic abundance limit is simply a visual interpolation of the corresponding limit in Fig. 2.3 [5]. The solid colored lines represent lower limits on $\langle\sigma_{32}v^2\rangle$ from CRDM scattering in various detectors: XENON1T (blue), Borexino (red), MiniBooNE (orange), and Darwin (green), assuming the matrix element $|\mathcal{M}|^2 = C/s$ and no attenuation. The solid (dashed) black line shows an estimated upper bound, found by requiring $\sigma_{\chi p \rightarrow \chi p} \lesssim 10^{-26} \text{ cm}^2$ at the reference scale E_1^{ref} (E_2^{ref}).

The resulting picture is rather pessimistic: the large annihilation cross sections required to match the relic density require that the scattering cross section is enormous. Even under optimistic assumptions, the current CRDM limits fail to exclude Co-SIMPs for $m_\chi \lesssim 1 \text{ GeV}$. The only detector with a standing chance to supply any bounds given this analysis is Borexino surrounding $m_\chi \sim 1 \text{ GeV}$. However, this region is not what is of interest for a Co-SIMP history, since this corresponds to a WIMP-like freezeout via $\chi\chi \rightarrow \chi\bar{p}p$ as opposed to the Co-SIMP freezeout $\chi\chi p \rightarrow \chi p$.

¹⁶The energy scale ambiguity applies only to the upper bounds in this plot, since the lower bounds are obtained directly from the observed rate.

4.5 Energy Loss of $2 \rightarrow 3$ Interactions

Until now, attenuation has been neglected in our analysis, relying only on optimistic estimates based on the upper limits in [7]. We then attempted to continue by including the shielded Co-SIMP CRDM flux. However, as shown in the previous section, the cross sections required to avoid Co-SIMPs overclosing the universe, $\Omega_{\text{DM}} h^2 \leq 0.12$, are typically large: $\sigma_{2 \rightarrow 3} \gtrsim 10^{-25} \text{ cm}^2$. Assuming similar attenuation thresholds apply as in $2 \rightarrow 2$ CRDM processes, such high cross sections result in severe suppression due to interactions with the Earth's crust and atmosphere—washing out nearly all CRDM with energies above the $2 \rightarrow 3$ kinematic threshold. This raises the question of whether $2 \rightarrow 3$ processes might offer a kinematic advantage when propagating through a medium.¹⁷

As a simple check, we analyze the average reduction in energy of an incoming Co-SIMP due to a single interaction in the Earth's crust. The idea is that if $2 \rightarrow 3$ kinematics allow for a smaller energy loss per collision than $2 \rightarrow 2$ scattering, then Co-SIMPs might still penetrate the overburden. Relabeling (3.26), the average energy loss for this specific process is

$$\langle \omega_{2 \rightarrow 3}^\chi \rangle = [\sigma_{\chi N \rightarrow \chi \chi N}]^{-1} \int d\Pi_3 \frac{d\sigma_{\chi N \rightarrow \chi \chi N}}{d\Pi_3} \omega_{2 \rightarrow 3}^\chi, \quad (4.45)$$

where $d\Pi_3$ is the 3-body LIPS, $\omega_{2 \rightarrow 3}^\chi$ is the energy lost by the incoming χ in a single interaction. For Co-SIMPs we have an ambiguity in the definition of $\omega_{2 \rightarrow 3}^\chi$, since there are two χ particles in the final state. The most optimistic estimate is to take the maximal energy of the two as this corresponds to minimal energy loss. Using the same parametrization as in the CF as shown in Fig. 4.3, relabeling $\psi \rightarrow N$ and adopting the Earth frame (where $N(p_2)$ is at rest), we define

$$\omega_{2 \rightarrow 3}^\chi \equiv E_1 - \max[E_3, E_4]. \quad (4.46)$$

Using (4.5) and (4.4), we can relate the energies in the RF of $N(p_2)$ to the other Mandelstam variables:

$$\omega_{2 \rightarrow 3}^\chi = \frac{1}{2m_N} \min[s_{45} - t_{13}, s_{35} - t_{14}] - \frac{m_N}{2}. \quad (4.47)$$

Since ω is the only frame-dependent quantity¹⁸ in (4.45), we may reuse the calculation done for the full cross section. This allows us to insert $\omega_{2 \rightarrow 3}^\chi$ into (4.15), and divide this by the integrated cross section to compute $\langle \omega_{2 \rightarrow 3}^\chi \rangle$. For comparison, we will also include the corresponding average energy loss in elastic scattering. In this case $\omega_{2 \rightarrow 2}^\chi = T_N = -t/(2m_N)$ which, for a matrix element which is independent of t , yields the average energy loss per interaction:

$$\langle \omega_{2 \rightarrow 2}^\chi \rangle = \frac{\int_{t^-}^{t^+} dt \frac{d\sigma}{dt} \omega_{2 \rightarrow 2}^\chi}{\int_{t^-}^{t^+} dt \frac{d\sigma}{dt}} = \frac{m_\chi^2}{m_N} + \frac{1}{4m_N s} (s + m_\chi^2 - m_N^2)^2, \quad (4.48)$$

where t^\pm corresponds to t evaluated at the CM angle $\cos \theta' = \pm 1$.

The nuclear composition of Earth's crust is location-dependent, but oxygen is generally the most abundant element, on average constituting 46.1% [97]. Given its dominance,

¹⁷The result of this section is unsurprising, and it was not expected to change our initial assumptions. Still, quantifying how prevalent attenuation has been proved useful for ruling out this approach, and motivates certain assumptions in the next section.

¹⁸In the sense that ω takes a different form depending on the frame in which it is defined.

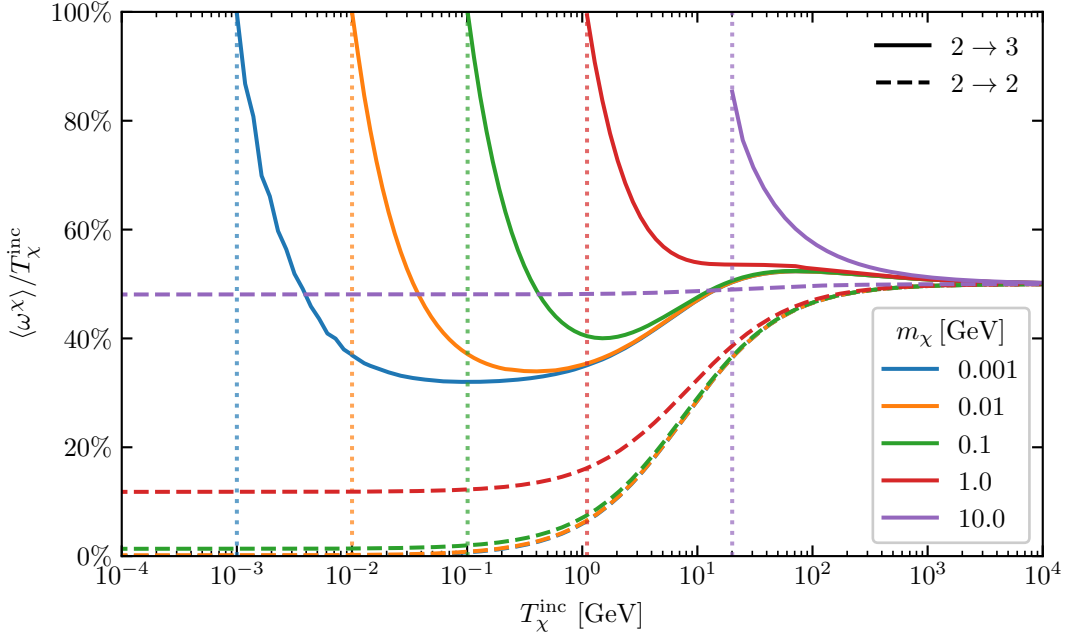


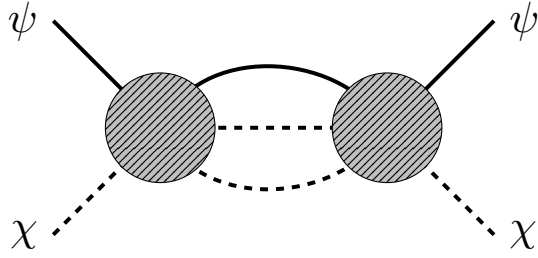
Fig. 4.12: The average energy loss $\langle \omega \rangle / T_\chi^{\text{inc}}$ as a function of the incoming energy T_χ^{inc} with $G_{\text{O-16}}(Q^2) = 1$. The incoming particle is χ , which scatters off an initially at rest oxygen nucleus. Solid lines correspond to the $2 \rightarrow 3$ Co-SIMP process, while dashed lines represent the analogous $2 \rightarrow 2$ elastic scattering. Dotted vertical lines indicate the minimal T_χ^{inc} required for the $2 \rightarrow 3$ process to occur.

we consider scattering processes involving oxygen nuclei as representative of terrestrial attenuation effects as shown in Fig. 4.12 where we set $G(Q^2) = 1$. Here $\langle \omega \rangle / T_\chi^{\text{inc}}$ is given as a function of the incoming kinetic energy T_χ^{inc} , thus representing the fractional energy loss of the most energetic outgoing χ at different energy scales.

There is a significant difference at the energy scale where the $2 \rightarrow 3$ process initially kinematically allowed. When $m_\chi \ll m_N$, at the threshold $T_\chi = T_\chi^{\min} = 3m_\chi^2/(2m_N) + m_\chi$, nearly all of the kinetic energy is converted to rest mass, with energy loss approaching 100%.¹⁹ As m_χ approaches m_N this effect weakens. Here the 3-momentum of the incoming CRDM is no longer negligible. This forces the particles to still maintain some forward motion after the interaction. This is of course the case even when $m_\chi \ll m_N$, but since χ has such low mass, a slight momentum transfer to the nucleus is sufficient to preserve momentum.

While unsurprising, these results look grim for terrestrial detection of pure $2 \rightarrow 3$ Co-SIMP interactions. The energy loss—even in the most optimistic case—is greater than in $2 \rightarrow 2$ for all m_χ and energy scales, eventually converging in the ultra-relativistic limit where the energy requirement of the production of another χ is negligible. We additionally considered form factors in both cases; this ended up helping slightly in the high-energy regime, but form factor suppression of the attenuation in $2 \rightarrow 2$ is much more prevalent. Thus, the energy loss turned out to be orders of magnitude higher for $2 \rightarrow 3$ compared to $2 \rightarrow 2$ with this inclusion. This makes sense from the standpoint that high-energy scattering with form factors will suppress high momentum transfers to

¹⁹While it is not visible in this figure, the lines never exceed nor arrive at 100%, but as $m_\chi/m_N \rightarrow 0$ it seems to get arbitrarily close to 100%.


 Fig. 4.13: Elastic $\chi\psi \rightarrow \chi\psi$ induced at two-loop level.

the nucleus. As such, configurations which evenly distribute energy among the two χ particles will dominate. Since we are looking at the most energetic of the two, this does not help our case much compared to elastic scattering.

The combined effect of high energy loss per interaction and requiring large cross sections and means that the vast majority of CRDM with $T_\chi > T_\chi^{\min}$ will be washed out in the overburden, creating a cascade of DM with insufficient energy for the interaction to occur again in the detector. As a result, applying the upper limits for $2 \rightarrow 2$ to $2 \rightarrow 3$ is poorly motivated, implying that the upper limits in Fig. 4.11. Due to this, we note that the region at $m_\chi \sim 1$ GeV in Fig. 4.11 covered by Borexino must be discarded. With this conclusion, to set limits on Co-SIMPs via CRDM, one needs to either consider detectors that are not shielded by the Earth's crust or atmosphere, e.g. extraterrestrial detectors, or a subdominant process.

However, this analysis omits all phase space structure. For example, as was seen in Fig. 4.1, at $T_\chi \approx T_\chi^{\min}$ there is a strong suppression stemming from the cross section. Such details are not represented in Fig. 4.12. As such, a fraction of these CRDM may make it through the overburden and reach the detector, and we do not exclude the possibility that a full treatment of $2 \rightarrow 3$ attenuation may yield some positive results. That said, this particular example is not very promising, as Co-SIMPs near threshold are not energetic enough to produce observable recoils given that the $2 \rightarrow 3$ interaction reoccurs. Although, a UV completed matrix element may suppress configurations of maximal energy loss, in which the impact of attenuation would be less dominant.

4.6 Two-Loop Elastic Co-SIMP Scattering

With the conclusion reached in the previous section, the natural next step is to look for a potential workaround. The alternative approach which may still make use of terrestrial detectors is to consider the elastic scattering of Co-SIMPs induced at 2-loop order which is depicted in Fig. 4.13. At this level, even for very large cross sections, these contributions could be heavily suppressed, allowing for the Co-SIMP CRDM to make it through the overburden and into the detector. This is in fact exactly what was considered in [5], but without the CRDM component.

Recoil Rates

Since the CRDM component energetic enough for the $2 \rightarrow 3$ process is likely stopped by the overburden, only Co-SIMPs with sub-threshold energies can reach the detector. This

corresponds to an upper bound on the integration limits

$$T_\chi^+ = \frac{3m_\chi^2}{2m_{\text{HA}}} + m_\chi, \quad (4.49)$$

where m_{HA} is the mass of the heaviest abundant nucleus in the overburden.

The Earth's crust is composed of approximately 46.1% oxygen, 28.2% silicon, 8.23% aluminum, 5.63% iron [97]. The next element which is heavier than iron is barium with a much lower abundance of 0.0425% [97]. Thus, it is clear that the most conservative and physically motivated choice is to take ^{56}Fe as our candidate for the heaviest abundant isotope. The two less conservative options are taking either ^{28}Si or ^{16}O as m_{HA} which will allow for our upper integration bound to be higher, sampling higher energy components of the Co-SIMP CRDM flux. We note that for any $m_\chi \ll m_{\text{HA}}$ —which is generally the case even with ^{16}O as our target for the $m_\chi \lesssim 1 \text{ GeV}$ which are most relevant for CRDM—this choice is mostly irrelevant as $T_\chi^+ \approx m_\chi$ in this limit.

Now, since this process is the familiar $2 \rightarrow 2$ scattering, we may make use of the functions in `DarkSUSY` [6] to take into account the full effects of attenuation and calculate the 2-loop induced interaction rate as before:

$$\Gamma_N^{\text{2-loop}} = \int_{T_N^-}^{T_N^+} dT_N \int_{T_\chi^-}^{T_\chi^+} dT_\chi \frac{d\sigma_{\chi N \rightarrow \chi N}}{dT_N} \frac{d\Phi_\chi}{dT_\chi}. \quad (4.50)$$

Here, $d\Phi_\chi/dT_\chi$ is the CRDM flux stemming from *both* $2 \rightarrow 3$ interactions and the 2-loop elastic channel, T_χ^- is a simple relabeling of (3.4):

$$T_\chi^- = \frac{T_N}{2} - m_\chi + \sqrt{\left(\frac{T_N}{2} - m_\chi\right)^2 + \frac{T_N}{2m_N}(m_N + m_\chi)^2}, \quad (4.51)$$

and $d\sigma_{\chi N \rightarrow \chi N}/dT_\chi$ will be derived below. We recall that when including attenuation, $T_\chi^- = T_\chi(T_\chi^{z,-})$ and T_χ in $d\sigma_{\chi N \rightarrow \chi N}/dT_N$ must be evaluated at T_χ^z as explained below (3.33).

Even with the full attenuation treatment, the rate in (4.50) remains a conservative estimate. This is because the $2 \rightarrow 3$ scattering process, which dominates at $T_\chi > T_\chi^+$, also generates secondary Co-SIMPs with lower energies $T_\chi < T_\chi^+$. This cascade will in principle contribute to the flux reaching the detector. Since the high-energy CRDM flux is significant, we expect this secondary cascade to be especially relevant for low m_χ , where the energy loss per interaction is smaller. Incorporating this effect would require modifying the incoming flux accordingly. However, such a full treatment is beyond the scope of this thesis.

The need to impose an upper bound on the integration region in (4.50) clearly limits the ability to constrain low values of m_χ , since smaller masses require much less energy for the $2 \rightarrow 3$ interaction to be kinematically accessible. This is closely analogous to the issue encountered in direct detection of halo dark matter, where for any given m_{DM} , the DM velocity distribution imposes an effective upper bound on the recoil energy. To determine which m_χ values which can be probe in this setup, we examine when $T_\chi^- = T_\chi^+$ in (4.50). Specifically, we evaluate $T_\chi^-(T_N^-)$, where T_N^- is the lower threshold of the detectors recoil energy window, and numerically solve for m_χ . For the XENON1T detector, this yields $m_\chi \sim 10^{-2} \text{ GeV}$. Similarly, evaluating $T_\chi^-(T_N^+)$, which corresponds to the upper recoil threshold, we find $m_\chi \sim 3 \times 10^{-2} \text{ GeV}$. This implies that only Co-SIMPs with $m_\chi \gtrsim 3 \times 10^{-2} \text{ GeV}$ can contribute fully across the detector window. Masses in the range $m_\chi \in [10^{-2}, 3 \times 10^{-2}] \text{ GeV}$ will be suppressed due to a restricted integration

range, and masses $m_\chi \lesssim 10^{-2}$ GeV are entirely inaccessible in XENON1T. The effect is even more pronounced for detectors with higher recoil thresholds, but becomes less severe when the target nucleus is lighter. For example, the analogous sensitivity range for Borexino is in range $m_\chi \in [5 \times 10^{-2}, 0.6]$ GeV, aided by the fact that at these energies the interaction proceeds via scattering off individual protons.

Despite these limitations, Fig. 4.11 shows that certain mass regimes remain within reach via the 2-loop process, though the low m_χ region will not be accessible. To model the flux cutoff more realistically, we note that the $2 \rightarrow 3$ cross section is strongly suppressed near $T_\chi \sim T_\chi^+$. Rather than imposing a sharp cutoff, we implement a smooth suppression factor that suppresses off the flux above this point, allowing some contribution from energies just above the threshold. The modified flux used in (4.50) takes the form:

$$\frac{d\Phi_\chi}{dT_\chi} \rightarrow \frac{d\Phi_\chi}{dT_\chi} \times \begin{cases} 1, & T_\chi \leq T_\chi^+, \\ \exp \left[-200 \left(\frac{T_\chi}{T_\chi^+} - 1 \right)^2 \right], & T_\chi^+ < T_\chi < 1.2 T_\chi^+, \\ 0, & T_\chi^+ \geq 1.2 T_\chi^+. \end{cases} \quad (4.52)$$

We do not believe the above is the most realistic way of smoothing the suppression and minimal testing has been done with other cutoff functions. Fig. 4.1 shows that the slope of the kinematic regions vary significantly based on the mass of the CRDM. Ideally, one would find a cutoff which mimics this well, e.g. change $1.2 \rightarrow A m_\chi / m_{\text{HA}}$ for some constant A . Alternatively, one can tailor a specific smooth cutoff for the relevant mass regimes of each detector. However, even a sharp cutoff would not meaningfully affect any of the primary results.

Dynamics

Then all that remains is to connect the 2-loop diagram in Fig. 4.13 to $\langle \sigma_{32} v^2 \rangle$ and thus $|\mathcal{M}_{2 \rightarrow 3}|^2$, which will set the corresponding Co-SIMP CRDM flux for the interaction strength. By treating the ‘blob’ in Fig. 4.3 as a vertex we may write the leading effective interaction term for Co-SIMPs as

$$\mathcal{L} \supset \frac{1}{\Lambda^2} \chi^3 \bar{\psi} \psi. \quad (4.53)$$

By following the prescription in [98], one can show that [5]

$$\langle \sigma_{32} v^2 \rangle \approx \frac{\sqrt{3}}{4\pi m_\chi \Lambda^4}. \quad (4.54)$$

Now, all we need is to connect Λ to the 2-loop diagram. By inspection, we see that the diagram in Fig. 4.13 has a superficial degree of divergence $D = 3$ and thus diverges. To evaluate this diagram we regularize this loop via a cut-off scale, which we take to be the same Λ as above since perturbation theory breaks down past this point. Then with the momentum labeling $\psi(p_1)\chi(p_2) \rightarrow \psi(p_3)\chi(p_4)$, the effective (non-squared) 2-loop matrix element can be written as²⁰

$$\begin{aligned} \mathcal{M}_{\chi\psi \rightarrow \chi\psi}^{\text{2-loop}} &= \frac{-S}{\Lambda^4} \bar{u}(p_3) \int \frac{d^4 k}{(2\pi)^4} \frac{d^4 q}{(2\pi)^4} \left[(\not{k} + m_\psi)((k-q)^2 + m_\chi^2)((p_1 + p_2 - k)^2 + m_\chi^2) \right]^{-1} u(p_1) \\ &\quad + \mathcal{O}(\Lambda^{-3}) \\ &\equiv c_\psi \bar{u}(p_3) u(p_1) + \mathcal{O}(\Lambda^{-3}). \end{aligned} \quad (4.55)$$

²⁰The attentive reader may notice that this is a first order expansion of a strongly interacting theory. We discuss the validity of this analysis in Chapter 5. Also, we write $\mathcal{O}(\Lambda^{-3})$ since performing the leading order integrals with Λ as an explicit cutoff gives $\mathcal{O}(\Lambda^{-2})$, as manifest in (4.57).

Here k and q are the loop momenta, S is the symmetry factor of the diagram, and in the final equality we introduced a calculable coefficient c_ψ .

This coefficient can now be treated as an effective coupling to a four-point interaction term of the form²¹

$$\mathcal{L} \supset c_\psi \chi^2 \bar{\psi} \psi. \quad (4.56)$$

Performing the q integral in (4.55) gives that [5]

$$\begin{aligned} c_\psi &= \frac{m_\psi}{(4\pi)^2 \Lambda^4} \int \frac{d^4 k}{(2\pi)^4} \ln\left(\frac{x+1}{x-1}\right) \left(\frac{x}{k^2 - m_\psi^2}\right) \\ &\approx \frac{m_\psi}{(4\pi)^4 \Lambda^2} \left[1 - \frac{m_\chi^2}{\Lambda^2}\right] \ln\left[\frac{\Lambda^2 + m_\psi^2}{4m_\chi^2}\right], \end{aligned} \quad (4.57)$$

where $x \equiv \sqrt{1 - 4m_\chi^2/k^2}$. With the above approximations, we emphasize that one can not neglect the logarithmic factor in (4.57) as this term typically evaluates to 0.1–10 for the relevant values of $\langle \sigma_{32} v^2 \rangle$ in our parameter space.

Note that in the above we have assumed that the target particle in the detector is a fermion. The treatment of scalar targets is introducing an effective operator of the form $\mathcal{L} \supset \Lambda^{-1} \chi^3 \phi^2$, which generates the elastic term $c_\phi \chi^2 \phi^2$ where c_ϕ is obtained by computing its corresponding 2-loop diagram. However, we will neglect this detail as it introduces only $\mathcal{O}(1)$ discrepancies, which will primarily affect the limits from the XENON1T and Darwin detectors.

Since we can now connect c_ψ to $\langle \sigma_{32} v^2 \rangle$, which in turn sets the normalization of the $2 \rightarrow 3$ matrix element, we may compute the Co-SIMP CRDM flux with the value that satisfies $\Gamma_N^{2\text{-loop}} = \Gamma_N^{\text{DM}}$. All we need is the 2-loop differential cross section. A direct calculation with the new effective interaction term in (4.56) yields the spin-averaged matrix element squared

$$|\mathcal{M}_{\chi\psi \rightarrow \chi\psi}^{\text{2-loop}}|^2 = c_\psi^2 [4m_\psi^2 - t] A_\psi^2 G_\psi^2(Q^2) = 2c_\psi^2 m_\psi [2m_\psi + T_\psi] A_\psi^2 G_\psi^2(2m_\psi T_\psi), \quad (4.58)$$

where we have included the effects of form factors and coherent enhancement, and in the final equality we evaluated t and Q^2 in the RF of the initial particle $\psi(p_1)$. Thus, T_ψ corresponds to the outgoing kinetic energy of particle $\psi(p_3)$ in the detector. With this matrix element, arriving at the differential cross section is straightforward:

$$\frac{d\sigma_{\chi\psi \rightarrow \chi\psi}}{dT_\psi} = \frac{c_\psi^2 m_\psi T_\psi [2m_\psi + T_\psi]}{8\pi \lambda(s, m_\psi^2, m_\chi^2)} A_\psi^2 G_\psi^2(2m_\psi T_\psi). \quad (4.59)$$

Taking $G(Q^2) = 1$ in the above, integrating over T_ψ and taking the non-relativistic limit, one arrives at the non-relativistic 2-loop nucleon–CRDM cross section:

$$\sigma_{\text{NR}} = \frac{c_\psi^2}{4\pi} \left(\frac{m_\psi}{m_\chi + m_\psi} \right)^2. \quad (4.60)$$

Resulting Flux

With a secondary interaction channel contributing to the Co-SIMP CRDM flux, we aim to examine the relative strength of the 2-loop component to the $2 \rightarrow 3$ process. This is

²¹In the language of renormalization, we would say that this term is generated radiatively, but to avoid the topic of counterterms and renormalizability we will stick to this naive approach. For a detailed approach to this subject, we recommend [90] for a great introduction.

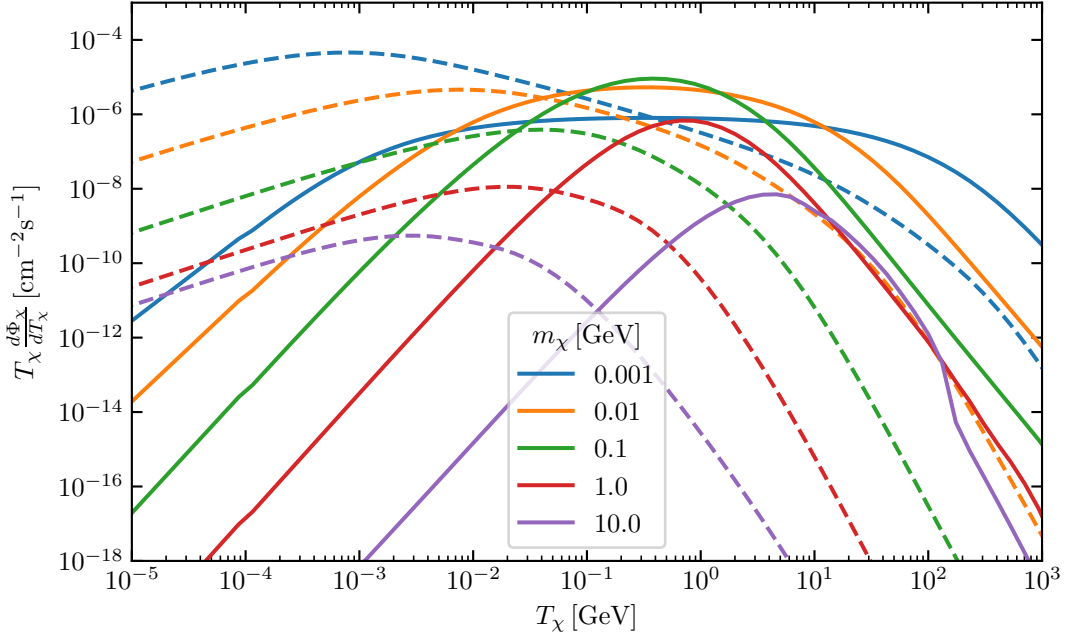


Fig. 4.14: CRDM flux $d\Phi_\chi/dT_\chi$ for both the $2 \rightarrow 3$ process (solid) along with the 2-loop induced process (dashed) both including form factors. In this figure, $\sigma_{\text{NR}}^{\text{2-loop}} = 10^{-30} \text{ cm}^2$ and the corresponding $2 \rightarrow 3$ normalization is $C \approx 2 \times 10^{-22} \text{ GeV}^2 \text{ cm}^2$.

done with the same program which was used to generate the corresponding $2 \rightarrow 2$ flux in Fig. 4.5, but including form factors and connecting the normalization to the $2 \rightarrow 3$ interaction. The result of this is shown in Fig. 4.14 where we include form factors in both cases. At high energies, the flux generated by the elastic process is in general subdominant due to the 2-loop suppression. In the ultra-relativistic limit, neglecting form factors, the ratio $(d\Phi_\chi^{\text{2-loop}}/dT_\chi)/(d\Phi_\chi^{2 \rightarrow 3}/dT_\chi)$ is expected to approach a constant suppression factor, independent of kinematics. However, at the low-energy regime, the 2-loop component can be seen to dominate heavily over the $2 \rightarrow 3$ process due its comparatively lenient kinematic constraints. Since we impose an upper cutoff on T_χ to avoid the $2 \rightarrow 3$ process occurring, this could improve the Co-SIMPs ability to supply the relevant recoil rates in the detector. As such, the resulting flux from 2-loop Co-SIMPs is important for low energy detection, and neglecting it would lead to conservative limits.

Constraints

Figure 4.15 shows the resulting limits on the non-relativistic 2-loop cross section σ_{NR} for the $\chi p \rightarrow \chi p$ process, using the combined Co-SIMP CRDM flux with the detection thresholds listed in Table 3.1. These constraints follow the same procedure as explained in Section 4.4. For Darwin, we make use of the optimistic lower energy threshold. Adopting a more conservative threshold for Darwin would shift the exclusion boundary rightward, aligning its low-mass sensitivity with XENON1T and slightly weakening its overall constraint. We also include the corresponding XENON1T results from [7] with the same parameters as this thesis.

The dashed curves correspond to the limits obtained when the CRDM flux includes only the $2 \rightarrow 3$ contribution. It is clear that this component dominates the exclusion sensitivity. From Fig. 4.14, one might have expected a larger impact from the 2-loop

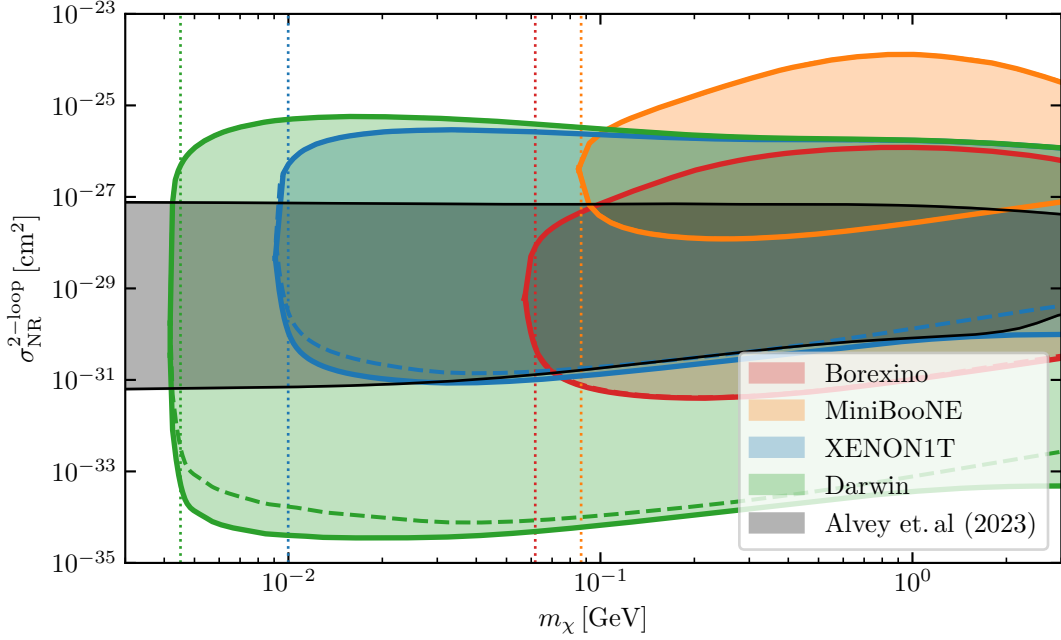


Fig. 4.15: The solid lines are the resulting limits on the non-relativistic 2-loop cross section stemming from the combined Co-SIMP CRDM flux. The dashed lines are the corresponding limits when we neglect the 2-loop contribution to the flux. Both make use of the full attenuation treatment in `DarkSUSY`, including quasi-elastic scattering, hadronic resonances, deep inelastic scattering and a relativistic cross section with form factors included in the attenuation. Additionally, we apply the cut-off for the $2 \rightarrow 3$ process in (4.52) to mimic the suppression from the $2 \rightarrow 3$ flux. The dotted vertical lines show the expected minimal threshold where any given χ has sufficient energy to produce an observable recoil rate in the detector while still having insufficient energy for the $2 \rightarrow 3$ process. Note that for Borexino we have used the unquenched energy such that it represents the actual minimal m_χ to see a signal in the detector. The black shaded region are the analogous XENON1T constraints from [7]. The shaded region within each line indicates which regions each detector excludes when considering the full treatment.

process. However, for the m_χ values accessible to direct detection—i.e., those not excluded by $2 \rightarrow 3$ attenuation—the difference in flux between the two processes is minimal in the relevant energy range. Earlier, we saw the opposite behavior when considering a $2 \rightarrow 3$ process in the detector, which suffers from a low-energy suppression in the cross section. In contrast, the $2 \rightarrow 2$ elastic scattering used here does not experience the same suppression, and thus, the detector response differs accordingly. Furthermore, at low T_χ , where the 2-loop flux is comparatively larger, attenuation severely reduces the number of particles reaching the detector. Since the cross section is not suppressed in this regime, energy loss is significant and renders most of the flux ineffective for producing detectable recoils. As a result, the 2-loop flux provides only a marginal improvement to the constraints, barely becoming visible for Borexino at $m_\chi \gtrsim 2$ GeV. Even there, the dashed lines remain nearly hidden beneath the solid ones, indicating the dominance of the $2 \rightarrow 3$ contribution.

When comparing the XENON1T constraint from [7], we find similar lower limits, stretching down to $\sigma^{\text{NR}} \sim 10^{-31} \text{ cm}^2$ at $m_\chi = 0.1 \text{ GeV}$. However, our upper limits are significantly stronger. The difference lies in our inclusion of the $2 \rightarrow 3$ contribution to the flux. Since this component dominates the exclusion, the total flux is far greater than

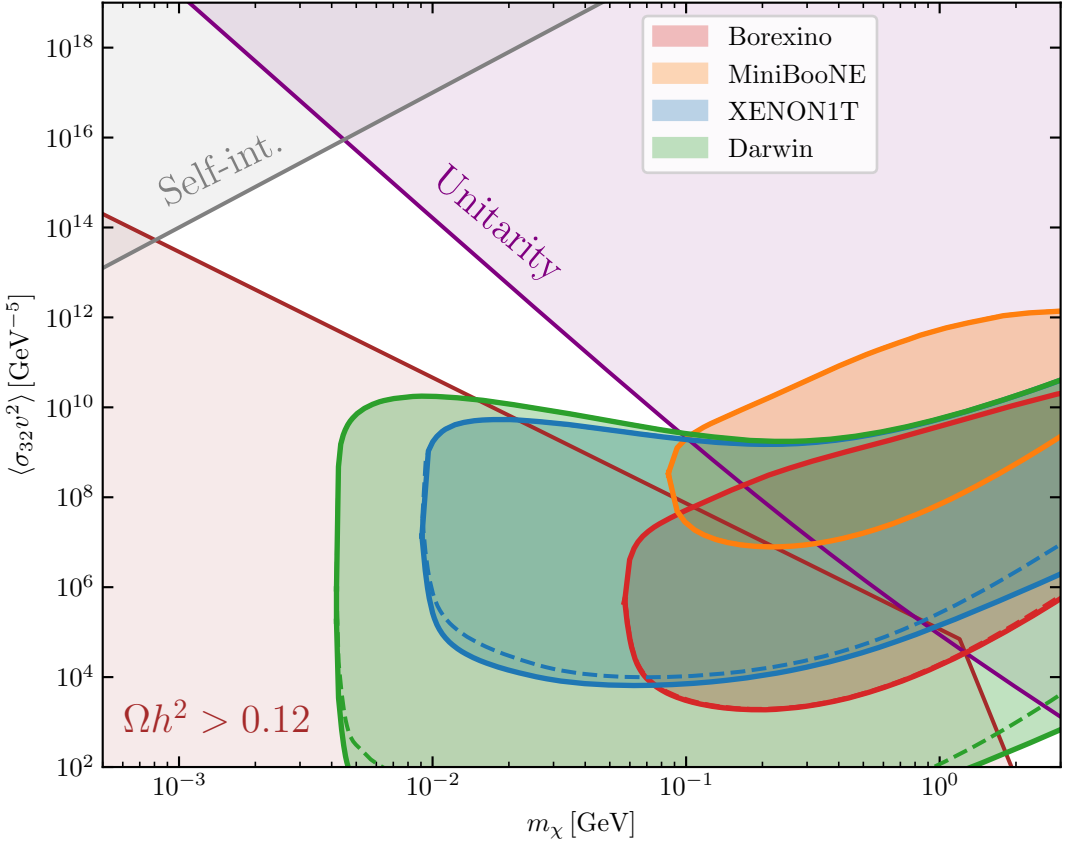


Fig. 4.16: The lower limits $\langle\sigma_{32}v^2\rangle$ evaluated in the non-relativistic limit $s = (2m_\chi + m_p)^2$. A description for the theoretical and detector bounds can be found in Figs. 4.11 and 4.15, respectively.

in the pure elastic scenario. Consequently, even with stronger attenuation, a substantial number of Co-SIMPs are able to reach the detector with sufficient energy. The clearest difference between our figure and that of [7] appears at small m_χ . In the purely elastic case, m_χ can in principle be pushed to the keV scale without significantly altering the limits. In contrast, our analysis is bounded by the $2 \rightarrow 3$ attenuation cutoff. This causes our limits to stop at the vertical dotted lines in Fig. 4.15, extending slightly past them only due to the smooth cutoff implemented in (4.52).

Fig. 4.16 shows the corresponding limits on $\langle\sigma_{32}v^2\rangle$, obtained using the σ^{NR} result above to relate it to the $3 \rightarrow 2$ process. The projected sensitivity of the Darwin experiment covers $m_\chi \in [1, 2] \text{ GeV}$, probing most of this small region. Present-day detectors do not reach this regime, so low-GeV nucleophilic Co-SIMPs remain viable DM candidates. XENON1T, on the other hand, excludes the viable region $m_\chi \in [10^{-2}, 1] \text{ GeV}$ for $\langle\sigma_{32}v^2\rangle \lesssim 10^{10} \text{ GeV}^{-5}$. Above this, attenuation prevents deep underground detectors from probing such large cross sections. A near-surface detector like MiniBooNE, with a low recoil threshold, similar to xenon-based detectors, can probe a large portion of this upper region via the 2-loop channel. If this analysis holds, Co-SIMPs can account for all present-day DM only if $m_\chi \gtrsim 1 \text{ GeV}$ or $m_\chi \in [10^{-3}, 2 \times 10^{-2}] \text{ GeV}$. This concludes our analysis of the CRDM constraints on nucleophilic Co-SIMPs.

Chapter 5

Discussion

This chapter outlines the physical implications, modeling assumptions, and limitations of the results obtained, with a focus on the viability of probing co-scattering strongly interacting massive particles (Co-SIMPs) via the cosmic-ray-boosted dark matter (CRDM) mechanism.

Comparison to Previous Work

Our work differs from previous CRDM studies [4, 7, 35, 36] by focusing on inelastic scattering in strongly interacting dark sectors. While earlier analyses focused on elastic upscattering of sub-GeV halo dark matter, this study investigates a $2 \rightarrow 3$ particle-producing interaction, as naturally expected in the Co-SIMP model. This required generalizing the standard CRDM framework to incorporate nontrivial final-state kinematics. The dynamics were modeled using a phase-space average of the matrix element squared, and the resulting relativistic flux and recoil spectra were implemented in a modified version of `DarkSUSY`.

This inelastic setup leads to several qualitative differences from previous CRDM results. The most pronounced differences appear in the low-energy regime, where the CRDM flux and recoil rates are significantly suppressed. This suppression originates from the combined effects of the falling differential cross section (see Fig. 4.2), the non-monotonic lower integration bound T_χ^- in (4.30), and additional damping from nuclear form factors. The latter arises because, in $2 \rightarrow 3$ scattering, it is the incoming cosmic ray—not the dark matter particle—that imparts momentum to the target. While the two are equivalent in elastic processes, the distinction becomes non-negligible in inelastic scenarios. Another unexpected feature is the minimal role played by heavier cosmic-ray species. In elastic CRDM, heavier nuclei, such as helium, typically dominate the high-energy flux [7]. In contrast, our findings show that their contribution is consistently subdominant across all Co-SIMP masses, a result that follows from the shifted kinematic thresholds and the steeply falling flux of heavy CRs.

Compared to the original Co-SIMP proposal [5]—which considered direct detection of halo DM via $3 \rightarrow 2$ annihilation in the detector along with the 2-loop elastic processes—our results show that cosmic-ray-induced relativistic fluxes offer a qualitatively different handle on the same parameter space. In the $3 \rightarrow 2$ case, interactions require extremely large cross sections due to the interaction rate being proportional to n_χ^2 . In contrast, CRDM-induced fluxes can be detected even with much smaller cross sections—provided attenuation is sufficiently weak—offering a new window into their parameter space.

Modeling Assumptions and Limitations

A core assumption throughout this work is the dominance of a $2 \rightarrow 3$ scattering process in the CRDM production channel. The matrix element was treated as isotropic and modeled as $|\mathcal{M}|^2 \propto 1/s$ to preserve unitarity at high energies. While this is sufficient to characterize the overall scaling and spectral shape, it obscures possible angular structure, dynamic threshold effects, and potential logarithmic enhancements. Although the kinematical treatment is exact, such dynamics are inherently model-dependent.

The major limiting factor in probing Co-SIMPs through CRDM is the strong attenuation these particles experience in the overburden. Because thermal freezeout requires large cross sections, CRDM particles above the $2 \rightarrow 3$ threshold undergo substantial energy loss before reaching underground detectors. A full simulation of $2 \rightarrow 3$ attenuation within the overburden is beyond the scope of this thesis. However, we estimate the impact of energy loss using average energy loss per collision and phase-space suppression arguments. Although it does not capture the full energy evolution of downscattered Co-SIMPs, it provides a reliable estimate of the severity of the attenuation. Even under optimistic assumptions, $2 \rightarrow 3$ events suffer significantly greater energy loss than elastic ones, effectively ruling out the possibility of direct $2 \rightarrow 3$ detection in terrestrial experiments.

The possibility of detecting nucleophilic Co-SIMPs using extraterrestrial detectors was also considered. However, background levels in satellite environments are notoriously high, limiting sensitivity to only the most extreme interaction rates. These rates correspond to Co-SIMP fluxes comparable in magnitude to the proton ICR flux—clearly in conflict with unitarity. This suggests that the uppermost region of the nucleophilic $\langle\sigma_{32}v^2\rangle-m_\chi$ parameter space lies beyond the reach of $2 \rightarrow 3$ processes, as the unitarity bound is seemingly more restrictive than the corresponding bound on the thermally averaged annihilation cross section.

For the attenuation treatment, we noted in Section 3.4 that the energy loss equation in (3.23) assumes the trajectory of the incoming CRDM particle remains unchanged after scattering. This assumption is typically valid when $m_\chi \gg m_N$, since angular deflections per collision are then suppressed. However, in the relevant parameter space where $m_\chi \lesssim 1 \text{ GeV}$, this is not the case. We therefore briefly analyze the validity of this assumption by considering a benchmark with $m_\chi = 0.1 \text{ GeV}$ and $\sigma_{\chi N} = 10^{-28} \text{ cm}^2$, propagating through an overburden composed entirely of oxygen. Using $\rho \approx 2.7 \text{ g/cm}^3$ and $m_N \approx 16 \text{ g/mol}$, the number density is estimated as $n_N \sim 10^{23} \text{ cm}^{-3}$, based on the implementation in DarkSUSY [6]. This yields an expected number of scatterings over 1.4 km of $\mathcal{O}(1)$. Since the typical deflection per collision for $m_\chi \sim m_N$ is $\mathcal{O}(1)$ radian, and our benchmark satisfies $m_\chi \ll m_N$, the deflection angle in our case is likely even larger. However, such large-angle scatterings correspond to large momentum transfers and are therefore strongly suppressed by the nuclear form factor—particularly since light CRDM requires high energies for detection. Thus, such large deflection angles are likely not realistic. On the other hand, the depth used for each detector corresponds to the vertical distance from the surface. For CRDM entering Earth’s crust at an angle, the effective depth the particle must traverse will be greater. While this is the standard approach in CRDM attenuation studies, a more refined treatment would involve tracking both energy and angular deflections, e.g., through Monte Carlo simulations. For the parameter space considered, such an analysis could predict stronger attenuation. Nevertheless, since large-angle scatterings are form factor suppressed and relativistic effects reduce coherence, we do not expect these refinements to produce a large deviation from our results.

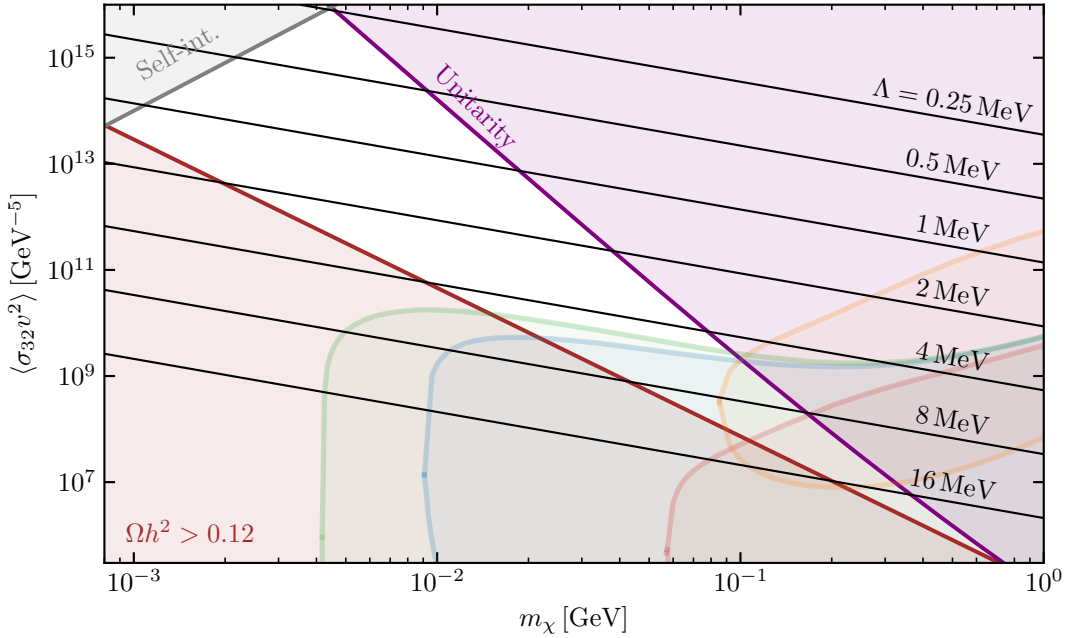


Fig. 5.1: Contour showing the value of Λ in the available Co-SIMP parameter space. A description for the theoretical and detector bounds can be found in Figs. 4.11 and 4.15, respectively.

Two-Loop Channel and Theoretical Validity

Inspired by [5], a subdominant 2-loop elastic channel was considered in Section 4.6. While this interaction is loop-suppressed, it becomes relevant precisely because the flux below the $2 \rightarrow 3$ energy threshold can still survive traversal through the overburden. This channel was modeled using the attenuation formalism developed in [7], which accounts for relativistic kinematics, form factors, and high-energy corrections. In this context, the elastic interaction acts as a detection proxy for the $2 \rightarrow 3$ production mechanism. To connect 2-loop elastic scattering to the thermal $3 \rightarrow 2$ process, it was assumed that the same effective operator governs both interactions, using a leading-order estimate of the induced coupling c_ψ . Since Co-SIMPs are strongly interacting species, such perturbative arguments are not well justified. This discussion can be quantified by considering the relevant energy scale Λ . For the 2-loop analysis to remain physically meaningful, the first-order expansion in (4.55) must provide a good approximation. The minimal expectation is that $\Lambda \gtrsim 5 \text{ GeV}$, as the relevant CM energies for scattering off protons are $\sqrt{s} \gtrsim 1 \text{ GeV}$. Using (4.54), the corresponding contours for Λ are shown in Fig. 5.1.

Clearly, we are far beyond the point where a first-order perturbative expansion in s/Λ^2 can be trusted. Since this approximation underlies all results in this section, the bounds in Figs. 4.15 and 4.16 are not rigorous; nor is the relative normalization of the flux in Fig. 4.14, which inherits the same uncertainty. This issue also affects the constraints presented in [5] which are based on the same 2-loop diagram. Moreover, their analysis does not acknowledge the breakdown of the effective theory, even though their bounds extend deeper into the regime where $\sqrt{s} \gg \Lambda$ and the expansion is even less reliable.

Despite this, the situation is not entirely pessimistic. Although the perturbative expansion breaks down for $\sqrt{s} \sim \Lambda$, dimensional analysis—combined with the absence of new thresholds—suggests that the qualitative scaling of the cross section may still be approximately preserved. Provided these corrections do not significantly enhance the

two-loop contribution to the point where attenuation dominates, or suppress it so strongly that the signal becomes undetectable, we expect the overall scaling behavior to remain approximately valid. In this sense, the resulting exclusion regions may still serve as a diagnostic benchmark for the scale at which CRDM becomes sensitive to loop-suppressed elastic interactions in strongly interacting dark sectors. While this issue was mitigated by defining $|\mathcal{M}_{2 \rightarrow 3}|^2$ as a phase-space average of the UV-completed matrix element, this does not capture non-analytic contributions such as large logarithms. However, since our analysis typically probes GeV-scale kinematics, such logarithmic terms appear as factors like $\ln(\text{GeV}^2/\text{MeV}^2)$, potentially introducing $\mathcal{O}(10)$ corrections to all observables derived from $2 \rightarrow 3$ scattering.

Additionally, there is a clear case of unitarity violation in (4.55), as $|\mathcal{M}_{\chi\psi \rightarrow \chi\psi}^{2\text{-loop}}|^2 \propto T_\psi$. This behavior is expected from effective operators, and could in principle be regulated by imposing an upper bound $T_\psi < \Lambda$. However, for values of Λ comparable to the typical energy scale of experiments like Borexino and MiniBooNE, such a restriction would eliminate all detectable events. Moreover, as discussed, the CM energies involved are significantly larger than the recoil energies. For these reasons, an artificial cutoff was not implemented, as it would not resolve the underlying issue in a consistent manner.

Taken together, these observations suggest that a proper assessment of Co-SIMPs requires embedding all interactions in a complete theory. A recent follow-up to the Co-SIMP proposal investigates such a UV completion for a scalar-mediated nucleophilic interaction [59]. Translating their results to the CRDM framework is beyond the scope of this thesis, but it is expected that the precise limits will shift depending on the UV details.

D_{eff} and the Leptophilic Scenario

As noted in Section 4.2, the behavior of the effective distance D_{eff} in non-elastic processes is not well understood. While its determination is certainly more involved in the inelastic case, we do not expect its qualitative features to differ significantly, anticipating only $\mathcal{O}(1)$ corrections to the chosen value $D_{\text{eff}} = 5 \text{ kpc}$. Even so, the present results are not reliant on the exact value of this parameter, and more conservative estimates do not affect our conclusions. Thus, we consider a more detailed analysis of this behavior to be unwarranted in light of its limited impact on our conclusions.

Finally, we briefly comment on the leptophilic scenario. Since heavy cosmic rays have negligible impact on the Co-SIMP CRDM flux, light species dominate—protons and electrons in the nucleophilic and leptophilic case, respectively. Since the electron ICR flux peaks at relativistic energies, the threshold condition $T_\psi^{\min} > m_\psi$ is less restrictive for electrons. This potentially enhances the leptophilic CRDM flux at low m_χ , though such low-mass Co-SIMPs are more likely to be attenuated by the $2 \rightarrow 3$ process. If sufficiently large, it may still be probed via elevated background rates in extraterrestrial detectors. As this work focuses on the nucleophilic case, a detailed analysis of the leptophilic scenario is left for future work.

Summary

While the framework developed here may capture the dominant physical effects in a consistent model, several limitations remain. These include the breakdown of the effective theory at high energies, the absence of a full treatment of inelastic attenuation, and sensitivity to UV completions. Nevertheless, the analysis provides a diagnostic tool for when CRDM becomes sensitive to strongly interacting dark sectors, and a basis for more refined future work.

Chapter 6

Conclusion

This thesis explored whether co-scattering strongly interacting massive particles (Co-SIMPs) can be probed using the mechanism of cosmic-ray-boosted dark matter (CRDM). Motivated by the unique thermal history of Co-SIMPs—in which the relic abundance is set by a $\chi\chi\psi \rightarrow \chi\psi$ annihilation process—this study examined whether high-energy cosmic rays can upscatter such particles into detectable fluxes reaching underground detectors.

To construct viable models, we imposed a perturbative unitarity bound and extended the standard CRDM framework to account for inelastic $2 \rightarrow 3$ scattering, as naturally arises in Co-SIMP scenarios. The resulting relativistic flux was derived using a phase-space average of the matrix element, and the corresponding recoil spectra were computed using a modified version of `DarkSUSY`.

In contrast to earlier elastic CRDM studies, our inelastic analysis reveals several qualitative differences. For $m_\chi/m_p \gtrsim 0.1$, the low-energy flux is suppressed by form factors, as certain phase space configurations allow a combination of low outgoing CRDM energy and large momentum transfer. The kinematics of $2 \rightarrow 3$ upscattering introduced a production threshold and reduced phase space at low outgoing energies in the cosmic frame, further diminishing the flux. Finally, heavy cosmic-ray species—which can enhance elastic CRDM signals—contribute negligibly here due to their more restrictive kinematic thresholds. Together, these effects make strongly interacting inelastic scenarios qualitatively harder to probe than previously studied elastic cases.

The unitarity constraint alone excludes a substantial portion of the nucleophilic parameter space compatible with thermal freeze-out, even without invoking direct detection limits. However, for tree-level $2 \rightarrow 3$ interactions, the large cross sections required to obtain the observed relic abundance imply rapid energy loss in the atmosphere and crust, rendering terrestrial detectors effectively blind to the pure Co-SIMP scenario. We considered the use of extraterrestrial detectors, but found that the CRDM flux levels required to not be buried under large astrophysical backgrounds would be in conflict with unitarity.

However, when a subdominant loop-induced elastic channel is included, provided the perturbative estimate remains valid, meaningful constraints can still be derived. In particular, nucleophilic Co-SIMPs with $m_\chi \sim [0.1, 1]$ GeV can be excluded using CRDM-induced recoils. For lower masses, our analysis yields bounds on the thermally averaged cross section $\langle\sigma_{32}v^2\rangle \gtrsim 10^{10}$ GeV $^{-5}$ in the range $m_\chi \sim [0.02, 1]$ GeV, while $m_\chi \lesssim 20$ MeV remains inaccessible due to χ requiring energies above the $2 \rightarrow 3$ kinematic threshold. Crucially, these results rely on extrapolations beyond the perturbative regime and should not be viewed as conclusive.

Altogether, we find that CRDM is unlikely to constrain strongly interacting inelastic processes directly, due to the combined effects of high energy loss, large required cross sections, and overburden attenuation. If a UV completion permits a sufficiently suppressed elastic channel, CRDM can still probe Co-SIMP masses $m_\chi \gtrsim 10$ MeV with xenon-based detectors—offering an indirect window into strongly coupled sectors otherwise hidden from conventional searches.

Outlook

Looking ahead, several avenues for future work suggest themselves. While our lower limits on the tree-level Co-SIMP–nucleon cross section are weak, the corresponding constraints on the thermally averaged annihilation cross section are comparatively strong, extending well into the $\Omega h^2 > 0.12$ region. This suggests that even subdominant elastic scattering processes may offer viable routes for terrestrial detection, as demonstrated by the two-loop analysis. To study this consistently, UV-complete Co-SIMP models with explicit mediator dynamics would allow for more accurate computation of matrix elements and kinematic distributions relevant for CRDM production and detection. While the effective field theory used here couples directly to nucleons—making collider-based constraints generally weak, especially at the sub-GeV scale—a UV-complete model would instead couple to fundamental quarks. This would induce interactions with all hadrons, including pions, and could make such models testable at low-energy, high-intensity accelerator experiments such as GeV-scale beam dumps. Accordingly, electroweak-scale collider searches are expected to yield weak constraints, while lower-energy experiments may be better suited to probing viable Co-SIMP UV completions.

While Co-SIMPs have proven difficult to probe via conventional direct detection methods, an alternative route may lie in their potential effect on the cosmic-ray energy spectrum itself. As seen, CRDM production involves energy transfer from incoming cosmic-ray protons to dark-sector particles through semi-elastic scattering processes. If such interactions occur with sufficiently large cross sections, they may lead to a measurable softening of the high-energy tail of the cosmic-ray proton spectrum. Since the interstellar CR spectrum is precisely measured, even small distortions could serve as an indirect constraint on the interaction rate. Modeling this backreaction would require solving a modified cosmic-ray transport equation with a DM-induced energy-loss term. While standard propagation tools such as GALPROP [99] or DRAGON2 [100] can provide the baseline CR spectrum, incorporating CR–DM scattering would likely require extending these frameworks or developing a dedicated numerical Boltzmann solver.

Finally, our treatment of $2 \rightarrow 3$ attenuation relied on an average energy loss estimate. While this strongly suggests that terrestrial detection of such interactions is unlikely, a more detailed modeling of attenuation—potentially incorporating deep inelastic scattering and nuclear resonances at high recoil energies—would improve the accuracy of this conclusion and may identify rare propagation windows. However, based on the energy loss estimates already obtained, we expect such an analysis would only reinforce the conclusion that attenuation prevents detection of $2 \rightarrow 3$ interactions in terrestrial detectors.

Appendix A

$2 \rightarrow 3$ Scattering

In this appendix, we review the basics of $2 \rightarrow 3$ processes relevant for probing Co-SIMPs with CRDM. In particular, we derive several results stated in Chapter 4.

A.1 Cross Section

We aim to reduce the number of integrals needed to compute $\sigma_{2 \rightarrow 3}$ while preserving the manifestly Lorentz-invariant form of (4.12). Originally, this was done using a naive approach involving non-scalar quantities. This method was abandoned in favor of the one presented below, which allows us to analyze different frames using a single expression for the cross section, without dealing with Lorentz transformations of non-scalar quantities.

Poincaré invariance implies that the problem has five independent kinematic DoF. Therefore, the differential cross section must be expressible in terms of five independent variables, without relying on physical assumptions. We follow the general procedure outlined in [96], applied to the specific $2 \rightarrow 3$ case, beginning with writing out (4.12):

$$d\sigma = \frac{1}{4F} \frac{d^3 p_3}{(2\pi)^3 2E_3} \frac{d^3 p_4}{(2\pi)^3 2E_4} \frac{d^3 p_5}{(2\pi)^3 2E_5} (2\pi)^4 \delta^4(p_1 + p_2 - p_3 - p_4 - p_5) |\mathcal{M}|^2. \quad (\text{A.1})$$

Using

$$\frac{d^3 p_5}{(2\pi)^3 2E_5} = \frac{d^4 p_5}{(2\pi)^4} \delta(p_5^2 - m_5^2) \theta(p_5^0), \quad (\text{A.2})$$

and integrating over the four components of p_5 , we obtain

$$d\sigma = \frac{1}{4F} \frac{d^3 p_3}{(2\pi)^3 2E_3} \frac{d^3 p_4}{(2\pi)^3 2E_4} (2\pi) \delta(p_5^2 - m_5^2) \theta(p_5^0) |\mathcal{M}|^2. \quad (\text{A.3})$$

Now, all momenta are now constrained by overall momentum conservation from the delta function. To compute the differential cross section in an arbitrary frame, it is convenient to express it entirely in terms of scalar quantities. As mentioned earlier, the process has five kinematical degrees of freedom, and for the final-state particles, only two of the s_{ij} and two of the t_{ij} are independent. We choose s_{45}, s_{35}, t_{13} , and t_{14} as our independent variables, introduced as follows:¹

$$\int ds_{45} \delta[s_{45} - (p_4 + p_5)^2] = 1 = \int dt_{13} \delta[t_{13} - (p_1 - p_3)^2], \quad (\text{A.4})$$

$$\int ds_{35} \delta[s_{35} - (p_3 + p_5)^2] = 1 = \int dt_{14} \delta[t_{14} - (p_1 - p_4)^2], \quad (\text{A.5})$$

¹The choice is arbitrary; Eqs. (4.2, 4.3, 4.4) in Section 4.1 can be used to eliminate one for another.

with s being the final DoF. Choosing to work in the CM frame² we can rewrite the delta functions as:

$$\delta \left[s_{45} - (p'_4 + p'_5)^2 \right] = \frac{1}{2\sqrt{s}} \delta \left[E'_3 - \frac{s + m_3^2 - s_{45}}{2\sqrt{s}} \right], \quad (\text{A.6})$$

$$\delta \left[s_{35} - (p'_3 + p'_5)^2 \right] = \frac{1}{2\sqrt{s}} \delta \left[E'_4 - \frac{s + m_4^2 - s_{35}}{2\sqrt{s}} \right], \quad (\text{A.7})$$

$$\delta \left[t_{13} - (p'_1 - p'_3)^2 \right] = \frac{1}{2|\mathbf{p}'_1||\mathbf{p}'_3|} \delta \left[\cos \theta'_{13} - \cos \tilde{\theta}'_{13} \right], \quad (\text{A.8})$$

$$\cos \tilde{\theta}'_{13} \equiv \frac{t_{13} - m_1^2 - m_3^2 + 2E'_1 E'_3}{2|\mathbf{p}'_1||\mathbf{p}'_3|}, \quad (\text{A.9})$$

$$\delta \left[t_{14} - (p'_1 - p'_4)^2 \right] = \frac{1}{2|\mathbf{p}'_1||\mathbf{p}'_4| \sin \theta'_{13} \sin \theta'_{34}} \delta \left[\cos \varphi'_4 - \cos \tilde{\varphi}'_4 \right], \quad (\text{A.10})$$

$$\cos \tilde{\varphi}'_4 \equiv \frac{t_{14} - m_1^2 - m_4^2 + 2E'_1 E'_4 - 2|\mathbf{p}'_1||\mathbf{p}'_4| \cos \theta'_{13} \cos \theta'_{34}}{2|\mathbf{p}'_1||\mathbf{p}'_4| \sin \theta'_{13} \sin \theta'_{34}}, \quad (\text{A.11})$$

where the angles are defined by:

$$\cos \theta'_{ij} \equiv \frac{\mathbf{p}'_i \cdot \mathbf{p}'_j}{|\mathbf{p}'_i||\mathbf{p}'_j|}, \quad \cos \varphi'_4 \equiv \frac{\cos \theta'_{14} - \cos \theta'_{13} \cos \theta'_{34}}{\sin \theta'_{13} \sin \theta'_{34}}. \quad (\text{A.12})$$

We begin by inserting Eqs. (A.4, A.5) into (A.3), switching to spherical coordinates in the p_3 integral, and integrating over the azimuthal angle.³ The rewritten delta functions from Eqs. (A.6–A.8) are then applied to obtain:

$$\begin{aligned} \sigma = & \frac{1}{4F} \frac{1}{16\pi\sqrt{s}|\mathbf{p}'_1|} \int ds_{45} dt_{13} ds_{35} dt_{14} \int \frac{d^3 p'_4}{(2\pi)^3 2E'_4} \delta \left[p'^2_5 - m_5^2 \right] \\ & \times |\mathcal{M}|^2 \delta \left[s_{35} - (p'_1 + p'_2 - p'_4)^2 \right] \delta \left[t_{14} - (p'_1 - p'_4)^2 \right]. \end{aligned} \quad (\text{A.13})$$

We now express the on-shell condition for p'_5 as:

$$\delta \left[p'^2_5 - m_5^2 \right] = \delta \left[(p'_1 + p'_2 - p'_3 - p'_4)^2 - m_5^2 \right] = \frac{1}{2|\mathbf{p}'_3||\mathbf{p}'_4|} \delta \left[\cos \theta'_{34} - \cos \tilde{\theta}'_{34} \right], \quad (\text{A.14})$$

$$\cos \tilde{\theta}'_{34} \equiv \frac{s - 2\sqrt{s}(E'_3 + E'_4) + 2E'_3 E'_4 + m_3^2 + m_4^2 - m_5^2}{2|\mathbf{p}'_3||\mathbf{p}'_4|}. \quad (\text{A.15})$$

We proceed similarly for the p_4 integral, using (A.7) and (A.10).

$$\begin{aligned} \sigma = & \frac{1}{4F} \frac{1}{32\pi s|\mathbf{p}'_1|^2} \int ds_{45} dt_{13} ds_{35} dt_{14} \int d\varphi'_4 \frac{|\mathbf{p}'_4|}{(2\pi)^3 2} \frac{1}{4|\mathbf{p}'_3||\mathbf{p}'_4|^2} |\mathcal{M}|^2 \\ & \times \frac{1}{|\sin \theta'_{13}||\sin \theta'_{34}|} \delta \left[\cos \varphi'_4 - \cos \tilde{\varphi}'_4 \right] \end{aligned} \quad (\text{A.16})$$

$$= \frac{1}{4F} \frac{1}{4(4\pi)^4 s |\mathbf{p}'_1|^2} \int \frac{ds_{45} dt_{13} ds_{35} dt_{14}}{|\sin \theta'_{13}||\sin \theta'_{34}||\sin \varphi'_4|} \frac{|\mathcal{M}|^2}{|\mathbf{p}'_3||\mathbf{p}'_4|}. \quad (\text{A.17})$$

²We refer to all non-Lorentz invariant (including covariant) quantities in the CM frame with a prime.

³Technically, this step involves integrating over the azimuthal angle. However, since the total three-momentum vanishes in the CM frame, the outgoing particles lie in a single plane, making the kinematics azimuthally symmetric. Moreover, the matrix element depends only on scalar invariants constructed from the momenta and masses, all of which are independent of the azimuthal angle. Thus, no additional physical assumption is introduced in this step. The same applies to the analogous step performed later.

where we redefined $\tilde{\theta}_{ij}$ and $\tilde{\varphi}_4$ as θ_{ij} and φ_4 , respectively. Note that the absolute values appear due to the identity $\delta(g(x)) = \delta(x)/|g'(x)|$. The energies in the CM frame can be expressed in terms of the kinematical invariants:

$$E'_1 = \frac{s + m_1^2 - m_2^2}{2\sqrt{s}}, \quad E'_3 = \frac{s + m_3^2 - s_{45}}{2\sqrt{s}}, \quad E'_4 = \frac{s + m_4^2 - s_{35}}{2\sqrt{s}}. \quad (\text{A.18})$$

Using $E^2 = m^2 + \mathbf{p}^2$, a direct calculation shows that the momenta can be written as:

$$|\mathbf{p}'_1| = \frac{\sqrt{\lambda(s, m_1^2, m_2^2)}}{2\sqrt{s}}, \quad |\mathbf{p}'_3| = \frac{\sqrt{\lambda(s, s_{45}, m_3^2)}}{2\sqrt{s}}, \quad |\mathbf{p}'_4| = \frac{\sqrt{\lambda(s, s_{35}, m_4^2)}}{2\sqrt{s}}. \quad (\text{A.19})$$

Substituting these expressions into (A.17) and simplifying yields the final result:

$$\sigma = \frac{1}{4F} \frac{4}{(4\pi)^4} \frac{s}{\lambda(s, m_1^2, m_2^2)} \int \frac{ds_{45} dt_{13} ds_{35} dt_{14}}{|\sin \theta'_{13} \sin \theta'_{34} \sin \varphi'_4|} \frac{|\mathcal{M}|^2}{\sqrt{\lambda(s, s_{45}, m_3^2) \lambda(s, s_{35}, m_4^2)}}. \quad (\text{A.20})$$

Since the energies and momenta in the CM frame are fully determined by scalar invariants, all angular variables can likewise be expressed in terms of them. Thus, the result in (A.20) depends exclusively on scalar quantities. Rewriting the full phase space confirms that this expression is consistent with the initial claim of this section. The integration limits follow directly from solving the arguments of the delta functions in Eqs. (A.6–A.10). Substituting Eqs. (A.18, A.19) yields the integration limits given in Eqs. (4.17–4.22).

A.2 CM Angles

The relevant CM angles can also be expressed in terms of generalized Mandelstam variables. When performing the integrals numerically—which is necessary when including form factors in the CF in (4.34)—the angles are implemented as follows:

$$\cos \theta'_{1i} = \frac{m_i^2(m_i^2 - s - s_{jk}) - m_2^2(m_i^2 + s - s_{jk}) + s(s + 2t_{1i} - s_{jk} - m_i^2)}{\sqrt{\lambda(s, m_1^2, m_2^2) \lambda(s, s_{jk}, m_i^2)}}, \quad (\text{A.21})$$

$$\cos \theta'_{34} = \frac{s(m_3^2 + m_4^2 - 2m_5^2 + s_{35} + s_{45}) + s_{35}s_{45} + m_3^2m_4^2 - m_3^2s_{35} - m_4^2s_{45}}{\sqrt{\lambda(s, s_{45}, m_3^2) \lambda(s, s_{35}, m_4^2)}}, \quad (\text{A.22})$$

$$\cos \varphi'_4 = \frac{t_{14}\lambda(s, s_{45}, m_\chi^2) - A}{2\sqrt{BC}}, \quad (\text{A.23})$$

where $i, j, k \in \{3, 4, 5\}$, $i \neq j \neq k$ and

$$\begin{aligned} A &\equiv m_\psi^2(m_\chi^2(s + s_{35}) - 3m_\chi^4 - s(s_{35} + s_{45} + 2t_{13}) + s_{45}(s_{35} + s_{45})) \\ &+ m_\psi^4(m_\chi^2 + s - s_{45}) + 2m_\chi^6 + m_\chi^4(s_{35} - 5s - s_{45} + t_{13}) \\ &+ m_\chi^2(4s^2 - s(2s_{35} + 3s_{45} - 2t_{13}) - t_{13}(s_{35} + s_{45}) + s_{45}(s_{45} - 3s_{35})) \\ &- t_{13}(s^2 - s(s_{35} + s_{45}) - s_{35}s_{45}) - s(s - s_{45})(s - s_{35} - s_{45}), \end{aligned} \quad (\text{A.24})$$

$$B \equiv t_{13}(m_\psi^2(m_\chi^2 + s - s_{45}) + s_{45}(m_\chi^2 + s) - (m_\chi^2 - s)^2) - m_\chi^2(m_\psi^2 - s_{45})^2 - st_{13}^2, \quad (\text{A.25})$$

$$\begin{aligned} C &\equiv m_\psi^2(m_\chi^4 + m_\chi^2(2s - s_{35} - s_{45}) - s^2 + s(s_{35} + s_{45}) + s_{35}s_{45}) - m_\psi^4s - 2m_\chi^6 \\ &+ m_\chi^4(s + s_{35} + s_{45}) - m_\chi^2(s(s_{35} + s_{45}) - 2s_{35}s_{45}) + s_{35}s_{45}(s - s_{35} - s_{45}). \end{aligned} \quad (\text{A.26})$$

The remaining angles can be obtained from momentum conservation. Note that the $\cos \varphi'_4$ expression is not general; it only applies when particles 1, 3, 4 and 2, 5 have masses m_χ and m_ψ , respectively. This is why we labeled $N(p_2)$ explicitly in Section 4.5, even though the rest of the thesis typically places particle 1 at rest. Although not immediately evident from the expressions, numerical evaluation confirms that $\cos \theta'_{2i} = -\cos \theta'_{1i}$, as expected from symmetry.

A.3 Analytical Simplification of Differential Cross Section

To arrive at (4.25) and (4.26) in the main text, we begin from the result in (A.17), assuming $\overline{|\mathcal{M}|^2} = C/s$, where C is a dimensionless constant and s is the CM energy squared. Using the variable dependencies in (A.21–A.23) allow us to rewrite (A.20) as:

$$\sigma(s) = \frac{1}{4F} \frac{4}{(4\pi)^4} \frac{s}{\lambda(s, m_1^2, m_2^2)} \int_{s_{45}^-}^{s_{45}^+} \frac{ds_{45}}{\sqrt{\lambda(s, s_{45}, m_3^2)}} \int_{t_{13}^-}^{t_{13}^+} \frac{dt_{13}}{|\sin \theta'_{13}|} \\ \times \int_{s_{35}^-}^{s_{35}^+} \frac{ds_{35}}{|\sin \theta'_{34}|} \left[\sqrt{\lambda(s, s_{35}, m_4^2)} \right]^{-1} \int_{t_{14}^-}^{t_{14}^+} dt_{14} \frac{\overline{|\mathcal{M}|^2}}{|\sin \varphi'_4|}. \quad (\text{A.27})$$

As mentioned, this result is frame independent. As such, we can apply it in any frame. Starting with the CM frame, assuming the point-like interaction limit, three of the integrals can be performed analytically, as the first integral cancels several of the kinematic factors. To illustrate this cancellation, we rewrite the expression for $\cos \varphi'_4$ from (A.11) as:

$$\cos \varphi'_4 \equiv w \equiv \frac{t_{14} + b}{a}, \quad (\text{A.28})$$

where

$$a \equiv 2|\mathbf{p}'_1||\mathbf{p}'_4| \sin \theta'_{13} \sin \theta'_{34}, \quad (\text{A.29})$$

$$b \equiv -m_1^2 - m_4^2 + 2E'_1 E'_4 - 2|\mathbf{p}'_1||\mathbf{p}'_4| \cos \theta'_{13} \cos \theta'_{34}. \quad (\text{A.30})$$

A direct evaluation confirms that $w(t_{14}^\pm) = \pm 1$, as expected. The t_{14} integral then reduces to a standard angular integral:

$$\int_{t_{14}^-}^{t_{14}^+} dt_{14} \frac{\overline{|\mathcal{M}|^2}}{|\sin \varphi'_4|} = \overline{|\mathcal{M}|^2} \int_{-1}^1 \frac{a dw}{\sqrt{1-w^2}} = 2\pi |\mathbf{p}'_1||\mathbf{p}'_4| \sin \theta'_{13} \sin \theta'_{34} \overline{|\mathcal{M}|^2}. \quad (\text{A.31})$$

Inserting this into (A.27) we obtain:⁴

$$\begin{aligned}\sigma(s) &= \frac{1}{4F} \frac{4}{(4\pi)^4} \frac{s}{\lambda(s, m_1^2, m_2^2)} \int_{s_{45}^-}^{s_{45}^+} \frac{ds_{45}}{\sqrt{\lambda(s, s_{45}, m_3^2)}} \int_{t_{13}^-}^{t_{13}^+} \frac{dt_{13}}{\sin \theta'_{13}} \\ &\quad \times \int_{s_{35}^-}^{s_{35}^+} \frac{ds_{35}}{\sqrt{\lambda(s, s_{35}, m_4^2)}} \frac{2\pi |\mathbf{p}'_1| |\mathbf{p}'_4| \sin \theta'_{13} \sin \theta'_{34}}{\sin \theta'_{34}} \overline{|\mathcal{M}|^2} \end{aligned} \quad (\text{A.32})$$

$$= \frac{1}{4F} \frac{2\pi}{(4\pi)^4} \frac{1}{\sqrt{\lambda(s, m_1^2, m_2^2)}} \int_{s_{45}^-}^{s_{45}^+} \frac{ds_{45}}{\sqrt{\lambda(s, s_{45}, m_3^2)}} \int_{t_{13}^-}^{t_{13}^+} dt_{13} \int_{s_{35}^-}^{s_{35}^+} ds_{35} \overline{|\mathcal{M}|^2} \quad (\text{A.33})$$

$$= \frac{1}{4F} \frac{1}{2(4\pi)^3} \frac{1}{s} \int_{s_{45}^-}^{s_{45}^+} \frac{ds_{45}}{s_{45}} \sqrt{\lambda(s, s_{45}, m_3^2) \lambda(s_{45}, m_4^2, m_5^2)} \overline{|\mathcal{M}|^2}, \quad (\text{A.34})$$

where we have used expressions from Section A.1, along with the integration limits given in (4.17–4.20). Using the relation between E'_3 and s_{45} from (A.18), we obtain the differential cross section in the CM frame:

$$\frac{d\sigma}{dE'_3} = \frac{1}{4F} \frac{1}{(4\pi)^3} \frac{\overline{|\mathcal{M}|^2}}{s_{45} \sqrt{s}} \sqrt{\lambda(s, s_{45}, m_3^2) \lambda(s_{45}, m_4^2, m_5^2)}. \quad (\text{A.35})$$

However, in our case, we are interested in the corresponding expression in the lab (CF) frame, i.e., where particle 1 is at rest. Since t_{13} is directly related to E_3 , it is most convenient to perform the t_{13} integral last. We therefore return to (A.33), change the order of integration with the updated limits, and perform the s_{35} integral to obtain:

$$d\sigma = \frac{1}{4F} \frac{1}{2(4\pi)^3} \frac{dt_{13}}{\sqrt{\lambda(s, m_1^2, m_2^2)}} \int_{s_{45}^-}^{s_{45}^+} \frac{ds_{45}}{s_{45}} \sqrt{\lambda(s_{45}, m_4^2, m_5^2)} \overline{|\mathcal{M}|^2}, \quad (\text{A.36})$$

$$\frac{d\sigma}{dE_3} = \frac{1}{2} \frac{1}{4F} \frac{m_1}{(4\pi)^3} \frac{1}{\sqrt{\lambda(s, m_1^2, m_2^2)}} \int_{s_{45}^-}^{s_{45}^+} \frac{ds_{45}}{s_{45}} \sqrt{\lambda(s_{45}, m_4^2, m_5^2)} \overline{|\mathcal{M}|^2}. \quad (\text{A.37})$$

Here, we have used the corresponding integration limits appropriate for the lab frame. This completes the derivation of the results stated in the main text.

⁴There are sign ambiguities in this calculation; however, the full differential cross section must be non-negative in the kinematically allowed region. We therefore disregard these signs here. This is only problematic when $m_1 \neq m_3$ or $m_1 \neq m_4$, as t_{13} and t_{14} can then switch signs. For our purposes, this never occurs.

Appendix B

Implementation in DarkSUSY

This appendix documents the numerical implementation of the Co-SIMP scenario within the `DarkSUSY` framework [6] which can be found on GitHub.¹ It focuses exclusively on components not already described in existing literature, in particular the original `DarkSUSY` documentation [6] and the CRDM modules introduced in [4, 7]. All generic functionality, common interface routines, and unmodified modules are assumed to be understood from those references. The content below details only the new algorithms, modified functions, and parameter handling introduced to support the results in Chapter 4.

Cross Section Normalization and Inversion

For elastic $2 \rightarrow 2$ scattering, the non-relativistic cross section is set by $\sigma_{\text{NR}} \equiv (\text{sin} + \text{sip})/2$, where `sin` (`sip`) is the spin-independent cross section for neutrons (protons). In the $2 \rightarrow 3$ case, this quantity has no simple physical interpretation and is used to fix the matrix element normalization,

$$\frac{\text{sin} + \text{sip}}{2} = C, \quad (\text{B.1})$$

with $\overline{|\mathcal{M}|^2} = C/s$.²

When including the two-loop elastic interaction in Fig. 4.13, we compute the non-relativistic cross section by integrating Eq. (4.59) with $G_\psi = 1$, dividing by T_ψ^{\max} from Eq. (3.28), and taking the $T_\psi \rightarrow 0$ limit:

$$\sigma_{\text{NR}} = \frac{c_\psi^2}{4\pi} \left(\frac{m_\psi}{m_\chi + m_\psi} \right)^2. \quad (\text{B.2})$$

The coherent enhancement factor is excluded, as it cancels when matching rates to experimental limits. The relativistic correction is then included as

$$\frac{d\sigma_{\chi\psi \rightarrow \chi\psi}}{dT_\psi} = \frac{\sigma_{\text{NR}}}{T_\psi^{\max}} A_\psi^2 G_\psi^2 (2m_\psi T_\psi) \cdot \frac{1}{s} (m_\chi + m_\psi)^2 \left[1 + \frac{Q^2}{4m_\psi^2} \right]. \quad (\text{B.3})$$

To set the corresponding normalization C for the $2 \rightarrow 3$ matrix element, we use Eqs. (4.44, 4.54, 4.57) and invert

$$c_\psi = 2\sqrt{\pi\sigma_{\text{NR}}} \left[\frac{m_\chi}{m_\psi} + 1 \right]. \quad (\text{B.4})$$

¹https://github.com/EdvardRornes/CoSIMP_CRDM

²There is an additional option which sets $\overline{|\mathcal{M}|^2} = C$. In this case, $(\text{sin} + \text{sip})/2 = \overline{|\mathcal{M}|^2}$.

This expression is not analytically invertible for C , so a numerical bisection method is used to match a given σ_{NR} to its corresponding C . With this mapping, we impose

$$\Gamma_N^{\text{2-loop}} = \Gamma_N^{\text{DM}}, \quad (\text{B.5})$$

to determine the lower or upper limit on σ_{NR} .

Program Structure

All programs follow the prefix `DDCR_` (Direct Detection Cosmic Ray). They rely on functions stored in `my_replaceable`:

- `DDCR_CRflux.f`: Computes the tabulated ICR flux for $\psi \in \{p, \text{He}, \text{C}, \text{O}\}$. Units: $[\text{cm}^{-2} \text{s}^{-1} \text{GeV}^{-1}]$.
- `DDCR_flux.f`: Computes the $2 \rightarrow 3$ Co-SIMP CRDM flux in (4.27). Units: $[\text{cm}^{-2} \text{s}^{-1} \text{GeV}^{-1}]$.
- `DDCR_target_recoil.f`: Computes the recoil spectrum for target mass m_N in (4.35). Units: $[\text{s}^{-1} \text{GeV}^{-1}]$.
- `DDCR_sigtot.f`: Computes the integrated $2 \rightarrow 3$ cross section in (4.15). Units: $[\text{cm}^2]$.
- `DDCR_countrate.f`: Computes $\Gamma_{\text{Co-SIMP}}^{\text{CRDM}} / \Gamma_N^{\text{DM}}$. Units: [None].
- `DDCR_limits.f`: Finds the value of σ_{NR} (and C) such that $\Gamma_N^{\text{2-loop}} = \Gamma_N^{\text{DM}}$. Units: varies; typically $[\text{cm}^2]$ or [None], depending on options.
- `DDCR_limits2.f`: Optimized version for $2 \rightarrow 3$ limits assuming attenuation is neglected. Units: varies; typically $[\text{cm}^2]$ or [None], depending on options.
- `DDCR_EnergyLoss.f`: Computes average energy loss for $\chi O \rightarrow \chi \chi O$ in (4.45). Units: [GeV].
- `DDCR_EnergyLoss2t2.f`: Same as above but for $2 \rightarrow 2$ elastic scattering. Only relevant with form factors or t -dependent $|\mathcal{M}|^2$, otherwise (4.48) is exact. Units: [GeV].

Options

The file `dsddcrdm_init.f` defines the following user options:

- `CRDM_form_factor`: Enables form factors $G(Q^2)$ if `.true.`.
- `CRDM_cs`: Sets $|\mathcal{M}|^2 = C/s$ if `.true.`, else $|\mathcal{M}|^2 = C$ (the latter violates unitarity at high energies).
- `CRDM_high_acc`: Enables high-accuracy integration (slower).
- `CRDM_tab`: Uses tabulated $2 \rightarrow 3$ CRDM flux.
- `CRDM_2loop`: Uses 2-loop differential cross section in the detector.
- `CRDM_EnergyLoss`: Auxiliary flag for energy loss integrals (do not change).

- **CRDM_attenuation**: Enables full attenuation modeling. (this was always on by default previously)
- **CRDM_both**: Adds 2-loop elastic contribution to CRDM flux.

The header file `dsddcom.h` is modified to support the above changes (NB: this requires changing the corresponding `dsddcom.h` in the DarkSUSY directory!). Default D_{eff} was set to 5 kpc. Note that additional options exist from the work in [7].

While the core combinations of settings used to produce the physical results in this thesis have been thoroughly tested, not all possible configurations of user options have been validated. We advise to verify consistency on a case-by-case basis when modifying multiple options simultaneously.

Function Overview

Below is a list of new or modified functions. For brevity, routine wrappers or unchanged copies from DarkSUSY are grouped.

Modified or new functions:

- `dsddDMCRdgammadt.f`: Compute $d\Gamma/dT_N$ for the $2 \rightarrow 3$ or $2 \rightarrow 2$ channels, given in (4.35) and (4.50), respectively. Units: [$\text{s}^{-1} \text{GeV}^{-1}$].
- `dsddDMCREnergyLoss.f`: Computes $\langle \omega^\chi \rangle \sigma$ for $2 \rightarrow 3$ or returns total σ . Units: [$\text{cm}^2 \text{GeV}$] or [cm^2].
- `dsddDMCREnergyLoss2t2.f`: Computes $\langle \omega^\chi \rangle$ for $2 \rightarrow 2$. Units: [GeV].
- `dsddDMCRflux.f`, `dsddDMCRflux_2loop.f`: Computes $d\Phi_\chi/dT_\chi$ for $2 \rightarrow 3$ and $2 \rightarrow 2$, see (4.27). Units: [$\text{cm}^{-2} \text{s}^{-1} \text{GeV}^{-1}$].
- `dsddDMCRRflux_Tab.f`: Interpolates tabulated $2 \rightarrow 3$ CRDM flux for $m_\chi \in [10^{-4}, 10] \text{ GeV}$ and $T_\chi \in [10^{-4}, 10^6] \text{ GeV}$. Allows extrapolation of T_χ . Units: [$\text{cm}^{-2} \text{s}^{-1} \text{GeV}^{-1}$].
- `dsddDMCRinvertcpsi.f`: Inverts σ^{NR} to determine the normalization C . Units: [None].
- `dsddDMCRsigCR_2loop.f`: Computes the differential cross section for the 2-loop process, see (4.59). Units: [$\text{cm}^2 \text{GeV}^{-1}$].
- `dsddDMCRsigCR.f`: Computes the simplified $2 \rightarrow 3$ differential cross section with $G(Q^2) = 1$, see (4.26). Units: [$\text{cm}^2 \text{GeV}^{-1}$].
- `dsddDMCRsigCRff.f`: Computes the form factor suppressed $2 \rightarrow 3$ differential cross section $d\sigma/dT_\chi$, see (4.34). Units: [$\text{cm}^2 \text{GeV}^{-1}$].
- `dsddDMCRsigCRs35int.f`, `dsddDMCRsigCRT14int.f`: Sub-integrals for s_{35} and t_{14} in (4.34). Units: [None] and [None].
- `dsddDMCRsigtarget_2loop.f`: Computes the nuclear $2 \rightarrow 2$ differential cross section, see (4.59). Units: [$\text{cm}^2 \text{GeV}^{-1}$].
- `dsddDMCRsigtarget_2loop.f`: Computes the nuclear $2 \rightarrow 3$ differential cross section, see (4.37). Units: [$\text{cm}^2 \text{GeV}^{-1}$].

-
- `dsddDMCRsigtot_2loop.f`: Computes the integrated 2-loop cross section σ . Units: [cm²].
 - `dsddDMCRsigtot.f`: Computes the integrated $2 \rightarrow 3$ cross section σ , see (4.15). Note: This integrates over `dsddDMCRsigtot.f`. `dsddDMCREnergyLoss.f` is the only function which computes the full integral numerically. Units: [cm²].

Minor changes:

- `dsddDMCRsigsoil.f`, `dsddTDMattenuation.f`, `dsddDMCRcountrate.f`: No or minor changes.
- `dsddlfreeSim.f`: Fixed typo in `how.eq.2` for-loop.
- `dsddsigmarel.f`: Updated relativistic correction to $\sigma_{\text{NR}}/T_\psi^{\max}$, see (B.3).

Summary

This implementation enabled a fully relativistic computation of the $2 \rightarrow 3$ CRDM flux, recoil spectra, and elastic 2-loop limits, all with support for attenuation and form factor suppression. The connection between σ_{NR} and the phase-space-averaged matrix element $|\mathcal{M}|^2$ was handled dynamically, and results were benchmarked against known limits. The infrastructure supports all numerical results in Chapter 4. Note: Only core configurations used in this thesis were validated; caution is advised when enabling additional combinations of toggles.

Bibliography

- [1] F. Zwicky. “Die Rotverschiebung von extragalaktischen Nebeln.” In: *Helv. Phys. Acta* 6 (1933), pp. 110–127. DOI: [10.1007/s10714-008-0707-4](https://doi.org/10.1007/s10714-008-0707-4).
- [2] Jaco de Swart. “Five decades of missing matter.” In: *Physics Today* 77.8 (Aug. 2024), pp. 34–43. ISSN: 0031-9228. DOI: [10.1063/pt.ozhk.lfeb](https://doi.org/10.1063/pt.ozhk.lfeb). eprint: https://pubs.aip.org/physicstoday/article-pdf/77/8/34/20082503/34_1_pt.ozhk.lfeb.pdf. URL: <https://doi.org/10.1063/pt.ozhk.lfeb>.
- [3] N. Aghanim et al. “Planck 2018 results. VI. Cosmological parameters.” In: *Astron. Astrophys.* 641 (2020). [Erratum: *Astron. Astrophys.* 652, C4 (2021)], A6. DOI: [10.1051/0004-6361/201833910](https://doi.org/10.1051/0004-6361/201833910). arXiv: [1807.06209](https://arxiv.org/abs/1807.06209) [[astro-ph.CO](#)].
- [4] Torsten Bringmann and Maxim Pospelov. “Novel direct detection constraints on light dark matter.” In: *Phys. Rev. Lett.* 122.17 (2019), p. 171801. DOI: [10.1103/PhysRevLett.122.171801](https://doi.org/10.1103/PhysRevLett.122.171801). arXiv: [1810.10543](https://arxiv.org/abs/1810.10543) [[hep-ph](#)].
- [5] Juri Smirnov and John F. Beacom. “New Freezeout Mechanism for Strongly Interacting Dark Matter.” In: *Physical Review Letters* 125.13 (Sept. 2020). ISSN: 1079-7114. DOI: [10.1103/physrevlett.125.131301](https://doi.org/10.1103/physrevlett.125.131301). URL: <http://dx.doi.org/10.1103/PhysRevLett.125.131301>.
- [6] Torsten Bringmann et al. “DarkSUSY 6 : An Advanced Tool to Compute Dark Matter Properties Numerically.” In: *JCAP* 07 (2018), p. 033. DOI: [10.1088/1475-7516/2018/07/033](https://doi.org/10.1088/1475-7516/2018/07/033). arXiv: [1802.03399](https://arxiv.org/abs/1802.03399) [[hep-ph](#)].
- [7] James Alvey, Torsten Bringmann, and Helena Kolesova. “No room to hide: implications of cosmic-ray upscattering for GeV-scale dark matter.” In: *JHEP* 01 (2023), p. 123. DOI: [10.1007/JHEP01\(2023\)123](https://doi.org/10.1007/JHEP01(2023)123). arXiv: [2209.03360](https://arxiv.org/abs/2209.03360) [[hep-ph](#)].
- [8] Csaba Balazs et al. “A Primer on Dark Matter.” In: (Nov. 2024). arXiv: [2411.05062](https://arxiv.org/abs/2411.05062) [[astro-ph.CO](#)].
- [9] Paolo Salucci. “The distribution of dark matter in galaxies.” In: *Astron. Astrophys. Rev.* 27.1 (2019), p. 2. DOI: [10.1007/s00159-018-0113-1](https://doi.org/10.1007/s00159-018-0113-1). arXiv: [1811.08843](https://arxiv.org/abs/1811.08843) [[astro-ph.GA](#)].
- [10] Richard Massey, Thomas Kitching, and Johan Richard. “The dark matter of gravitational lensing.” In: *Rept. Prog. Phys.* 73 (2010), p. 086901. DOI: [10.1088/0034-4885/73/8/086901](https://doi.org/10.1088/0034-4885/73/8/086901). arXiv: [1001.1739](https://arxiv.org/abs/1001.1739) [[astro-ph.CO](#)].
- [11] Jean-Michel Alimi and Remy Koskas. “The shape of dark matter halos: A new fundamental cosmological invariance.” In: *Astron. Astrophys.* 691 (2024), A10. DOI: [10.1051/0004-6361/202450845](https://doi.org/10.1051/0004-6361/202450845). arXiv: [2406.15947](https://arxiv.org/abs/2406.15947) [[astro-ph.CO](#)].

- [12] Michael Kuhlen, Mark Vogelsberger, and Raul Angulo. “Numerical Simulations of the Dark Universe: State of the Art and the Next Decade.” In: *Phys. Dark Univ.* 1 (2012), pp. 50–93. DOI: [10.1016/j.dark.2012.10.002](https://doi.org/10.1016/j.dark.2012.10.002). arXiv: [1209.5745 \[astro-ph.CO\]](https://arxiv.org/abs/1209.5745).
- [13] Chiaki Hanyu and Asao Habe. “The differential energy distribution of the universal density profile of dark halo.” In: *Astrophys. J.* 554 (2001), p. 1268. DOI: [10.1086/321389](https://doi.org/10.1086/321389). arXiv: [astro-ph/0011004](https://arxiv.org/abs/astro-ph/0011004).
- [14] P. Cataldi et al. “Baryons shaping dark matter haloes.” In: *Mon. Not. Roy. Astron. Soc.* 501.4 (2021), pp. 5679–5691. DOI: [10.1093/mnras/staa3988](https://doi.org/10.1093/mnras/staa3988). arXiv: [2008.02404 \[astro-ph.GA\]](https://arxiv.org/abs/2008.02404).
- [15] Jan Novotný, Zdeněk Stuchlík, and Jan Hladík. “Polytropic spheres modelling dark matter haloes of dwarf galaxies.” In: *Astron. Astrophys.* 647 (2021), A29. DOI: [10.1051/0004-6361/202039338](https://doi.org/10.1051/0004-6361/202039338). arXiv: [2101.00891 \[astro-ph.CO\]](https://arxiv.org/abs/2101.00891).
- [16] Raul E. Angulo and Oliver Hahn. “Large-scale dark matter simulations.” In: *Liv. Rev. Comput. Astrophys.* 8.1 (2022), p. 1. DOI: [10.1007/s41115-021-00013-z](https://doi.org/10.1007/s41115-021-00013-z). arXiv: [2112.05165 \[astro-ph.CO\]](https://arxiv.org/abs/2112.05165).
- [17] Aaron A. Dutton and Andrea V. Macciò. “Cold dark matter haloes in the Planck era: evolution of structural parameters for Einasto and NFW profiles.” In: *Mon. Not. Roy. Astron. Soc.* 441.4 (2014), pp. 3359–3374. DOI: [10.1093/mnras/stu742](https://doi.org/10.1093/mnras/stu742). arXiv: [1402.7073 \[astro-ph.CO\]](https://arxiv.org/abs/1402.7073).
- [18] Aaron D. Ludlow et al. “The Mass Profile and Accretion History of Cold Dark Matter Halos.” In: *Mon. Not. Roy. Astron. Soc.* 432 (2013), p. 1103. DOI: [10.1093/mnras/stt526](https://doi.org/10.1093/mnras/stt526). arXiv: [1302.0288 \[astro-ph.CO\]](https://arxiv.org/abs/1302.0288).
- [19] P.F. de Salas et al. “On the estimation of the local dark matter density using the rotation curve of the Milky Way.” In: *Journal of Cosmology and Astroparticle Physics* 2019.10 (Oct. 2019), pp. 037037. ISSN: 1475-7516. DOI: [10.1088/1475-7516/2019/10/037](https://doi.org/10.1088/1475-7516/2019/10/037). URL: <http://dx.doi.org/10.1088/1475-7516/2019/10/037>.
- [20] J. I. Read. “The Local Dark Matter Density.” In: *J. Phys. G* 41 (2014), p. 063101. DOI: [10.1088/0954-3899/41/6/063101](https://doi.org/10.1088/0954-3899/41/6/063101). arXiv: [1404.1938 \[astro-ph.GA\]](https://arxiv.org/abs/1404.1938).
- [21] Manuel Drees and Zhongyi Zhang. “LHC constraints on a mediator coupled to heavy quarks.” In: *Phys. Lett. B* 797 (2019), p. 134832. DOI: [10.1016/j.physletb.2019.134832](https://doi.org/10.1016/j.physletb.2019.134832). arXiv: [1903.00496 \[hep-ph\]](https://arxiv.org/abs/1903.00496).
- [22] “High-Luminosity Large Hadron Collider (HL-LHC) : Preliminary Design Report.” In: (Dec. 2015). Ed. by G Apolinari et al. DOI: [10.5170/CERN-2015-005](https://doi.org/10.5170/CERN-2015-005).
- [23] Jennifer M. Gaskins. “A review of indirect searches for particle dark matter.” In: *Contemp. Phys.* 57.4 (2016), pp. 496–525. DOI: [10.1080/00107514.2016.1175160](https://doi.org/10.1080/00107514.2016.1175160). arXiv: [1604.00014 \[astro-ph.HE\]](https://arxiv.org/abs/1604.00014).
- [24] Kimberly K. Boddy et al. “New dark matter analysis of milky way dwarf satellite galaxies with madhatv2.” In: *Phys. Rev. D* 109.10 (2024), p. 103007. DOI: [10.1103/PhysRevD.109.103007](https://doi.org/10.1103/PhysRevD.109.103007). arXiv: [2401.05327 \[hep-ph\]](https://arxiv.org/abs/2401.05327).
- [25] Christoph Tönnis. “Searches for Dark Matter in the Sun with the IceCube Neutrino Telescope.” In: *Phys. Sci. Forum* 8.1 (2023), p. 26. DOI: [10.3390/psf2023008026](https://doi.org/10.3390/psf2023008026).
- [26] K. Abe et al. “Indirect search for dark matter from the Galactic Center and halo with the Super-Kamiokande detector.” In: *Phys. Rev. D* 102.7 (2020), p. 072002. DOI: [10.1103/PhysRevD.102.072002](https://doi.org/10.1103/PhysRevD.102.072002). arXiv: [2005.05109 \[hep-ex\]](https://arxiv.org/abs/2005.05109).

- [27] J. D. Lewin and P. F. Smith. “Review of mathematics, numerical factors, and corrections for dark matter experiments based on elastic nuclear recoil.” In: *Astropart. Phys.* 6 (1996), pp. 87–112. DOI: [10.1016/S0927-6505\(96\)00047-3](https://doi.org/10.1016/S0927-6505(96)00047-3).
- [28] Katherine Freese, Mariangela Lisanti, and Christopher Savage. “Colloquium: Annual modulation of dark matter.” In: *Rev. Mod. Phys.* 85 (2013), pp. 1561–1581. DOI: [10.1103/RevModPhys.85.1561](https://doi.org/10.1103/RevModPhys.85.1561). arXiv: [1209.3339](https://arxiv.org/abs/1209.3339) [astro-ph.CO].
- [29] E. Aprile et al. “Dark Matter Search Results from a One Ton-Year Exposure of XENON1T.” In: *Phys. Rev. Lett.* 121.11 (2018), p. 111302. DOI: [10.1103/PhysRevLett.121.111302](https://doi.org/10.1103/PhysRevLett.121.111302). arXiv: [1805.12562](https://arxiv.org/abs/1805.12562) [astro-ph.CO].
- [30] E. Aprile and T. Doke. “Liquid Xenon Detectors for Particle Physics and Astrophysics.” In: *Rev. Mod. Phys.* 82 (2010), pp. 2053–2097. DOI: [10.1103/RevModPhys.82.2053](https://doi.org/10.1103/RevModPhys.82.2053). arXiv: [0910.4956](https://arxiv.org/abs/0910.4956) [physics.ins-det].
- [31] E. Aprile et al. “XENON1T dark matter data analysis: Signal and background models and statistical inference.” In: *Phys. Rev. D* 99.11 (2019). [Erratum: *Phys. Rev. D* 111, 059904 (2025)], p. 112009. DOI: [10.1103/PhysRevD.99.112009](https://doi.org/10.1103/PhysRevD.99.112009). arXiv: [1902.11297](https://arxiv.org/abs/1902.11297) [physics.ins-det].
- [32] E. Aprile et al. “First Search for Light Dark Matter in the Neutrino Fog with XENONnT.” In: *Phys. Rev. Lett.* 134.11 (2025), p. 111802. DOI: [10.1103/PhysRevLett.134.111802](https://doi.org/10.1103/PhysRevLett.134.111802). arXiv: [2409.17868](https://arxiv.org/abs/2409.17868) [hep-ex].
- [33] Zihao Bo et al. “Dark Matter Search Results from 1.54 Tonne · Year Exposure of PandaX-4T.” In: *Phys. Rev. Lett.* 134.1 (2025), p. 011805. DOI: [10.1103/PhysRevLett.134.011805](https://doi.org/10.1103/PhysRevLett.134.011805). arXiv: [2408.00664](https://arxiv.org/abs/2408.00664) [hep-ex].
- [34] Til Piffl et al. “The RAVE survey: the Galactic escape speed and the mass of the Milky Way.” In: *Astron. Astrophys.* 562 (2014), A91. DOI: [10.1051/0004-6361/201322531](https://doi.org/10.1051/0004-6361/201322531). arXiv: [1309.4293](https://arxiv.org/abs/1309.4293) [astro-ph.GA].
- [35] Chen Xia, Yan-Hao Xu, and Yu-Feng Zhou. “Constraining light dark matter upscattered by ultrahigh-energy cosmic rays.” In: *Nucl. Phys. B* 969 (2021), p. 115470. DOI: [10.1016/j.nuclphysb.2021.115470](https://doi.org/10.1016/j.nuclphysb.2021.115470). arXiv: [2009.00353](https://arxiv.org/abs/2009.00353) [hep-ph].
- [36] Chen Xia, Yan-Hao Xu, and Yu-Feng Zhou. “Production and attenuation of cosmic-ray boosted dark matter.” In: *JCAP* 02.02 (2022), p. 028. DOI: [10.1088/1475-7516/2022/02/028](https://doi.org/10.1088/1475-7516/2022/02/028). arXiv: [2111.05559](https://arxiv.org/abs/2111.05559) [hep-ph].
- [37] Richie Diurba, Helena Kolešová, and Gailyn Monroe. “Effect of inelastic scattering on cosmic-ray-boosted dark matter.” In: *PoS ICHEP2024* (2025), p. 774. DOI: [10.22323/1.476.0774](https://doi.org/10.22323/1.476.0774). arXiv: [2409.05932](https://arxiv.org/abs/2409.05932) [hep-ph].
- [38] Christopher V. Cappiello et al. “Cosmic ray-boosted dark matter at IceCube.” In: *Phys. Rev. D* 110.9 (2024), p. 095031. DOI: [10.1103/PhysRevD.110.095031](https://doi.org/10.1103/PhysRevD.110.095031). arXiv: [2405.00086](https://arxiv.org/abs/2405.00086) [hep-ph].
- [39] Keyu Lu et al. “Inelastic Scattering of Dark Matter with Heavy Cosmic Rays.” In: *Res. Astron. Astrophys.* 24.6 (2024), p. 065007. DOI: [10.1088/1674-4527/ad3c6f](https://doi.org/10.1088/1674-4527/ad3c6f). arXiv: [2310.12501](https://arxiv.org/abs/2310.12501) [astro-ph.HE].
- [40] H. Goldberg. “Constraint on the Photino Mass from Cosmology.” In: *Phys. Rev. Lett.* 50 (1983). Ed. by M. A. Srednicki. [Erratum: *Phys. Rev. Lett.* 103, 099905 (2009)], p. 1419. DOI: [10.1103/PhysRevLett.50.1419](https://doi.org/10.1103/PhysRevLett.50.1419).
- [41] John R. Ellis et al. “Supersymmetric Relics from the Big Bang.” In: *Nucl. Phys. B* 238 (1984). Ed. by M. A. Srednicki, pp. 453–476. DOI: [10.1016/0550-3213\(84\)90461-9](https://doi.org/10.1016/0550-3213(84)90461-9).

- [42] Jonathan L. Feng. “The WIMP paradigm: Theme and variations.” In: *SciPost Phys. Lect. Notes* 71 (2023), p. 1. DOI: 10.21468/SciPostPhysLectNotes.71. arXiv: 2212.02479 [hep-ph].
- [43] J. Aalbers et al. “First constraints on WIMP-nucleon effective field theory couplings in an extended energy region from LUX-ZEPLIN.” In: *Phys. Rev. D* 109.9 (2024), p. 092003. DOI: 10.1103/PhysRevD.109.092003. arXiv: 2312.02030 [hep-ex].
- [44] M. N. Mazziotta. “Indirect searches for dark matter with the Fermi LAT instrument.” In: *Int. J. Mod. Phys. A* 29 (2014), p. 1430030. DOI: 10.1142/S0217751X14300300. arXiv: 1404.2538 [astro-ph.HE].
- [45] Andrea Albert. “Indirect Searches for Dark Matter with the Fermi Large Area Telescope.” In: *Phys. Procedia* 61 (2015). Ed. by Frank Avignone and Wick Haxton, pp. 6–12. DOI: 10.1016/j.phpro.2014.12.004.
- [46] Pierre Salati. “Indirect Dark Matter searches in the light of the recent AMS-02 observations.” In: *17th Lomonosov Conference on Elementary Particle Physics*. 2017, pp. 305–311. DOI: 10.1142/9789813224568_0047. arXiv: 1605.01218 [astro-ph.HE].
- [47] Jessica Goodman et al. “Constraints on Dark Matter from Colliders.” In: *Phys. Rev. D* 82 (2010), p. 116010. DOI: 10.1103/PhysRevD.82.116010. arXiv: 1008.1783 [hep-ph].
- [48] Yonit Hochberg et al. “Mechanism for Thermal Relic Dark Matter of Strongly Interacting Massive Particles.” In: *Phys. Rev. Lett.* 113 (2014), p. 171301. DOI: 10.1103/PhysRevLett.113.171301. arXiv: 1402.5143 [hep-ph].
- [49] Stacy Y. Kim, Annika H. G. Peter, and David Wittman. “In the Wake of Dark Giants: New Signatures of Dark Matter Self Interactions in Equal Mass Mergers of Galaxy Clusters.” In: *Mon. Not. Roy. Astron. Soc.* 469.2 (2017), pp. 1414–1444. DOI: 10.1093/mnras/stx896. arXiv: 1608.08630 [astro-ph.CO].
- [50] Alexander Kusenko. “Sterile neutrinos: The Dark side of the light fermions.” In: *Phys. Rept.* 481 (2009), pp. 1–28. DOI: 10.1016/j.physrep.2009.07.004. arXiv: 0906.2968 [hep-ph].
- [51] Alexander Kusenko. “Sterile neutrinos.” In: *AIP Conf. Proc.* 917.1 (2007). Ed. by Heriberto Castilla Valdez, Miguel A. Perez, and Juan Carlos D’Olivo, pp. 58–68. DOI: 10.1063/1.2751940. arXiv: hep-ph/0703116.
- [52] Martina Gerbino et al. “Synergy between cosmological and laboratory searches in neutrino physics.” In: *Phys. Dark Univ.* 42 (2023), p. 101333. DOI: 10.1016/j.dark.2023.101333. arXiv: 2203.07377 [hep-ph].
- [53] R. D. Peccei and Helen R. Quinn. “CP Conservation in the Presence of Instantons.” In: *Phys. Rev. Lett.* 38 (1977), pp. 1440–1443. DOI: 10.1103/PhysRevLett.38.1440.
- [54] Olivier Wantz and E. P. S. Shellard. “Axion Cosmology Revisited.” In: *Phys. Rev. D* 82 (2010), p. 123508. DOI: 10.1103/PhysRevD.82.123508. arXiv: 0910.1066 [astro-ph.CO].
- [55] Raymond T. Co, Lawrence J. Hall, and Keisuke Harigaya. “Axion Kinetic Misalignment Mechanism.” In: *Phys. Rev. Lett.* 124.25 (2020), p. 251802. DOI: 10.1103/PhysRevLett.124.251802. arXiv: 1910.14152 [hep-ph].
- [56] G. Carosi et al. “Search for Axion Dark Matter from 1.1 to 1.3 GHz with ADMX.” In: (Apr. 2025). arXiv: 2504.07279 [hep-ex].

- [57] T. Braine et al. “Extended Search for the Invisible Axion with the Axion Dark Matter Experiment.” In: *Phys. Rev. Lett.* 124.10 (2020), p. 101303. DOI: [10.1103/PhysRevLett.124.101303](https://doi.org/10.1103/PhysRevLett.124.101303). arXiv: [1910.08638](https://arxiv.org/abs/1910.08638) [hep-ex].
- [58] C. Bartram et al. “Search for Invisible Axion Dark Matter in the 3.3–4.2 μeV Mass Range.” In: *Phys. Rev. Lett.* 127.26 (2021), p. 261803. DOI: [10.1103/PhysRevLett.127.261803](https://doi.org/10.1103/PhysRevLett.127.261803). arXiv: [2110.06096](https://arxiv.org/abs/2110.06096) [hep-ex].
- [59] Aditya Parikh et al. “Scalar Co-SIMP dark matter: models and sensitivities.” In: *JHEP* 08 (2023), p. 091. DOI: [10.1007/JHEP08\(2023\)091](https://doi.org/10.1007/JHEP08(2023)091). arXiv: [2302.00008](https://arxiv.org/abs/2302.00008) [hep-ph].
- [60] Manuel A. Buen-Abad, Razieh Emami, and Martin Schmaltz. “Cannibal Dark Matter and Large Scale Structure.” In: *Phys. Rev. D* 98.8 (2018), p. 083517. DOI: [10.1103/PhysRevD.98.083517](https://doi.org/10.1103/PhysRevD.98.083517). arXiv: [1803.08062](https://arxiv.org/abs/1803.08062) [hep-ph].
- [61] Andrew Robertson, Richard Massey, and Vincent Eke. “What does the Bullet Cluster tell us about self-interacting dark matter?” In: *Mon. Not. Roy. Astron. Soc.* 465.1 (2017), pp. 569–587. DOI: [10.1093/mnras/stw2670](https://doi.org/10.1093/mnras/stw2670). arXiv: [1605.04307](https://arxiv.org/abs/1605.04307) [astro-ph.CO].
- [62] Mohammad Hossein Namjoo, Tracy R. Slatyer, and Chih-Liang Wu. “Enhanced n-body annihilation of dark matter and its indirect signatures.” In: *JHEP* 03 (2019), p. 077. DOI: [10.1007/JHEP03\(2019\)077](https://doi.org/10.1007/JHEP03(2019)077). arXiv: [1810.09455](https://arxiv.org/abs/1810.09455) [astro-ph.CO].
- [63] Pieter Braat and Marieke Postma. “SIMPLY add a dark photon.” In: *JHEP* 03 (2023), p. 216. DOI: [10.1007/JHEP03\(2023\)216](https://doi.org/10.1007/JHEP03(2023)216). arXiv: [2301.04513](https://arxiv.org/abs/2301.04513) [hep-ph].
- [64] S. Navas et al. “Review of particle physics.” In: *Phys. Rev. D* 110.3 (2024). Chapter 49 Kinematics, p. 030001. DOI: [10.1103/PhysRevD.110.030001](https://doi.org/10.1103/PhysRevD.110.030001).
- [65] Kenneth M. Nollett and Gary Steigman. “BBN And The CMB Constrain Neutrino Coupled Light WIMPs.” In: *Phys. Rev. D* 91.8 (2015), p. 083505. DOI: [10.1103/PhysRevD.91.083505](https://doi.org/10.1103/PhysRevD.91.083505). arXiv: [1411.6005](https://arxiv.org/abs/1411.6005) [astro-ph.CO].
- [66] G. Angloher et al. “Results on MeV-scale dark matter from a gram-scale cryogenic calorimeter operated above ground.” In: *Eur. Phys. J. C* 77.9 (2017), p. 637. DOI: [10.1140/epjc/s10052-017-5223-9](https://doi.org/10.1140/epjc/s10052-017-5223-9). arXiv: [1707.06749](https://arxiv.org/abs/1707.06749) [astro-ph.CO].
- [67] E. Aprile et al. “Excess electronic recoil events in XENON1T.” In: *Phys. Rev. D* 102.7 (2020), p. 072004. DOI: [10.1103/PhysRevD.102.072004](https://doi.org/10.1103/PhysRevD.102.072004). arXiv: [2006.09721](https://arxiv.org/abs/2006.09721) [hep-ex].
- [68] E. Aprile et al. “Search for New Physics in Electronic Recoil Data from XENONnT.” In: *Phys. Rev. Lett.* 129.16 (2022), p. 161805. DOI: [10.1103/PhysRevLett.129.161805](https://doi.org/10.1103/PhysRevLett.129.161805). arXiv: [2207.11330](https://arxiv.org/abs/2207.11330) [hep-ex].
- [69] Wenyu Wang et al. “Direct detection of cosmic ray-boosted puffy dark matter.” In: *Nucl. Phys. B* 995 (2023), p. 116348. DOI: [10.1016/j.nuclphysb.2023.116348](https://doi.org/10.1016/j.nuclphysb.2023.116348). arXiv: [2305.12668](https://arxiv.org/abs/2305.12668) [hep-ph].
- [70] Hao-Ning He, B. Theodore Zhang, and Yi-Zhong Fan. “A Detectable Ultra-high-energy Cosmic-Ray Outburst from GRB 221009A.” In: *Astrophys. J.* 963.2 (2024), p. 109. DOI: [10.3847/1538-4357/ad2352](https://doi.org/10.3847/1538-4357/ad2352). arXiv: [2401.11566](https://arxiv.org/abs/2401.11566) [astro-ph.HE].
- [71] P. Abreu et al. “The energy spectrum of cosmic rays beyond the turn-down around 10^{17} eV as measured with the surface detector of the Pierre Auger Observatory.” In: *Eur. Phys. J. C* 81.11 (2021), p. 966. DOI: [10.1140/epjc/s10052-021-09700-w](https://doi.org/10.1140/epjc/s10052-021-09700-w). arXiv: [2109.13400](https://arxiv.org/abs/2109.13400) [astro-ph.HE].

- [72] Stefano Gabici. “Low-energy cosmic rays: regulators of the dense interstellar medium.” In: *Astron. Astrophys. Rev.* 30.1 (2022), p. 4. DOI: [10.1007/s00159-022-00141-2](https://doi.org/10.1007/s00159-022-00141-2). arXiv: [2203.14620](https://arxiv.org/abs/2203.14620) [astro-ph.HE].
- [73] R. Aloisio, V. Berezinsky, and A. Gazizov. “Transition from galactic to extragalactic cosmic rays.” In: *Astropart. Phys.* 39-40 (2012), pp. 129–143. DOI: [10.1016/j.astropartphys.2012.09.007](https://doi.org/10.1016/j.astropartphys.2012.09.007). arXiv: [1211.0494](https://arxiv.org/abs/1211.0494) [astro-ph.HE].
- [74] Cheng-Rui Zhu and Mei-Juan Wang. “Probing solar modulation of AMS-02 time-dependent D, ^3He and ^4He fluxes with modified force field approximation.” In: (Feb. 2025). arXiv: [2502.10016](https://arxiv.org/abs/2502.10016) [astro-ph.HE].
- [75] A. C. Cummings et al. “Galactic Cosmic Rays in the Local Interstellar Medium: Voyager 1 Observations and Model Results.” In: *Astrophys. J.* 831.1 (2016), p. 18. DOI: [10.3847/0004-637X/831/1/18](https://doi.org/10.3847/0004-637X/831/1/18).
- [76] Edward C. Stone et al. “Cosmic Ray Measurements from Voyager 2 as It Crossed into Interstellar Space.” In: *Nature Astronomy* 3.11 (Nov. 2019), pp. 1013–1018. ISSN: 2397-3366. DOI: [10.1038/s41550-019-0928-3](https://doi.org/10.1038/s41550-019-0928-3).
- [77] O. Adriani et al. “Time dependence of the proton flux measured by PAMELA during the July 2006 - December 2009 solar minimum.” In: *Astrophys. J.* 765 (2013), p. 91. DOI: [10.1088/0004-637X/765/2/91](https://doi.org/10.1088/0004-637X/765/2/91). arXiv: [1301.4108](https://arxiv.org/abs/1301.4108) [astro-ph.HE].
- [78] L.L. Zhao et al. “Modulation of galactic cosmic rays during the unusual solar minimum between cycles 23 and 24.” In: *Journal of Geophysical Research: Space Physics* 119.3 (Mar. 2014), pp. 14931506. ISSN: 2169-9402. DOI: [10.1002/2013ja019550](https://doi.org/10.1002/2013ja019550). URL: <http://dx.doi.org/10.1002/2013JA019550>.
- [79] Y. Shikaze et al. “Measurements of 0.2 to 20-GeV/n cosmic-ray proton and helium spectra from 1997 through 2002 with the BESS spectrometer.” In: *Astropart. Phys.* 28 (2007), pp. 154–167. DOI: [10.1016/j.astropartphys.2007.05.001](https://doi.org/10.1016/j.astropartphys.2007.05.001). arXiv: [astro-ph/0611388](https://arxiv.org/abs/astro-ph/0611388).
- [80] T. T. von Rosenvinge et al. “The Modulation of Galactic Cosmic Rays Between 1 and 17 AU.” In: *International Cosmic Ray Conference*. Vol. 3. International Cosmic Ray Conference. Jan. 1979, p. 248.
- [81] Cristina Consolandi. “Precision Measurement of the Proton Flux in Primary Cosmic Rays from 1 GV to 1.8 TV with the Alpha Magnetic Spectrometer on the International Space Station.” In: *25th European Cosmic Ray Symposium*. Dec. 2016. arXiv: [1612.08562](https://arxiv.org/abs/1612.08562) [astro-ph.HE].
- [82] W. Menn et al. “The Absolute Flux of Protons and Helium at the Top of the Atmosphere Using IMAX.” In: *The Astrophysical Journal* 533.1 (2000), p. 281. DOI: [10.1086/308645](https://doi.org/10.1086/308645). URL: <https://dx.doi.org/10.1086/308645>.
- [83] W. R. Webber et al. “A Measurement of the Cosmic-Ray ^2H and ^3He Spectra and $^2\text{H}/^4\text{He}$ and $^3\text{He}/^4\text{He}$ Ratios in 1989.” In: *The Astrophysical Journal* 380 (Oct. 1991), p. 230. DOI: [10.1086/170578](https://doi.org/10.1086/170578).
- [84] K. C. Hsieh, G. M. Mason, and J. A. Simpson. “Cosmic-Ray ^2H from Satellite Measurements, 1965-1969.” In: *The Astrophysical Journal* 166 (May 1971), p. 221. DOI: [10.1086/150951](https://doi.org/10.1086/150951).
- [85] Etienne E. Vos and Marius S. Potgieter. “NEW MODELING OF GALACTIC PROTON MODULATION DURING THE MINIMUM OF SOLAR CYCLE 23/24.” In: *The Astrophysical Journal* 815.2 (2015), p. 119. DOI: [10.1088/0004-637X/815/2/119](https://doi.org/10.1088/0004-637X/815/2/119). URL: <https://dx.doi.org/10.1088/0004-637X/815/2/119>.

- [86] M. J. Boschini et al. “Inference of the Local Interstellar Spectra of Cosmic-Ray Nuclei $Z \leq 28$ with the GalProp–HelMod Framework.” In: *Astrophys. J. Suppl.* 250.2 (2020), p. 27. DOI: [10.3847/1538-4365/aba901](https://doi.org/10.3847/1538-4365/aba901). arXiv: [2006.01337](https://arxiv.org/abs/2006.01337) [astro-ph.HE].
- [87] Kyrylo Bondarenko et al. “Direct detection and complementary constraints for sub-GeV dark matter.” In: *JHEP* 03 (2020), p. 118. DOI: [10.1007/JHEP03\(2020\)118](https://doi.org/10.1007/JHEP03(2020)118). arXiv: [1909.08632](https://arxiv.org/abs/1909.08632) [hep-ph].
- [88] Paolo Desiati et al. “Snowmass 2021 LoI: Determination of cosmic ray properties in the local interstellar medium with all-sky anisotropy observations.” In: (Sept. 2020). arXiv: [2009.04883](https://arxiv.org/abs/2009.04883) [astro-ph.HE].
- [89] Michael E. Peskin and Daniel V. Schroeder. *An Introduction to Quantum Field Theory*. Reading, USA: Addison-Wesley, 1995. ISBN: 978-0-201-50397-5, 978-0-429-50355-9, 978-0-429-49417-8. DOI: [10.1201/9780429503559](https://doi.org/10.1201/9780429503559).
- [90] Matthew D. Schwartz. *Quantum Field Theory and the Standard Model*. Cambridge University Press, Mar. 2014. ISBN: 978-1-107-03473-0, 978-1-107-03473-0.
- [91] C. F. Perdrisat, V. Punjabi, and M. Vanderhaeghen. “Nucleon Electromagnetic Form Factors.” In: *Prog. Part. Nucl. Phys.* 59 (2007), pp. 694–764. DOI: [10.1016/j.ppnp.2007.05.001](https://doi.org/10.1016/j.ppnp.2007.05.001). arXiv: [hep-ph/0612014](https://arxiv.org/abs/hep-ph/0612014).
- [92] V. Punjabi et al. “The Structure of the Nucleon: Elastic Electromagnetic Form Factors.” In: *Eur. Phys. J. A* 51 (2015), p. 79. DOI: [10.1140/epja/i2015-15079-x](https://doi.org/10.1140/epja/i2015-15079-x). arXiv: [1503.01452](https://arxiv.org/abs/1503.01452) [nucl-ex].
- [93] R. Anni, G. Co, and P. Pellegrino. “Nuclear charge density distributions from elastic electron scattering data.” In: *Nucl. Phys. A* 584 (1995), pp. 35–59. DOI: [10.1016/0375-9474\(94\)00508-K](https://doi.org/10.1016/0375-9474(94)00508-K). arXiv: [nucl-th/9410023](https://arxiv.org/abs/nucl-th/9410023).
- [94] T. Heinzl, B. King, and D. Liu. “Coherent enhancement of QED cross sections in electromagnetic backgrounds.” In: *Phys. Rev. D* 111.5 (2025), p. 056018. DOI: [10.1103/PhysRevD.111.056018](https://doi.org/10.1103/PhysRevD.111.056018). arXiv: [2412.10574](https://arxiv.org/abs/2412.10574) [hep-ph].
- [95] Eero Byckling and K. Kajantie. *Particle Kinematics*. London: John Wiley & Sons, 1973. ISBN: 0471128856.
- [96] R. Kumar. “Covariant phase-space calculations of n-body decay and production processes.” In: *Phys. Rev.* 185 (1969), pp. 1865–1875. DOI: [10.1103/PhysRev.185.1865](https://doi.org/10.1103/PhysRev.185.1865).
- [97] John R. Rumble, David R. Lide, and Thomas J. Bruno. *CRC Handbook of Chemistry and Physics: A Ready-Reference Book of Chemical and Physical Data*. 2017-2018, 98th edition. Boca Raton: CRC Press, 2017. ISBN: 9781498784542. URL: <https://www.worldcat.org/title/992909678>.
- [98] James M. Cline et al. “Enabling Forbidden Dark Matter.” In: *Phys. Rev. D* 96.8 (2017), p. 083521. DOI: [10.1103/PhysRevD.96.083521](https://doi.org/10.1103/PhysRevD.96.083521). arXiv: [1702.07716](https://arxiv.org/abs/1702.07716) [hep-ph].
- [99] Troy A. Porter, Gudlaugur Johannesson, and Igor V. Moskalenko. “The GALPROP Cosmic-ray Propagation and Nonthermal Emissions Framework: Release v57.” In: *Astrophys. J. Suppl.* 262.1 (2022), p. 30. DOI: [10.3847/1538-4365/ac80f6](https://doi.org/10.3847/1538-4365/ac80f6). arXiv: [2112.12745](https://arxiv.org/abs/2112.12745) [astro-ph.HE].
- [100] Carmelo Evoli et al. “Cosmic-ray propagation with DRAGON2: II. Nuclear interactions with the interstellar gas.” In: *JCAP* 07 (2018), p. 006. DOI: [10.1088/1475-7516/2018/07/006](https://doi.org/10.1088/1475-7516/2018/07/006). arXiv: [1711.09616](https://arxiv.org/abs/1711.09616) [astro-ph.HE].